

**STRUCTURAL AND LUMINESCENCE PROPERTIES OF $\text{NaYF}_4:\text{Yb}^{3+}/\text{Er}^{3+}$ AND
 $\text{NaGdF}_4:\text{Yb}^{3+}/\text{Nd}^{3+}$ NANOCRYSTALS FOR POSSIBLE APPLICATION IN PHOTOVOLTAIC SOLAR
CELLS**

by

THOKWANE PEBETSI

submitted in accordance with the requirements for
the degree of

MASTER OF SCIENCE

in Physics

at the

University of South Africa (UNISA)

Supervisor: Prof PS Mbule

April 2023

DECLARATION

Name: Thokwane Pebetsi_____

Student number: 13173251_____

Degree: Master of science in physics_____

Exact wording of the title of the dissertation as appearing on the electronic copy submitted for examination:

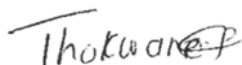
Structural and luminescence properties of $\text{NaYF}_4:\text{Yb}^{3+}/\text{Er}^{3+}$ and $\text{NaGdF}_4:\text{Yb}^{3+}/\text{Nd}^{3+}$ powder nanocrystals for possible application in photovoltaic solar cells.

I declare that the above dissertation is my own work and that all the sources that I have used or quoted have been indicated and acknowledged by means of complete references.

I further declare that I submitted the dissertation to originality checking software and that it falls within the accepted requirements for originality.

I further declare that I have not previously submitted this work, or part of it, for examination at Unisa for another qualification or at any other higher education institution.

(The dissertation will not be examined unless this statement has been submitted.)



SIGNATURE

20 April 2023

DATE

ACKNOWLEDGEMENTS

- I want to start by thanking the Almighty God for his constant assistance, direction, and protection during my studies.
- Sincere appreciation goes out to my dissertation advisor, Professor P.S. Mbule, for her unwavering support, inspiration, tolerance, and guidance throughout my MSc studies.
- Many thanks to Prof. L.L. Noto, who assisted me in conducting TL studies and interpreting the results.
- I am very appreciative of my parents, Mr. M.L. Thokwane and Mrs. M.S. Thokwane, as well as my siblings, Rudzani and Phumudzo Thokwane, for their support in all the decisions I took regarding my studies.
- Additionally, I want to thank the UNISA Physics Department and the South African National Research Foundation (NRF) for their financial assistance.
- Finally, I want to express my gratitude to Mudivhi Marcus Tshishivhiri for his unending love, friendship, humor, support, and inspiration throughout my academic journey.

DEDICATIONS

This dissertation is dedicated to my late younger sister Motshedi Mbavhalelo Thokwane (2002-2022) and my aunt Ms Emily Tshilidzi Mphaga (1958-2019). May your souls continue to rest in peace.

Abstract

NaYF₄:Yb³⁺/Er³⁺ and NaGdF₄:Yb³⁺/Nd³⁺ nanocrystals were prepared using a solution combustion (SC) method and their properties were evaluated for potential use as photon harvesters in photovoltaic solar cells (PSCs). The dopant concentrations were varied (10–30 mol% Yb³⁺, 1–3 mol% Er³⁺/Nd³⁺), and the samples went through an annealing process at 600 and 700 °C. The effect of doping and annealing on their structure, morphology, photon absorbance, photoluminescence (PL), and thermoluminescence (TL) was investigated.

The α -cubic and β -hexagonal phases of the nanocrystals was confirmed by X-ray diffractometer (XRD). Changing the dopant concentration and annealing temperature, respectively caused a distinct change in morphology (cubic to hexagonal and rod-like). It was observed that photon absorption occurred in the range from visible to near infrared (NIR), and bandgap values were greatly reduced. PL demonstrated upconversion (UC) and effective transfer of energy from Yb³⁺ to Er³⁺ ions, and also from Yb³⁺ to Nd³⁺ ions. The UC luminescence was boosted by annealing the nanocrystals. The thermogravimetric analysis (TGA) of the nanocrystals shed light on their stable temperatures, while the defects within the materials were investigated using TL. The kinetics involved in the electron trapping centres were found to be that of first order, and the depth of the electron trapping centres was determined using the initial rise (IR) method.

Key terms: Combustion; NaYF₄; NaGdF₄; Upconversion; luminescence; ytterbium; erbium; neodymium; morphology; bandgap

Acronyms

XRD - X-ray diffraction

EDX – Energy dispersive X-ray spectroscopy

SEM – Scanning electron microscope.

UV/Vis/NIR – Ultraviolet-visible near-infrared spectroscopy

PL – Photoluminescence

FTIR – Fourier transmission infrared spectroscopy

TGA – Thermogravimetric analysis

TL – Thermoluminescence

PCE- Power conversion efficiency

PV – Photovoltaic

UC – Upconversion

ESA – Excited state absorption

PA - Photon Avalanche

ETU – Energy transfer upconversion

RE – Rare-earth

UPL – Upconversion photoluminescence

QDS – Quantum dots

UCNCS - Upconversion nanocrystals

SPP – surface plasmon polariton

PSCs – Photovoltaic solar cells

SC – Solution combustion

CCD – Charge-coupled detector

TABLE OF CONTENTS

Chapter 1	1
1.1 Background	1
1.2 Problem statement	2
1.3 Aim of the study	3
1.4 objectives	3
1.5 Layout of the dissertation	4
Chapter 2	7
2.1 Photovoltaic (PV) cells	7
2.1.1 Photovoltaic effect	8
2.1.2 Photovoltaic cells generations	10
2.2 Structure and function of photovoltaic cells	11
2.3 Upconversion mechanism	17
2.4 Luminescent materials	21
2.5 Lanthanide-based upconverters	21
2.5.1 Activators	22
2.5.2 Sensitizers	24
2.5.3 Host Materials	25
2.6 Thermoluminescent Materials	27
Chapter 3	40
3.1 Introduction	40
3.2 Synthesis of powder nanocrystals	40
3.2.1 Solution combustion process	41
3.2.2. Experimental details	42
3.3 Characterization techniques	45
3.3.1 X-ray Diffractometer (Rigaku smartLab X-ray diffractometer (Cu K α , 45 kV and 200 mA).	45
3.3.2 Field-emission scanning electron microscopy (JEOL JSM-7800 (SEM) coupled with Oxford Aztec 350 X-Max 80 EDS.	46
3.3.3 Thermogravimetric analysis (SDT (TGA) Q600 T A Instruments).	48
3.3.4 Fourier-transform infrared spectroscopy (SHIMADZU-IRTracer-100).	49

3.3.5 Ultraviolet, Visible, and near-infrared system (PerkinElmer Lambda 1050 UV/Vis/NIR)	50
3.3.6 Photoluminescence Spectroscopy (Horiba Jobin Yvon Fluorolog 3).	52
3.3.7 Raman spectroscopy (XploRA PLUS Raman microscope).....	53
3.3.8 Thermoluminescence spectroscopy (Riso TL/OSL reader, model DA-20).....	54
Chapter 4.....	61
4.1 Introduction	61
4.2 results and discussion.....	64
4.2.1 XRD studies.....	64
4.2.2 Crystallite size, lattice parameters and strain analysis.....	70
4.2.2 FE-SEM and EDS and elemental mapping analysis.....	76
4.2.3 Thermogravimetric (TGA) analysis	84
4.2.4 FTIR and Raman Analysis	85
Chapter 5.....	98
Optical and thermoluminescence studies of the NaYF ₄ :Yb ³⁺ ,Er ³⁺ and NaGdF ₄ :Yb ³⁺ ,Nd ³⁺ nanocrystals.....	98
5.1 introduction	98
5.2.1 Photoluminescence (PL) analysis.....	98
5.2.2 Proposed energy-transfer mechanism.....	104
5.2.4 UV-Vis-NIR analysis	106
5.2.5 Thermoluminescence analysis.....	111
Chapter 6.....	123
6.1 Conclusion	123
6.2 Future work	124

CHAPTER 1

Introduction

1.1 BACKGROUND

The South African energy crisis is a period in which the country is experiencing extensive rolling blackouts due to a supply shortage that threatens to collapse the national system. This started in the later months of 2007 and continues to this day [1–3]. This is due to the annual rapid increase in energy consumption and infrastructure deterioration. As global energy consumption rises, demand for natural resources such as natural gas, coal, and petroleum will rise as well, negatively impacting the development of economies around the world [4-5]. As a result, an alternative technology is required to be implemented, and thus, several energy technologies are being investigated and developed.

The economy of South Africa, a developing nation, relies heavily on the energy-intensive sectors of manufacturing and mining. South Africa has not been very efficient in its use of energy, despite having some of the cheapest electrical supplies. Eskom, a state-owned company, is South Africa's sole wholesale electricity supplier. Due to the rapid decline of power plants and the depletion of coal, Eskom has acknowledged that electricity supply will be severely constrained for at least the next five years [4].

Solar energy is regarded as the most widely available form of renewable energy on earth because of its positive effects on the environment, the economy, and strategic planning. As a result, its utilization for the generation of electricity is becoming increasingly widespread across the globe [4–6]. The sun gives the earth a tremendous amount of energy. In just one minute, the sun produces enough energy to power the entire world for an entire year. It generates more energy in a single day than our current population would consume in 27 years. The total amount of energy contained in all forms of fossil fuel is equivalent to the amount of radiation coming from the sun that the earth is subjected to over the course of three days [7]. The two primary technologies for converting solar energy into electricity are photovoltaics (PVs) and solar thermal generators. Other

energy-supply technologies, including wind, power, and biogas, are also being investigated for energy supply in some countries [4]. We can generate power, heat, and fuel from sources of renewable energy using renewable energy technology [8]. Directly or indirectly, the sun powers wind, water, waves, heat exchange, tidal waves, and bioenergy technologies. Bioenergy systems are capable of transforming the solar energy that is stored in plants, food waste, farm waste, forest waste, sewage, and algae into heat, electricity, and fuel through a variety of different mechanisms. We can generate electricity, heat, and cool our homes, and travel by land, sea, and possibly air, and all of these activities can be done without the emission of greenhouse gases or other pollutants [9].

Solar energy is possibly the most readily apparent form of renewable energy source, so it is imperative that we rapidly scale up the application of solar cell technology to produce an adequate amount of power to maintain our future civilization. A pressing concern, particularly considering the recent increase in oil prices and the ongoing damage to the ecosystem of the planet because of the burning of fossil fuels [10].

1.2 PROBLEM STATEMENT

The incompatibility between the photon energy distribution and the bandgap values of the relevant semiconductors is a major issue limiting solar cells' efficiency. The conversion of sunlight's wavelength, that is, solar energy, to electrical energy is thought to be an efficient way to lessen spectral mismatch losses. Some researchers are looking into using semiconductors with UC properties to alter the light spectrum for PV cells. It is through UC that photons whose energies are below the band gap of a solar cell are transformed into photons with energies above the band gap, where they can be absorbed [16, 17].

Extending the spectrum of the sun's radiation to include the NIR wavelength is a critical technique for boosting the power efficiency of PSCs in converting sunlight into electricity [16, 17]. A lot of work is put into increasing solar cells' power conversion efficiencies (PCE) and keeping them stable at high temperatures [18]. Many scientists have had difficulty convincing themselves that expanding or reshaping the solar materials' absorption spectrum is a good idea [19]. Since most PSCs materials have an energy band

of about 1.5 eV, the typical range of wavelengths for AM (air mass) 1.5 G (global) sunlight condition is from 280 to 2500 nm. PV materials absorb the sun's photons in the range of 300 to 800 nm, but this merely constitutes about 45 % of the total solar spectrum. Since photons in the NIR regions are not efficiently absorbed, PCE is hindered by the challenge posed by the loss of energy. As more solar irradiation in the ultraviolet (UV) and NIR areas is not fully utilized by light absorption materials in PSCs, NIR spectra have been used in more research to enhance the features of PSCs [20–21]. It has been discovered that PSCs can have their properties enhanced by converting photons with a NIR wavelength into photons with a higher energy that can be absorbed by PSC materials and increase the amount of photocurrent in the active layer [22]. As a results, the efficiency of the PSC materials can have their absorption increased by using UC materials such as nanocrystals of sodium yttrium tetrafluoride (NaYF_4) and sodium gadolinium tetrafluoride (NaGdF_4) that have been doped with rare-earth ions (RE^{3+} ions). UC nanocrystals (UCNCs) doped with RE^{3+} ions are widely regarded as the most efficient luminous upconverting materials used in solar cells, due to their long luminous lifetimes and exceptional optical stability [23]. Furthermore, upconverting nanocrystals that are thermally stable are crucial for their potential in optical applications. As a result, in this work, NaYF_4 and NaGdF_4 doped with RE^{3+} ions will be synthesized, and their properties will be investigated for possible application in PSCs.

1.3 AIM OF THE STUDY

The aim of this study is to prepare upconverting $\text{NaYF}_4\text{:Yb}^{3+}/\text{Er}^{3+}$ and $\text{NaGdF}_4\text{:Yb}^{3+}/\text{Nd}^{3+}$ nanocrystals using solution combustion method so that they can be used as photon harvesters in the NIR region of the solar spectrum for possible application in PSCs.

1.4 OBJECTIVES

- To synthesize $\text{NaYF}_4\text{:Yb}^{3+}/\text{Er}^{3+}$ and $\text{NaGdF}_4\text{:Yb}^{3+}/\text{Nd}^{3+}$ nanocrystals using solution combustion method.

- To investigate the effect of dopant (10-30% Yb, 1-3%Er/Nd) concentration and annealing temperatures (600 °C and 700 °C) on the structure, thermal stability, and morphological characteristics of the NaYF₄ and NaGdF₄ nanocrystals.
- To investigate the effect of dopant (10-30%Yb, 1-3%Er/Nd) concentration and annealing temperature on the optical absorption (UV-VIS-NIR), PL and TL features of the NaYF₄ and NaGdF₄ nanocrystals.
- Analyse the obtained results for possible application is PSCs.

1.5 LAYOUT OF THE DISSERTATION

- **Chapter 2** - this chapter gives an overview on the literature of PSCs, luminescent UCNCs, RE³⁺ ions, and energy transfer mechanisms.
- **Chapter 3** - provides a thorough explanation of the synthesis method used in this study to prepare nanocrystals and theory of research techniques.
- **Chapter 4** - describes the experimental details on the SC synthesis of NaYF₄, NaGdF₄, NaYF₄:Yb³⁺, Er³⁺, and NaGdF₄:Yb³⁺, Nd³⁺, as well as the structural, elemental, and morphological analysis of the mentioned nanocrystals.
- **Chapter 5** - provides optical and luminescent features of NaYF₄, NaGdF₄, NaYF₄:Yb³⁺, Er³⁺, and NaGdF₄:Yb³⁺, Nd³⁺ nanocrystals.

References

- [1]. Constantinides, P. and Slavova, M., 2020. From a monopoly to an entrepreneurial field: The constitution of possibilities in South African energy. *Journal of Business Venturing*, 35 (6), pp.106061.
- [2]. Matthewman, S. and Byrd, H., 2013. Blackouts: a sociology of electrical power failure. *Social Space (Przestrzeń Społeczna)*, pp.31-55.
- [3]. Pollet, B.G., Staffell, I. and Adamson, K.A., 2015. Current energy landscape in the Republic of South Africa. *International Journal of Hydrogen Energy*, 40(46), pp.16685-16701.
- [4]. Dima, R.S., 2018. *Density functional theory study of TiO₂ Brookite (100), (110) and (210) surfaces doped with ruthenium (Ru) and platinum (Pt) for application in dye sensitized solar cells* (Masters dissertation, University of Venda).
- [5]. Bilgen, S.E.L.Ç.U.K., 2014. Structure and environmental impact of global energy consumption. *Renewable and Sustainable Energy Reviews*, 38, pp.890-902.
- [6]. Sampaio, P.G.V. and González, M.O.A., 2017. Photovoltaic solar energy: Conceptual framework. *Renewable and Sustainable Energy Reviews*, 74, pp.590-601.
- [7]. Bagher, A.M., Vahid, M.M.A. and Mohsen, M., 2015. Types of solar cells and application. *American Journal of optics and Photonics*, 3(5), pp.94-113.
- [8] Awan, A.B., and Z.A. Khan, 2014. Recent advances in renewable energy—A remedy for Pakistan's energy crisis. *Renewable and Sustainable Energy Reviews*, 33, pp.236-253.
- [9]. Gates, S., King, A., Bunn, L., Rose, B. and Energy, S., 2017. GREENS. ORG. AU/WA.
- [10]. Mbule, P.S., 2013. *The effects of the ZnO nanoparticles buffer layer on organic solar cells* (Doctoral dissertation, University of the Free State).

- [16]. Wang, M., Wu, Y., Juan, F., Li, Y., Shi, B., Xu, F., Jia, J., Wei, H. and Cao, B., 2021. Enhanced photocurrent of perovskite solar cells by dual-sensitized β -NaYF₄: Nd³⁺/Yb³⁺/Er³⁺ up-conversion nanoparticles. *Chemical Physics Letters*, 763, p.138253.
- [17]. Li, H., Chen, C., Jin, J., Bi, W., Zhang, B., Chen, X., Xu, L., Liu, D., Dai, Q. and Song, H., 2018. Near-infrared and ultraviolet to visible photon conversion for full spectrum response perovskite solar cells. *Nano Energy*, 50, pp.699-709.
- [18]. Wu, M., Haji Ladi, N., Yi, Z., Li, H., Shen, Y. and Wang, M., 2020. Stability Issue of Perovskite Solar Cells under Real-World Operating Conditions. *Energy Technology*, 8(4), p.1900744.
- [19]. García de Arquer, F.P., Talapin, D.V., Klimov, V.I., Arakawa, Y., Bayer, M. and Sargent, E.H., 2021. Semiconductor quantum dots: Technological progress and future challenges. *Science*, 373(6555), p. eaaz8541.
- [20]. Schoenauer, M., 2018. *Enhancing perovskite solar cells through upconversion nanoparticles insertion* (Doctoral dissertation, Sorbonne University).
- [21]. Chen, C., Zheng, S. and Song, H., 2021. Photon management to reduce energy loss in perovskite solar cells. *Chemical Society Reviews*, 50(12), pp.7250-7329.
- [22]. Bai, Y., Lang, K., Zhao, C., Guo, Q., Zeng, R., Wang, J., Hayat, T., Alsaedi, A. and Tan, Z.A., 2020. Strategies Toward Extending the Near-Infrared Photovoltaic Response of Perovskite Solar Cells. *Solar RRL*, 4(2), p.1900280.
- [23]. Raj, A.N., 2016. *Synthesis and Characterisation of Monodisperse Sub-10 Nm Alkali Metal Rare Earth Fluoride Nanocrystals* (Doctoral dissertation, Universität Osnabrück).

CHAPTER 2

Literature Review

2.1 PHOTOVOLTAIC (PV) CELLS

PV cells are electrical devices that use the PV effect to transform radiant energy into usable current. Once exposed to light, they alter electrical properties like current, voltage, or resistance [1–2]. Solar cells are PVs, regardless of whether the light source is natural or artificial [3].

Solar cell production technology is built on the basis of three essential elements. The semiconductor that turns light into electron-hole pairs by absorbing it, the junction that isolates the electrons and holes, and the contacts that allow current to flow from the front and back of the cell to the external circuit. Semiconductor choice defines the two primary categories of technology as thin layers of other materials or crystalline silicon in a liquid state [4–6].

Most solar cells have traditionally used crystalline silicon as the light-absorbing semiconductor [4, 7 - 8]. Despite its low efficiency and thickness, this material is widely used [9]. Its success can be rationalized on the basis that it makes use of process technology developed for the microelectronics industry to fabricate solar cells with a stable efficiency (11–16%) that is between 50% and 65% of the theoretical maximum [9].

Besides using solar cells for energy generation, they can be used as photodetectors, to detect light or other forms of electromagnetic radiation that are closer to the visible range, or as light intensity meters [9]. To be a feasible energy option, solar cell technology research and development must address issues with cost reduction, improved PCE, greater stability, and the use of plentiful and biocompatible raw materials [3]. For a PV cell to operate, it needs to possess the following three qualities:

- Light absorption that results in electron-hole pairs.
- Separation of electron-hole pairs.
- The unassisted transfer of such carriers into an external circuit [10–11].

2.1.1 Photovoltaic effect

A PV cell generates voltage or electric current through a process known as the "photovoltaic effect" when it is exposed to light. Due of this effect, the cells contained within a solar panel are able to convert sunlight into electrical energy, making the panel itself useful [12].

2.1.1.1 Photovoltaic effect process

PV cells are used to produce electricity from sunlight. These solar cells include a p-n junction, which is a junction between p-type and n-type semiconductors. The difference between n-type and p-type semiconductors is the primary material used to create the chemical reaction during doping. Depending on the material used, the outer orbital will have either five or three electrons making one negatively charged (n-type) and one positively charged (p-type). This junction is necessary for the solar cells to function properly. When these two semiconductors are combined, the electrons move to the p-side, "which is the positive side", and the holes move to the n-side, "which is the negative side." Due to this, an electric field is created in the area around the junction. Particles with a negative charge are accelerated in one direction by this field, while those with a positive charge are accelerated in the opposite direction [12].

Photons, the fundamental particles that make up light, are discrete bundles of electromagnetic radiation, or energy [13]. Solar panels use a special kind of cell called a PV cell to soak up the sun's rays [14]. Light of a specific wavelength must impart energy onto a single atom of the semiconducting material located in the p-n junction for these cells to function. The electrons in the material receive a controlled dose of energy. The next step is for the electrons to enter a higher energy band called conduction band. The valence band now has a "hole" through which the electron jumped. When energy is

added, electron motion creates a pair of charge carriers known as electrons and holes. Electrons keep the semiconducting material stationary by forming bonds with neighbouring atoms when they are not excited. On the other hand, these conduction-band electrons are unrestricted in their motion when they are excited. Since the p-n junction generates an electric field, electrons and holes naturally flow in different directions from one another. The liberated electron is not attracted to the p-side, but rather the n-side. An electric current is produced in the cell as a result of the electron's motion. When an electron moves, a "hole" is left behind. Like the p-side, this hole can rotate, but in a different direction. This causes a current to flow through the cell [12, 15–16]. Figure 2.1 provides a visual representation of the process that takes place in PV cells.

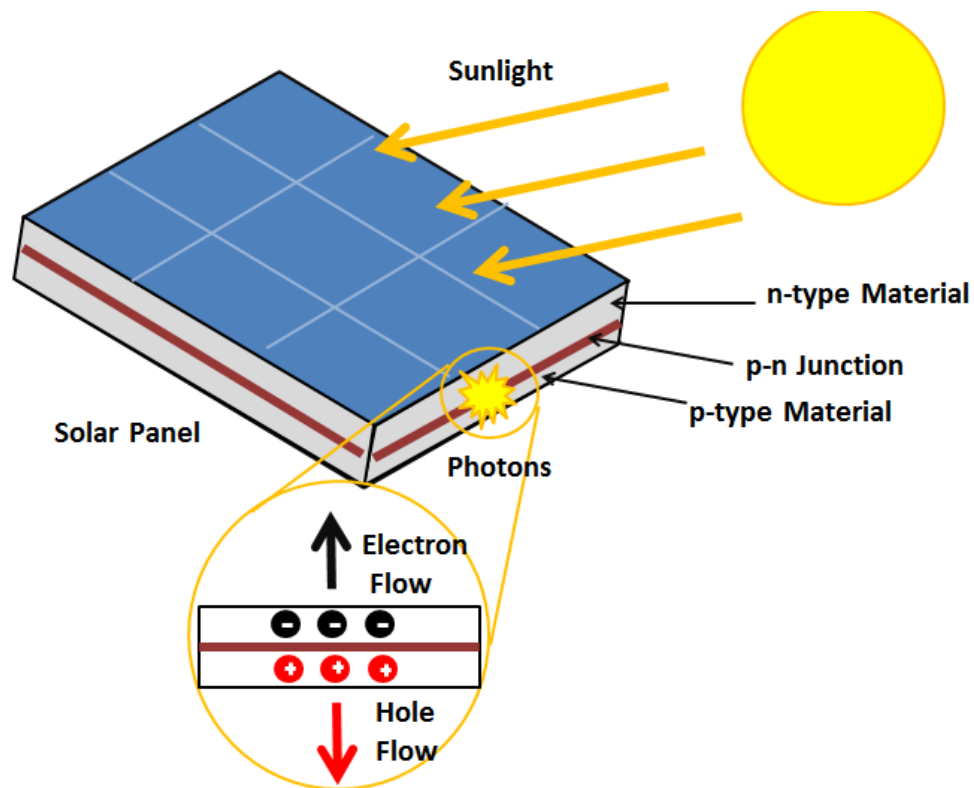


Figure 2.1: A representation of the photovoltaic effect [12].

2.1.2 Photovoltaic cells generations

Names for solar cells are usually derived from the semiconducting material used to make them. The aforementioned materials need to have specific properties so that they can absorb solar energy. While some cells are designed for use in space, others are constructed for use on the surface of the earth. Single-junction solar cells have just one layer of light-absorbing material, while multi-junction solar cells have multiple layers and different physical configurations to maximize light absorption and charge separation [1]. Performance and affordability of solar cells are used to classify them. First-generation PV cells, which make up roughly 86 %, are the most frequently used technology during the manufacturing of solar cells for commercial use. Typically, a crystalline silicon wafer with a large area of linked p-type and n-type semiconductors is used to construct them (a p-n junction diode). They are expensive to fabricate and have a wide spectral absorption range, but the vast majority of the energy carried by photons with higher energies at the blue and violet ends of the spectrum is converted to heat [18]. The second generation reduces the amount of material needed for cell design by using thin-film semiconductor deposits [19]. These solar cells enable the mounting of panels on light or flexible materials, lower production costs, and a lower cost per watt, but they are hazardous and less efficient than silicon solar cells [17]. Considering the Shockley-Queisser limit (which describes the maximum solar energy conversion efficiency achievable for a particular material and is the standard by which new PV technologies are compared), third-generation solar cells are being considered as a cheaper and safer alternative to first- and second-generation solar cells, however, the important challenge of this generation is to reduce the cost of solar electricity. [20]. These materials might be organic or nanostructured with high efficiency of more than 60% achieved by the use of different charge carrier collecting methods [19]. More emphasis has been placed on charge carrier mechanisms, charge collecting, and energy capture improvements in third-generation PSCs. They can be printed on huge regions and adjustable substrates, and they are cheap and easy to make. These new solar cell technologies include "dye-sensitized solar cells (DSSCs), colloidal quantum dot solar cells, organic PVs, and solution-processed bulk inorganic PVs" [21–23]. The fourth-generation solar cells produce a single

multispectral layer using a combination of polymers and nanoparticles [24]. These solar cells have lower material prices, self-assembly, and greater conversion efficiencies; however, they have lesser efficiencies than silicon solar cells and the same potential degradation issues as polymer cells [18].

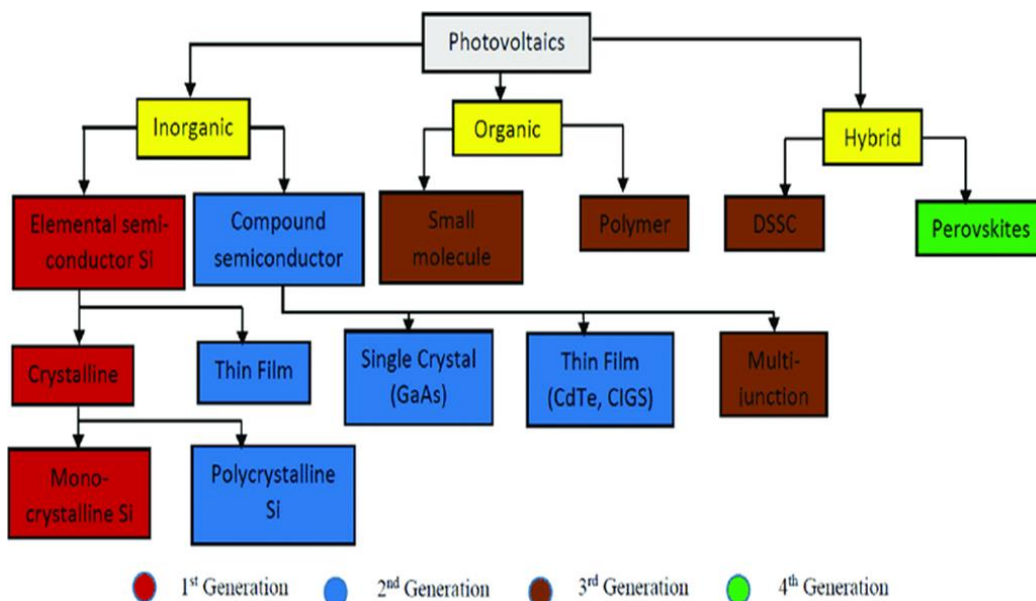


Figure 2.2: Evolution of photovoltaic cells [17].

2.2 STRUCTURE AND FUNCTION OF PHOTOVOLTAIC CELLS

Whether they are installed in a power plant, a satellite, or a calculator, PV cells all have the same fundamental design. An antireflection layer or optical coating allows light to enter the device and reduces light loss from reflection; this layer also increases the efficiency with which light from a solar cell is transmitted to its energy-conversion layers. On the surface of the cell is where the antireflection layer is located. "This layer is an oxide of silicon, tantalum, or titanium that is either spin-coated or vacuum-deposited. Under the antireflection layer are three layers that are responsible for the conversion of energy [11]. These layers are the top junction layer, the absorber layer, and the back junction layer." The cell needs two more electrical contact layers so that electricity can be conducted to an external load and then back into the cell. Only then will an electric circuit

be considered "complete" (see figure 2.3). The light-receiving side of a solar cell typically has a grid-patterned electrical contact layer made of metal or another good conductor. Since metal absorbs light, grid lines are as narrow and far apart as they can be without stopping the flow of electricity. In the back electrical contact layer, there are no such polar opposite requirements. It covers the entire back side of the cell structure, and its only purpose is to act as an electrical contact. For the same reason that metal is such a good electrical conductor, it is always used as the back layer [25, 27].

Since the majority of the energy in natural and artificial light is at visible wavelengths, the absorber material in a solar cell should be capable of absorbing that kind of radiation. Semiconductors are substances that absorb visible light very effectively. Since the layers that make connections and form junctions are much narrower, a solar cell has a thickness that is mostly similar to that of the absorber, which is a semiconductor that can help absorb all visible light and has a thickness of a hundredth of a centimetre or less. Solar cells often use semiconducting materials like "silicon, gallium arsenide, indium phosphide, and copper indium selenide" [26, 27].

Semiconductors are a type of material whose ability to conduct electricity depends on how much energy is available to excite electrons in the crystal lattice [28]. Crystalline silicon is a popular semiconductor in the field of PVs. When enough photons are absorbed by the surface of a crystal, the electrons in the crystal move from the valence to the conduction band, causing the crystal to become electrically conductive. The term "bandgap" refers to the minimum energy required to excite an electron that is stuck in its bound state into a free state where it can participate in conduction. The voltage produced by a PV cell is directly affected by the bandgap, an intrinsic property of semiconductors [29]. How much of the sun's spectrum a PV cell is able to absorb is dependent on its optical band gap (shown in Figure 2.4 below) [30]. If the bandgap is too large (wide bandgap), most photons will not cause PV effect; if it is too low most photons will have more than necessary energy to excite electrons across the bandgap, and the rest of energy will be wasted. [29].

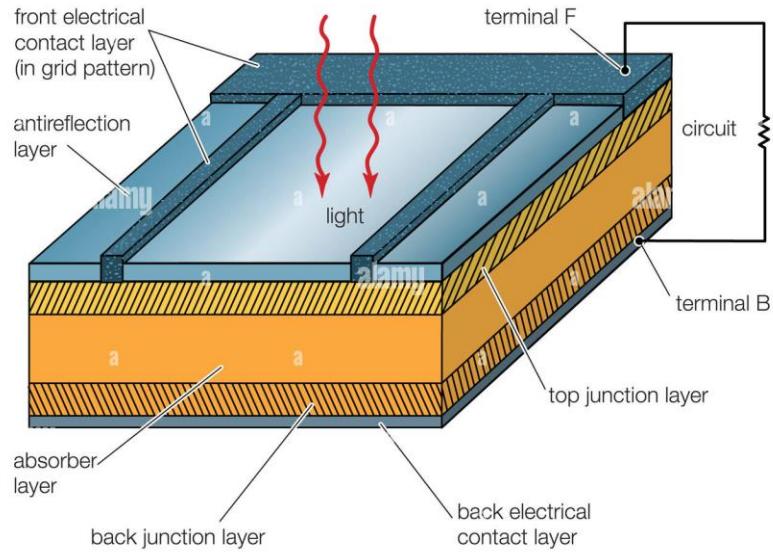


Figure 2.3: A diagram illustrating the operation of a photovoltaic cell in schematic form [25].

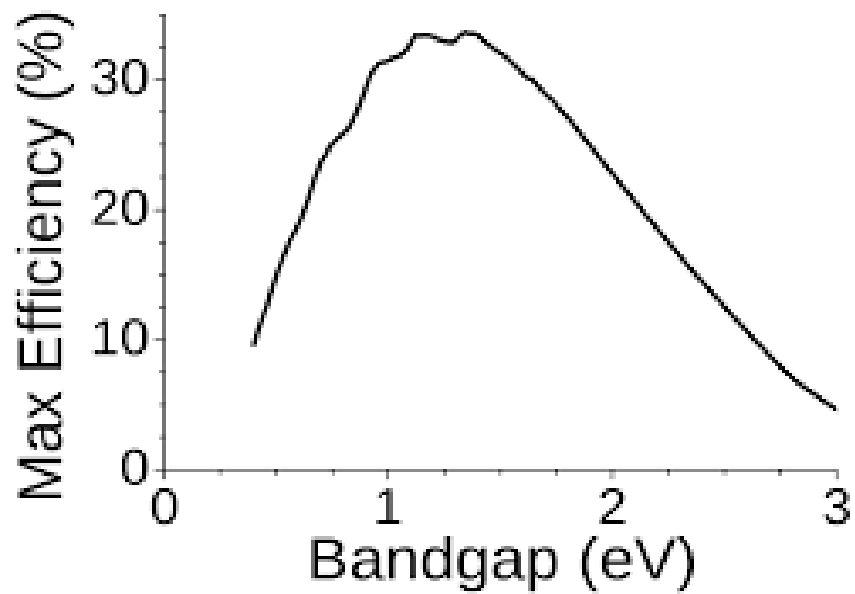


Figure 2.4: Solar cell maximum efficiency as a function of material band gap, as predicted by the Shockley–Queisser limit [29].

The semiconductor's bandgap (E_g) determines a single-junction solar cell's maximum conversion efficiency. Figure 2.5 shows a schematic of single-junction solar cell efficiency loss mechanisms. To make solar cells work better, we need to deal with lattice thermalization and photon transparency to sub-band gap photons [23].

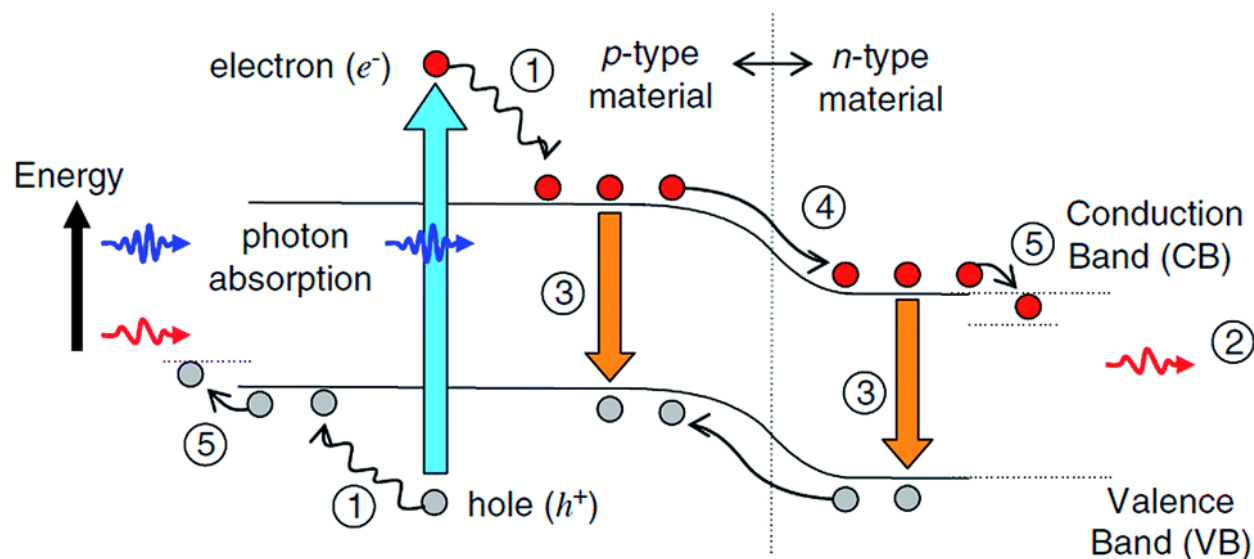


Figure 2.5: Single-junction solar cell loss mechanisms [23].

When a photon with higher or equal energy than the band gap is absorbed by a semiconductor, an electron-hole (charge carrier- the holes are called charge carriers because they are mobile, moving from atom site to atom site.) pair (also known as an e-h pair) with a higher energy is generated. The surplus energy is discharged as heat. This particular type of loss is referred to as "thermalization loss." Photons whose energies are lower than the band gap, on the other hand, are not absorbed by the semiconductor and are instead allowed to pass through. It has been found that solar cells that have a band gap that is narrow experience high thermalization losses, while solar cells that have a band gap that is wide experience high transmission losses [23, 31–32]. Another method by which energy is lost is through the recombination of e-h pairs that occur close to or at the surface [33]. Maintaining high minority carrier lifetimes in the semiconductor material can slow down this phenomenon. During transmission, heat loss and energy loss account for approximately 70% of the total energy loss. This phenomenon is referred to as

"spectral mismatch." This is primarily due to the fact that the solar spectrum and the band gap in semiconductors have different wavelengths. [23].

To deal with spectral mismatch, semiconductors with a decreasing band gap are used to make multi-junction solar cells with two to five junctions connected in series. The efficiency of solar cells has increased dramatically thanks to multi-junction solar cells, which almost double the efficiency of single-junction cells by using different wavelengths to cover a large portion of the sun's spectrum. At their theoretical best, multi-junction solar cells have been measured to be 43.5% efficient, which is significantly higher than the efficiency of any other single-junction solar cell [23, 34]. Multi-junction solar cells, on the other hand, are much harder to make than single-junction solar cells [35]. Since it is more complicated, it costs a lot more to make, which makes it too expensive for widespread use. As a result, most solar cells used today are single-junction cells. Researchers are looking into many ways to make single-junction solar cells better at absorbing light, separating charges, moving them, and collecting them. Even though there are many ways to collect light from a wide range of the sun's spectrum, photon absorption technology still needs to be improved so that highly efficient solar cells can be made [23]. Due to the way active semiconductor materials absorb light, PSCs are only able to harness a small part of the sun's electromagnetic spectrum, most of which falls within the visible spectrum. So, photons that are below or above these threshold values don't make electricity [36]. The PCE of PSCs could be greatly boosted if this energy were to be utilized.

Light photon wavelength conversions are a promising way to cut down on spectral mismatch losses, which are thought to be the main reason why single-junction solar cells lose most of their efficiency. Wavelength-dependent spectral converters have recently been looked into as a way to boost the way single-junction solar cells convert light into electricity. There are three different types of luminescence processes; quantum cutting, downshifting, and UC that have the potential to improve the performance of solar cells [37]. A single high-energy photon can be converted by quantum downconversion into several lower-energy photons, achieving a conversion efficiency of more than 100% in the process. High-energy photons can have some of their wasted energy recovered through a process known as "downconversion," which also incorporates the technique of "quantum cutting [38]." Solar cells have the ability to absorb photons that have been

downconverted, which helps to reduce the amount of energy that is wasted and increases the conversion's overall efficiency [39]. One type of downconversion is the process of downshifting, which transforms one high-energy photon that has been absorbed into one with a lower energy level. This process takes place at sub-unity quantum efficiencies. Quantum cutting and downshifting are connected in some way, but downshifting cannot be any more efficient than 100% of the time [40]. Downshifting is the process of converting shorter-wavelength UV light into longer-wavelength visible light, which solar cells respond to most favourably [23]. The transformation of photons with low energy into photons with high energy is referred to as the "UC process." It may be possible to convert light whose energies are less than the gap between the bands of a semiconductor because of this process. As a result, there would be a significant cut in the amount of energy that was lost during transmission. According to research that was published in 2002 by Trupke, Green, et al. [23], the process of upconverting sub-band gap light can have a significant impact on the efficiency with which solar cells convert light into electricity. They investigated a silicon solar cell system that had UC layers on the back of the device and had two sides. When concentrated sunlight was utilized, the system achieved a maximum energy conversion efficiency of 63.2%, whereas when non-concentrated sunlight was utilized, the system only achieved an efficiency of 47.6%. Research on solar cells, which convert light into electricity, has accelerated as a result of this model [23, 41–42]. The present research looks at how the UC photoluminescent (UPL) $\text{NaYF}_4:\text{Yb}^{3+},\text{Er}^{3+}$ and $\text{NaGdF}_4:\text{Yb}^{3+},\text{Nd}^{3+}$ nanocrystals can be used to make PSCs absorb more light and increase their PCE. Due to the UPL materials, which are anti-Stokes materials (luminescent materials which convert NIR laser light to visible light), can complete the UC process by absorbing two or more photons of NIR or infrared light (IR) and putting out one photon in the visible spectrum [42-44], these materials will be put in the active layer of PV cells to help the solar cell absorb more light. Figure 2.6 shows how $\text{NaYF}_4:\text{Yb}^{3+},\text{Er}^{3+}$ can be used in solar cells to change the wavelength of light.

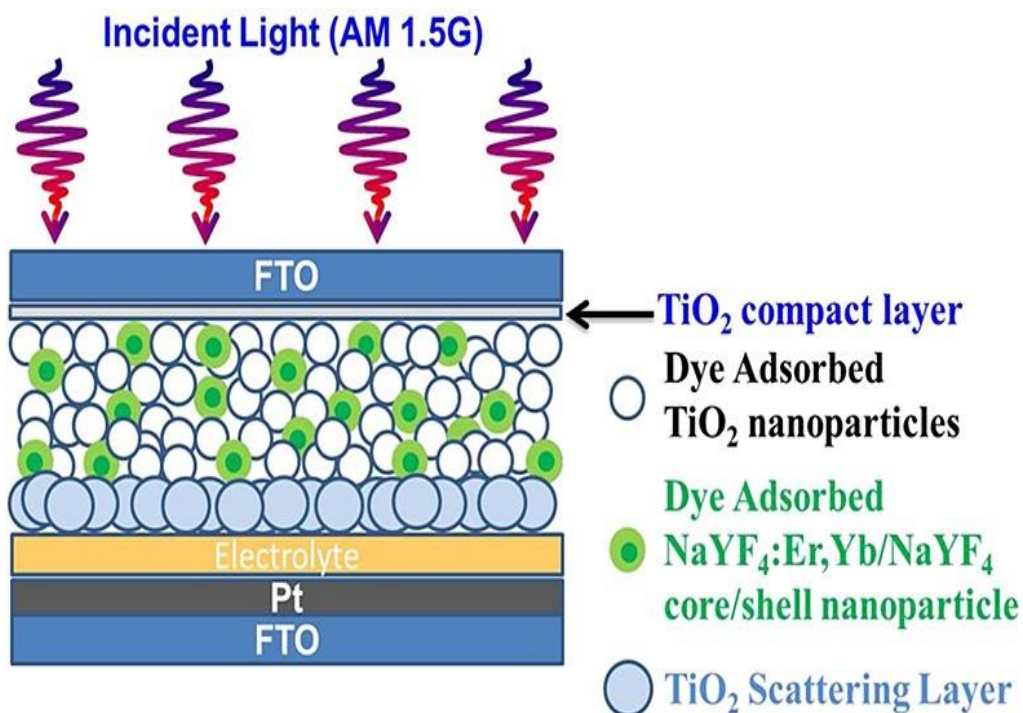


Figure 2.6: An illustration of $\text{NaYF}_4:\text{Yb}^{3+},\text{Er}^{3+}$ as spectral converters in solar cells [45].

2.3 UPCONVERSION MECHANISM

UC is a form of photoluminescence that uses multi-photon absorption to convert NIR excitation to visible light [23]. When two or more photons are absorbed one after the other, the photon UC process takes place, and light is emitted at a wavelength that is shorter than the excitation wavelength. Through various methods, this process occurs in both organic and inorganic materials. Transition metals, actinides, and primarily RE^{3+} elements containing the lanthanide (Ln) series, yttrium, and scandium, as well as organic molecules such as polycyclic aromatic hydrocarbons (PAHs) that can achieve photon UC through triplet-triplet annihilation, have all been observed to exhibit the UC phenomenon [46–49].

Some of the different UC luminescence mechanisms that were identified, either alone or in combination, are "excited state absorption (ESA), photon avalanche (PA), and energy transfer UC (ETU)" [47, 50–51]. In the case of ESA, excitation happens when a single ion in its ground state absorbs several pump photons.

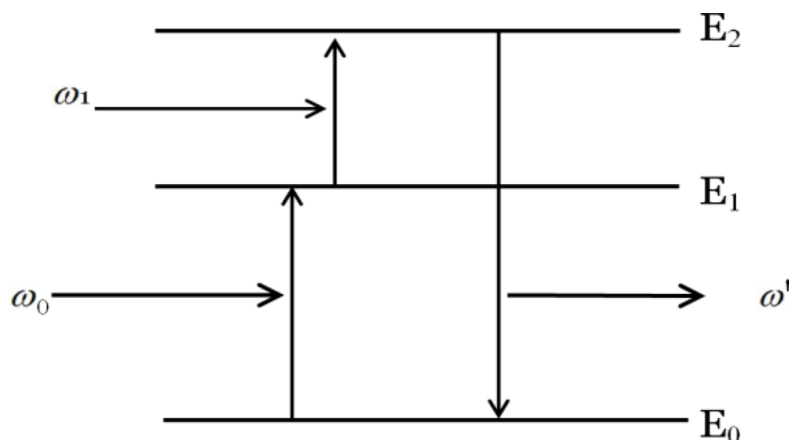


Figure 2.7: ESA procedure flowchart [52].

When an ion is excited from its ground state to the higher energy level (E_1), a second pump photon moves the ion from E_1 to the higher-lying state E_2 , which causes UC emission before the ion decays back to its ground state. (See Figure 2.7.). As a consequence of this, there will be emissions from a higher E_2 level that have been upconverted. In order for the extremely effective ESA to function, the ions' various levels of energy must be constructed in the shape of a ladder. Only a select few lanthanide ions, such as Er^{3+} , Ho^{3+} , Tm^{3+} , and Nd^{3+} , have energy levels that are structured in this manner; however, at this moment, these ions are the ones that are prevalent emitters (activators) in ESA-based UC nanomaterials. They also have an excellent excitation wavelength that is comparable to the output of diode lasers that are available for purchase (at either 975 or 808 nm) [52, 53-54].

Transmission, emission, and the gradual increase in pump power intensity are the three distinct nonlinear behaviours that are involved in the PA process. These three nonlinear behaviours contribute to the process's increased complexity [55]. In almost every instance, all three of these behaviours are followed by an essential pump threshold. In the four-energy system depicted below (figure 2.8), the notations E_0 , E_1 , E_2 , and E stand for the ground state, the intermediate state, and the upper excited state, respectively [56].

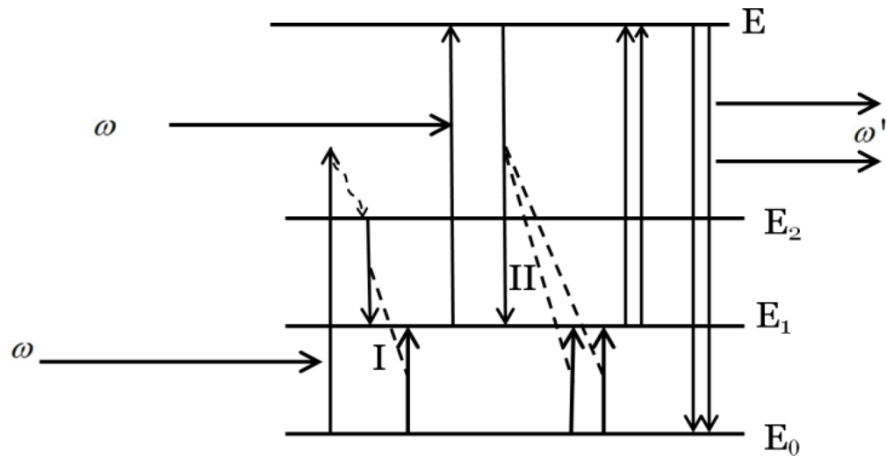


Figure 2.8: Illustration of the PA process [56].

An electron or ion becomes excited after absorbing excitation radiation. The transition that occurs during absorption, moving from the ground state to the intermediate states, is rarely resonant with excitation radiation, despite the fact that it is slightly higher than E_2 . The E_2 stage is reached through the process of cross-relaxation. Electrons in the excited state of E_2 and electrons in the ground state of E_0 are able to transfer their energy to one another. This results in a total of two electrons existing in the E_1 state. Excitation radiation is absorbed by one of these electrons, which then causes it to transition into the E state. After that, it engages in interactions with electrons in the E_0 state and undergoes energy transfer II, which results in the production of three electrons in the E_1 state. In this particular instance, the transition from E_1 to E is in resonance with the radiation that was responsible for causing the excitation. When the same things continue to happen over and over again, the total of all of the electrons that are in the E state will increase by a significant amount. When electrons move back to the E_0 state, they send out photons with a lot of energy. In short, the strong UC emission of the PA process is due to resonant ESA, effective cross relaxation, and a large reservoir level population [57]. PA has some problems, like a limited maximum output because of poor ground-state absorption and the need for a lot of pump power to reach the threshold condition [47, 58].

Both ETU and ESA achieve the metastable state by taking in two photons, one after the other. ETU and ESA are different in that ETU uses two lanthanide ions while ESA only uses one.

After the consumption of a pump photon, an excitation occurs in the ion 1 of the sensitizer, which raises it from the ground state to the metastable level E_1 . "Following the consumption of energy, the sensitizer ion 1 returns to its ground state, denoted by the letter G." Ion 2 is then able to transition into its higher emission state E_2 as a result of the transfer of this energy from its ground state G to its excited state E_1 . For an illustration of this, please refer to figure 2.9. The UC efficiency of the ETU UC process is significantly influenced by the dopant concentration, which modifies the distance that separates adjacent dopant ions. Due to the fact that the UC efficiency is directly proportional to the dopant concentration, this is the result. "The UC efficiency in an ESA process is unaffected by the concentration of the dopant because there is only one ion concentration in play" [58].

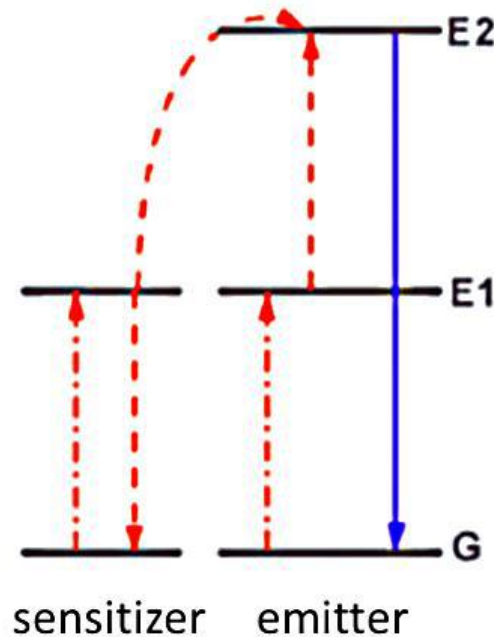


Figure 2.9: Energy transfer mechanism for upconversion process [59].

2.4 LUMINESCENT MATERIALS

Materials that absorb incident solar radiation and then radiate it outward in the form of photons are referred to as luminescent materials [60]. The Stokes Law governs the behaviour of luminous materials such as "organic dyes and quantum dots (QDs)" [61–64]. Materials that are used for downconversion absorb high-energy light and then send out light with less energy (energy reduction). However, low-energy, long-wavelength NIR light can be converted into higher-energy visible or UV light with the help of UCNCs. This mechanism can also take the form of the UC luminescence (UCL) phenomenon, which is also referred to as the anti-Stokes process [65–69].

Nano-lasers, nanophosphors, biological nanolabels, and other photonic applications have contributed to the sudden rise in popularity of the luminous nanoparticles, as have near-field microscopy applications such as temperature sensing and the identification of surface plasmon polariton (SPP) waves. Doping nanoparticles with RE^{3+} elements create luminescence bands from the UV to the IR, as well as multi-color UCL. "Frequency UPL of nanoparticles is essential in many contexts, including the detection of single-photon-emitting photons (SPP), IR nanophosphors, nanolasers, nanolabels, and other nanosensors." REs are comprised of 15 lanthanides, yttrium, and scandium. Due to their remarkable $4f$ electron layout level of energy, REs are able to experience a bandgap transition when the majority of the trivalent RE^{3+} ions are excited from outside. This allows REs to be used in a variety of applications. In addition, the secondary $5s^25p^6$ shell that surrounds the RE^{3+} ions protect them from the surrounding environment [65].

2.5 LANTHANIDE-BASED UP CONVERTERS

Trivalent RE^{3+} ions, such as Pr^{3+} , Nd^{3+} , Er^{3+} , Tm^{3+} , or Yb^{3+} , are the active parts of most popular UC phosphors. However, there are other types as well. The fact that the important electronic states for spectroscopy are in the inner $4f$ shell of these ions explains why most of the research in the field has been done on this small group of ions. The f states are not very concerned with the specific structure of the host lattice because both their $5s$ and $6p$

shells engage in bonding (i.e., "the exact crystal field and, to a lesser extent, the local site symmetry"). As a consequence of this, many of the excited f states persist for sufficient amounts of time for UC procedures to be carried out. Auzel, Ovsyankin, and Feofilov all independently discovered RE³⁺ ions around the middle of the 1960s [70]. The mentioned ions were the first to show UC [52, 71–72].

At room temperature, the vast majority of inorganic crystals do not exhibit UCL; rather, the luminous centre is frequently provided by the dopants that are present in the crystal. Therefore, a good lanthanide-based upconverter requires at least two things: (1) a very stable host material to act as a shield, and (2) an efficient dopant ion to act as a light source. Both of these things can be found in lanthanide compounds [73]. When the dopant ion in sensitized luminescence is excited to a higher energy state, it emits radiation as a result of the process. Radiation is produced as a byproduct of the process of exciting the dopant ion in sensitized luminescence to a higher energy state. This process causes the dopant ion to transition into a higher energy state. This occurs when the energy required to perform the experiment is extracted from a dopant ion in a way that does not need the use of radiation. The ion that releases the radiation is referred to as an "activator," while the ion that releases the energy is referred to as a "sensitizer." Even though UCL can be seen in a large number of lanthanide activator–sensitizer combinations and most crystalline composites can be used as hosts, UC only works well in a few carefully chosen combinations of dopant and host [52].

2.5.1 Activators

In theory, most lanthanide ions are expected to emit UC emissions. The difference in energy between every excited level and its lower-lying intermediate level must be close enough to allow the absorption of photons and energy transfer steps needed in UC processes to produce UC emissions that can be widely used. Some lanthanide ions cannot be excited in this manner because their energy level structures are not beneficial. As shown in Figure 2.11, Er³⁺, Tm³⁺, and Ho³⁺ are right now the most prevalent types of emitters found in UC phosphors. This is because their energy levels are set up like a ladder. The energy gap between the various energy levels in Er³⁺ is roughly the same, leading to a very high UC efficiency. For example, the difference in energy between the

$^4I_{11/2}$ and $^4I_{15/2}$ levels of Er^{3+} is the same as the difference between the $^4F_{7/2}$ and $^4I_{11/2}$ levels. So, the energy levels of $^4I_{15/2}$, $^4I_{11/2}$, and $^4F_{7/2}$ can be used to make UC emission by excitation at 980 nm. Also, because the difference in energy between the $^4F_{9/2}$ and $^4I_{13/2}$ states is in the same region, 980 nm excitation causes at least three distinct changes in Er^{3+} ions, which cause green and red light to be emitted after two photons are absorbed [46, 52].

Laporte does not allow $4f-4f$ transitions, so if the excited light is not absorbed enough, UCL isn't as bright, especially in thin samples of lanthanide-doped materials. In general, the material's absorption can be improved by adding more lanthanide ions. But multi-phonon relaxation that doesn't involve radiation can happen, and cross-relaxation makes it much harder to use an extensive variation in the amount of dopants. The efficiency with which energy is converted depends on a number of factors, including the number of intermediate and emission levels and the rate of non-radiative multi-phonon relaxation between energy levels. The multi-phonon relaxation rate constant k_{nr} is described by the following equation (2.1) for lanthanide ion $4f$ levels.

$$k_{nr} \propto \exp\left(-\beta \frac{\Delta E}{\hbar\omega}\right) \quad (2.1)$$

where β denotes the empirical standard of the host, ΔE is the energy gap between the occupied level and the following lower-lying energy level of a lanthanide ion, and $\hbar\omega$ is the highest energy vibrational mode of the host matrix.

Er^{3+} and Tm^{3+} have very wide energy gaps, as illustrated in Figure 2.10 (a–c), and consequently low likelihoods of non-radiative transitions between different excited states of the ions. According to the energy gap law, the UCNCs that are made with Er^{3+} and Tm^{3+} as activators are the most effective ones, and this is widely known to this day [52]. The proposed energy transfer mechanism is shown in Figure 2.10 (d) [52].

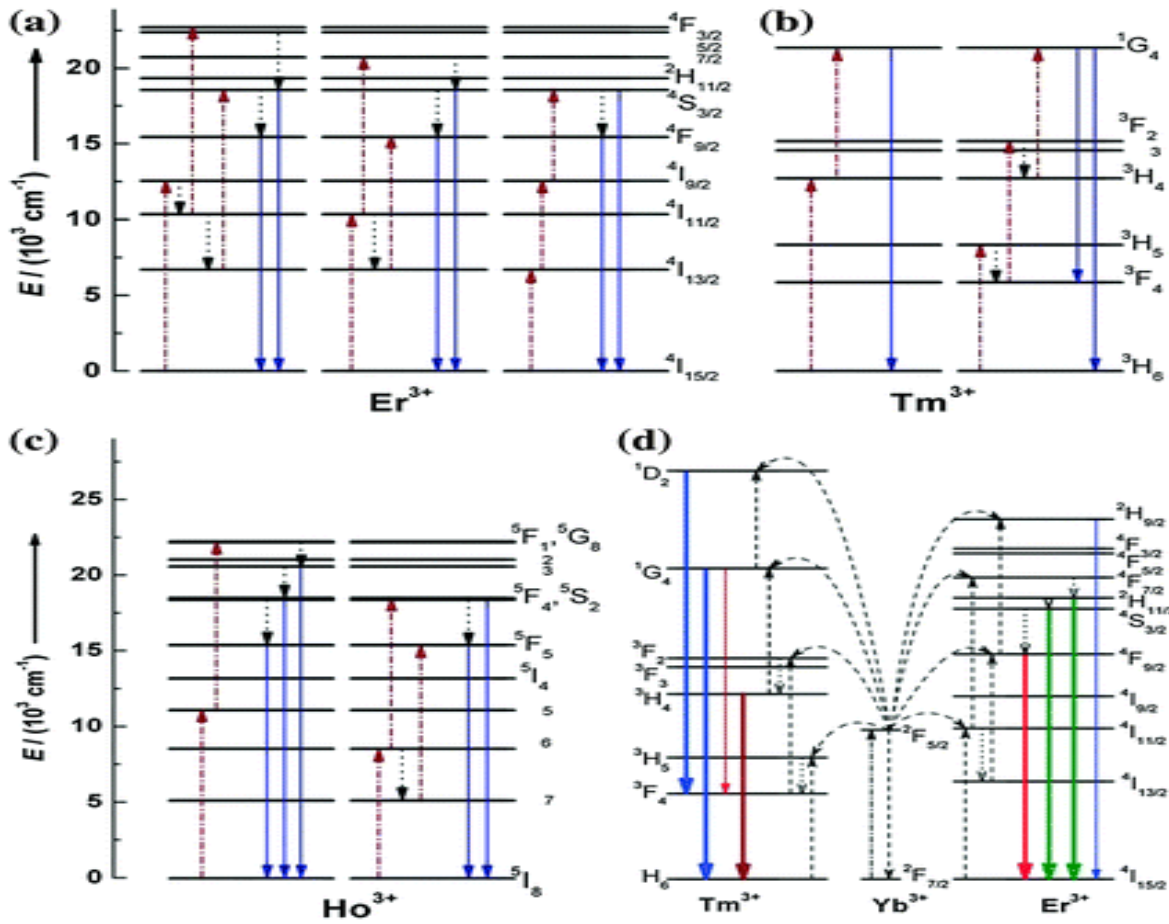


Figure 2.10 Simplified energy level diagrams of typical (a) Er^{3+} , (b) Tm^{3+} , (c) Ho^{3+} and (d) energy transfer mechanism [52].

2.5.2 Sensitizers

Cross-relaxation severely restricts a variety of effective doping concentrations for doped UCNs. Excitation energy may be quenched as a result of high doping levels. To prevent the quenching effect, the activator ion concentration should be kept low and well controlled [74]. However, when viewed from a different perspective, low doping levels can result in low pump light absorption, which in turn leads to high emission luminescence efficiency. Sensitizers, which are strongly absorbing ions, are often added to the host material to improve the absorption of phosphors that have been doped with lanthanides and make sure that energy gets to the activator efficiently [52, 75-77].

Co-doping a sensitizer that has a large cross-sectional area of absorption in the NIR region can make UCL work much better. Co-doping the sensitizer with the activator is often done to benefit from the efficient manner in which the ETU process operates between the activator and the sensitizer. Most of the time, Yb^{3+} - Er^{3+} and Yb^{3+} - Tm^{3+} ions are used as sensitizer-activator combinations. Yb^{3+} has a simple energy level scheme, with one excited $4f$ level of $^2\text{F}_{5/2}$ (see Figure 2.11d). "The energy difference between the $^4\text{I}_{11/2}$ and $^4\text{I}_{15/2}$ and the $^4\text{F}_{7/2}$ and $^4\text{I}_{11/2}$ states of Er^{3+} and the energy separation between the $^2\text{F}_{7/2}$ ground state and its $^2\text{F}_{5/2}$ excited state of Yb^{3+} are similar." This allows effective energy transfer between the two ions [78]. Tm^{3+} and Ho^{3+} both work on the same premise. Yb^{3+} is ideal for use as a sensitizer for UC because of its optical properties. Most of the time, Yb^{3+} is co-doped into the lattice at high amounts (18–20 mol%), whereas the activator concentration is kept low (2 mol%), which limits the loss of energy from cross-relaxation [46, 52, 77].

2.5.3 Host Materials

The features of the host lattice and the manner in which it interacts with dopants have a significant impact on the UC process in two different ways: (i) through the movement of phonons and (ii) through the local crystal field [79]. The energy exchange interactions between dopant ions are highly influenced by the host lattice, which promotes f - f electronic transitions among lanthanide ions by perturbing the $4f$ wave function with crystal fields. This is critical for energy transmission between lanthanide ions, which are often characterized by narrow emission and absorption bands that make spectral overlap difficult. The crystalline structure of the host material's lattice determines how far apart the dopant ions are, their location in relation to each other, how many of them there are, and what kind of anions are around them [80]. UCL has been seen in several lanthanide-doped host materials, although highly effective emission requires low phonon energy and a tiny lattice discrepancy between the dopants and the crystal lattice [65, 81].

A good host matrix should have low lattice phonon energy so that nonradiative losses are kept to a minimum and radiative emission is increased [65, 82–84]. Most of the time, the phonon energies of heavy halides like chlorides, bromides, and iodides are less than 300

cm^{-1} [85]. However, they absorb water, so they are not very useful. "Oxides are chemically stable, but their phonon energies are often higher than 500 cm^{-1} because of the stretching vibration of the host lattice [52]. Fluorides, on the other hand, have low phonon energies (350 cm^{-1}) and good chemical stability, which makes them perfect host materials for UC [52, 86]. Semiconductor nanocrystals, such as ZnS, have been proposed as UC host materials alongside the aforementioned materials. Whether the lanthanide ions in these nanocrystals are uniformly distributed in the host lattice or placed on the nanocrystals' outermost layer is still unclear due to the size discrepancy between the host and dopant ions" [52].

Since all trivalent lanthanide ions are the same size and have the same chemical properties, inorganic compounds based on trivalent lanthanide ions are good hosts for UC phosphors [87]. Crystal defects and lattice stress can be kept to a minimum by using host lattices composed of cations like Na^+ , Ca^{2+} , Sr^{2+} , and Ba^{2+} , whose ionic radii are comparable to those of the lanthanide dopant ions [52]. It is for this reason that Na^+ and Ca^{2+} fluorides are typically good host materials for UC phosphors. In conclusion, the best host materials for UC are fluorides based on Na^+ , Ca^{2+} , and Y^{3+} . In comparison to $\text{La}_2\text{O}_3:\text{Yb}^{3+},\text{Er}^{3+}$ and $\text{La}_2(\text{MoO}_4)_3:\text{Yb}^{3+},\text{Er}^{3+}$, $\text{NaYF}_4:\text{Yb}^{3+},\text{Er}^{3+}$ has a 20-fold higher UC efficiency [52, 86].

"The crystal structure of the host material could have a big effect on how UC materials behave optically. At this moment, hexagonal NaYF_4 ($\beta\text{-NaYF}_4$) is considered to be the most effective fluoride host material for green and blue UC phosphors. The efficiency of UC in bulk materials composed of hexagonal-phase $\text{NaYF}_4:\text{Yb}/\text{Er}$ is almost ten times higher than that of cubic-phase materials [88]." It is possible to establish a direct connection between the phase-dependent optical property and the various crystal fields that are located around trivalent lanthanide ions in matrices that have varying degrees of symmetry. In contrast to their counterparts with greater symmetry, hosts with low symmetry have a tendency to make a crystal field around the dopant ions that has more uneven parts than their counterparts with high symmetry. The electronic coupling between higher electronic configurations and the $4f$ energy levels is improved by the uneven parts. Due to this, there is an increased possibility that the dopant ions will move from the f level to the f level. Additionally, the efficiency of the UC can be improved by

decreasing the size of the host cations (or the volume of the unit cell), which strengthens the crystal field that surrounds the dopant ions. This can be accomplished by decreasing the volume of the unit cell. For instance, the UCL of NaYF₄:Yb/Er in bulk is two times as bright as that of NaLaF₄:Yb/Er [52, 86–89].

2.6 THERMOLUMINESCENT MATERIALS

Thermoluminescence (TL) is a type of luminescence that occurs in particular types of crystalline solids, such as "feldspar, lithium fluoride, calcium fluoride, calcium sulfate, lithium borate, calcium borate, and potassium bromide [90]." When heated, these materials emit light again after having previously absorbed energy from ionizing radiation or electromagnetic radiation. Additionally, the substance must be translucent due to its light emissions [91]. The basic principle of TL is that an insulating material contains defects, impurities, and imperfections. During the excitation of the sample, these lattice sites may acquire electrons and holes. Later, during heating, these charge carriers may recombine and result in the emission of light in the form of a TL glow curve (see figure 2.12) [92-93].

TL materials have a vast range of uses in fields like environmental dosimetry, medical research, and personal dosimetry. The characteristics of materials useful for a vast range of applications in a variety of fields are changed by introducing a variety of RE impurities into a variety of hosts. These materials can be exposed to a variety of beams, including electron, neutron, X-ray, and β -ray beams. TL dosimetry is highly dependent on the different radiation regimes and their dose-response range [94]. Lithium fluoride and calcium fluoride are the two most popular TL materials used in dosimetry, both of which contain an impurity or multiple impurities (such as manganese or magnesium) that develop states that can trap electrons with high energy. Following irradiation, the impurity enables the formation of electron traps within the crystalline lattice. The trapped electrons are released when the crystal is heated, which ultimately leads to the production of light. The radiation dose that the crystal receives has an impact on how much light is produced. Figure 2.11 illustrates the TL mechanism [95-96]. An electron is captured in a trap site as part of the activation process. The trap site needs to be deep enough to prevent the

electron from being removed quickly at the storage temperature. Ionizing radiation and light both have the ability to activate. After the sample has been turned on, it is heated to perform the readout. When the temperature reaches a certain point, the electrons undergo a process known as thermal excitation, which causes them to move into the conduction band. These conduction electrons are able to move freely around the lattice until they come across a hole, which allows them to unwind and stop moving. The centre of the hole is excited and emits if it has an emissive centre or is located near one. As an alternative, the relaxation of the hole could be emissive [95]. A material with characteristic TL signal can be proposed a dosimeter if it possess the linearity of signal with dose over a wide range [97].

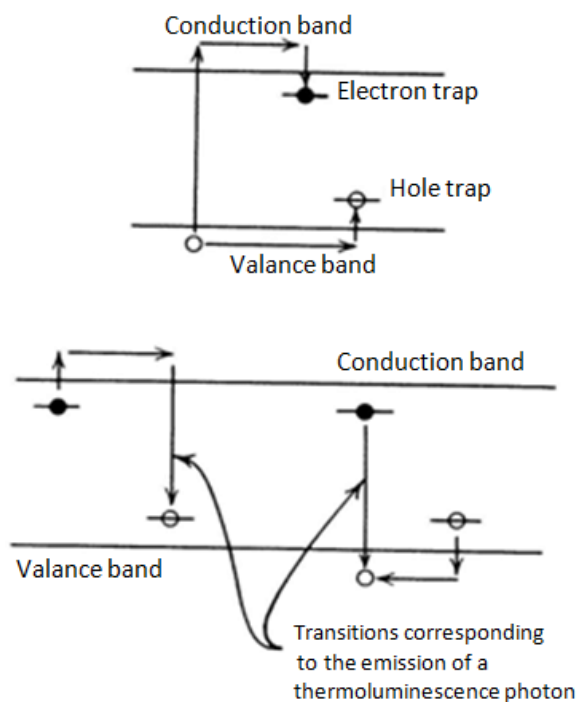


Figure 2.11: Thermoluminescence mechanism [96].

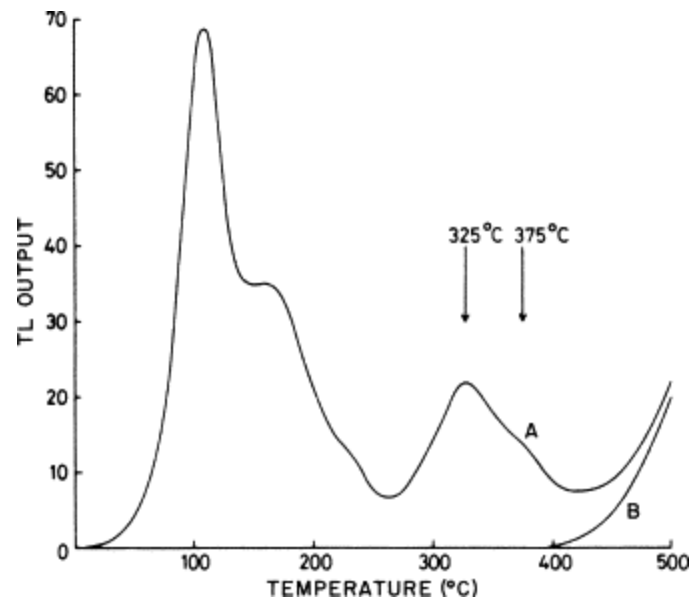


Figure 2.12: Thermoluminescence mechanism [95].

References

- [1]. Bodapati, J.B., 2011. *Novel Donor-Acceptor Polymers for Solar Cells* (Doctoral dissertation, Eastern Mediterranean University (EMU)).
- [2]. Dima, R.S., 2018. *Density functional theory study of TiO₂ Brookite (100), (110) and (210) surfaces doped with ruthenium (RU) and platinum (Pt) for application in dye sensitized solar cells* (Masters dissertation).
- [3]. Stranks, S.D. and Snaith, H.J., 2015. Metal-halide perovskites for photovoltaic and light-emitting devices. *Nature nanotechnology*, 10 (5), pp.391-402.
- [4]. Werner, J., Niesen, B. and Ballif, C., 2018. Perovskite/silicon tandem solar cells: Marriage of convenience or true love story?—An overview. *Advanced Materials Interfaces*, 5 (1), p.1700731.
- [5]. Bagher, A.M., Vahid, M.M.A. and Mohsen, M., 2015. Types of solar cells and application. *American Journal of optics and Photonics*, 3(5), pp.94-113.
- [6]. Tonui, P., Oseni, S.O., Sharma, G., Yan, Q. and Mola, G.T., 2018. Perovskites photovoltaic solar cells: An overview of current status. *Renewable and Sustainable Energy Reviews*, 91, pp.1025-1044.
- [7]. El Chaar L, El Zein N. Review of photovoltaic technologies. *Renewable and sustainable energy reviews*, June 1st, 2011; 15 (5) 2165-75.
- [8]. Sharma, K., Sharma, V. and Sharma, S.S., 2018. Dye-sensitized solar cells: fundamentals and current status. *Nanoscale research letters*, 13 (1), p.381.
- [9]. Yan J, Saunders BR. Third-generation solar cells: a review and comparison of polymers: fullerene, hybrid polymer and perovskite solar cells. *Rsc Advances*. 2014; (482):43286-314.
- [10]. Adil SF, Khan M, Kalpana D. Graphene-based nanomaterials for solar cells. In *Multifunctional Photocatalytic Materials for Energy* 2018 Jan 1 (pp. 127-152). Woodhead Publishing.
- [11]. Su, Q., Zhang, G., Lai, J., Feng, S. and Shi, W., 2010. Green solar electric vehicle changing the future lifestyle of human. *World electric vehicle journal*, 4(1), pp.128-132.

- [12]. Pushparaj, T.L., Raj, E., Rani, E., Darwin, S. and Appadurai, M., 2022. Employing Novel Si-Over-Si Technology to Optimize PV Effect in Solar Array. *Silicon*, pp.1-13.
- [13]. Hernandez-Garcia, C., O Shea, P.G. and Stutzman, M.L., 2008. Electron sources for accelerators. *Physics today*, 61(2), p.44.
- [14]. El Chaar, L. and El Zein, N., 2011. Review of photovoltaic technologies. *Renewable and sustainable energy reviews*, 15(5), pp.2165-2175.
- [15]. Tilley, R.J., 2010. *Colour and the optical properties of materials: an exploration of the relationship between light, the optical properties of materials and colour*. John Wiley & Sons.
- [16]. Pode, R. and Diouf, B., 2011. Solar Photovoltaic Electricity. In *Solar Lighting* (pp. 19-59). Springer, London.
- [17]. Jena, A.K., Kulkarni, A. and Miyasaka, T., 2019. Halide perovskite photovoltaics: background, status, and future prospects. *Chemical reviews*, 119 (5), pp.3036-3103.
- [18]. Ansari, M.I.H., Qurashi, A. and Nazeeruddin, M.K., 2018. Frontiers, opportunities, and challenges in perovskite solar cells: A critical review. *Journal of Photochemistry and Photobiology C: Photochemistry Reviews*, 35, pp.1-24.
- [19]. Green, M.A., 2000. Photovoltaics: technology overview. *Energy policy*, 28(14), pp.989-998.
- [20]. Arjunan, A.T. and Senthil, T.S., 2013. Dye sensitised solar cells. *Materials Technology*, 28(1-2), pp.9-14.
- [21]. Elumalai, N.K., Mahmud, M.A., Wang, D. and Uddin, A., 2016. Perovskite solar cells: progress and advancements. *Energies*, 9 (11), p.861.
- [22]. Krishna, B.G., Rathore, G.S., Shukla, N. and Tiwari, S., 2021. Perovskite solar cells: A review of architecture, processing methods, and future prospects. *Hybrid Perovskite Composite Materials*, pp.375-412.
- [23]. Ramasamy, P., Manivasakan, P. and Kim, J., 2014. Upconversion nanophosphors for solar cell applications. *Rsc Advances*, 4(66), pp.34873-34895.

- [24]. García de Arquer, F.P., Armin, A., Meredith, P. and Sargent, E.H., 2017. Solution-processed semiconductors for next-generation photodetectors. *Nature Reviews Materials*, 2(3), pp.1-17.
- [25]. Luque, A. and Hegedus, S. eds., 2011. *Handbook of photovoltaic science and engineering*. John Wiley & Sons.
- [26]. Berka, M., Hebali, M., Bey, A.B. and Mahdjoub, Z., 2018. Optimization of Technological Qualities of Photovoltaic Cells Based on Absorber Metamaterial (SRRs) Resonators. *Majlesi Journal of Mechatronic Systems*, 7(3), pp.9-16.
- [27]. Jäger, K.D., Isabella, O., Smets, A.H., van Swaaij, R.A. and Zeman, M., 2016. *Solar energy: fundamentals, technology and systems*. UIT Cambridge.
- [28]. Lutz, J., Schlangenotto, H., Scheuermann, U. and De Doncker, R., 2011. Semiconductor power devices. *Physics, characteristics, reliability*, 2.
- [29]. Reinders, A., Verlinden, P., Van Sark, W. and Freundlich, A., 2017. *Photovoltaic solar energy: from fundamentals to applications*. John Wiley & Sons.
- [30]. Ischenko, A.A., Fetisov, G.V. and Aslalnov, L.A., 2014. *Nanosilicon: properties, synthesis, applications, methods of analysis and control*. CRC Press.
- [31]. Moyez, A., Dhar, A., Sarkar, P., Jung, H.S. and Roy, S., 2016. A review of the multiple exciton generation in photovoltaics. *Reviews in Advanced Sciences and Engineering*, 5(1), pp.51-64.
- [32]. Ma, T., Guo, Z., Shen, L., Liu, X., Chen, Z., Zhou, Y. and Zhang, X., 2021. Performance modelling of photovoltaic modules under actual operating conditions considering loss mechanism and energy distribution. *Applied Energy*, 298, p.117205.
- [33]. Thomas, D.G., Hopfield, J.J. and Augustyniak, W.M., 1965. Kinetics of radiative recombination at randomly distributed donors and acceptors. *Physical Review*, 140(1A), p.A202.
- [34]. Lian, H., Hou, Z., Shang, M., Geng, D., Zhang, Y. and Lin, J., 2013. Rare earth ions doped phosphors for improving efficiencies of solar cells. *Energy*, 57, pp.270-283.

- [35]. Meusel, M., Baur, C., Siefert, G., Dimroth, F., Bett, A.W. and Warta, W., 2006. Characterization of monolithic III–V multi-junction solar cells—challenges and application. *Solar energy materials and solar cells*, 90(18-19), pp.3268-3275.
- [36]. Ghazy, A., Safdar, M., Lastusaari, M., Savin, H. and Karppinen, M., 2021. Advances in upconversion enhanced solar cell performance. *Solar Energy Materials and Solar Cells*, 230, p.111234.
- [37]. Day, J., Senthilarasu, S. and Mallick, T.K., 2019. Improving spectral modification for applications in solar cells: A review. *Renewable Energy*, 132, pp.186-205.
- [38]. Sekar, R., Ravitchandiran, A. and Angaiah, S., 2022. Recent Advances and Challenges in Light Conversion Phosphor Materials for Third-Generation Quantum-Dot-Sensitized Photovoltaics. *ACS omega*, 7(40), pp.35351-35360.
- [39]. Imenes, A.G. and Mills, D.R., 2004. Spectral beam splitting technology for increased conversion efficiency in solar concentrating systems: a review. *Solar energy materials and solar cells*, 84(1-4), pp.19-69.
- [40]. Richards, B.S. and Shalav, A., 2007. Photovoltaics devices. *The Handbook of Photonics*, 2.
- [41]. Yang, W., Li, X., Chi, D., Zhang, H. and Liu, X., 2014. Lanthanide-doped upconversion materials: emerging applications for photovoltaics and photocatalysis. *Nanotechnology*, 25(48), p.482001.
- [42]. Liu, S.M., Chen, W. and Wang, Z.G., 2010. Luminescence nanocrystals for solar cell enhancement. *Journal of nanoscience and nanotechnology*, 10(3), pp.1418-1429.
- [43]. Fan, Q., Ma, R., Liu, T., Su, W., Peng, W., Zhang, M., Wang, Z., Wen, X., Cong, Z., Luo, Z. and Hou, L., 2020. 10.13% Efficiency All-Polymer Solar Cells Enabled by Improving the Optical Absorption of Polymer Acceptors. *Solar RRL*, 4(6), p.2000142.
- [44]. Kesavan, A.V. and Ramamurthy, P.C., 2021. Photo-active polymer nanocomposite layer for energy applications. In *Polymer-based advanced functional composites for optoelectronic and energy applications* (pp. 135-156). Elsevier.

- [45]. Chander, N., Khan, A.F., Komarala, V.K., Chawla, S. and Dutta, V., 2016. Enhancement of dye sensitized solar cell efficiency via incorporation of upconverting phosphor nanoparticles as spectral converters. *Progress in Photovoltaics: Research and Applications*, 24(5), pp.692-70.
- [46]. Haase, M. and Schäfer, H., 2011. Upconverting nanoparticles. *Angewandte Chemie International Edition*, 50(26), pp.5808-5829.
- [47]. Chen, J. and Zhao, J.X., 2012. Upconversion nanomaterials: synthesis, mechanism, and applications in sensing. *Sensors*, 12 (3), pp.2414-2435.
- [48]. Cates, E.L., Chinnapongse, S.L., Kim, J.H. and Kim, J.H., 2012. Engineering light: advances in wavelength conversion materials for energy and environmental technologies. *Environmental science & technology*, 46(22), pp.12316-12328.
- [49]. Safdar, M., Ghazy, A., Lastusaari, M. and Karppinen, M., 2020. Lanthanide-based inorganic–organic hybrid materials for photon-upconversion. *Journal of Materials Chemistry C*, 8(21), pp.6946-6965.
- [50]. Bednarkiewicz, A., Chan, E.M., Kotulska, A., Marciniak, L. and Prorok, K., 2019. Photon avalanche in lanthanide doped nanoparticles for biomedical applications: super-resolution imaging. *Nanoscale Horizons*, 4(4), pp.881-889.
- [51]. Levy, E.S., Tajon, C.A., Bischof, T.S., lafrati, J., Fernandez-Bravo, A., Garfield, D.J., Chamanzar, M., Maharbiz, M.M., Sohal, V.S., Schuck, P.J. and Cohen, B.E., 2016. Energy-looping nanoparticles: harnessing excited-state absorption for deep-tissue imaging. *ACS nano*, 10(9), pp.8423-8433.
- [52]. Zhang, F., 2015. *Photon upconversion nanomaterials* (Vol. 416). Berlin, Germany: Springer.
- [53]. Chen, G., Qiu, H., Prasad, P.N. and Chen, X., 2014. Upconversion nanoparticles: design, nanochemistry, and applications in theranostics. *Chemical reviews*, 114(10), pp.5161-5214.
- [54]. Richards, B.S., Hudry, D., Busko, D., Turshatov, A. and Howard, I.A., 2021. Photon upconversion for photovoltaics and photocatalysis: a critical review: focus review. *Chemical Reviews*, 121(15), pp.9165-9195.

- [55]. Kobayashi, Y. and Abe, J., 2022. Recent advances in low-power-threshold nonlinear photochromic materials. *Chemical Society Reviews*.
- [56]. Solé, J., Bausa, L. and Jaque, D., 2005. *An introduction to the optical spectroscopy of inorganic solids*. John Wiley & Sons.
- [57]. Mi, C., Wu, J., Yang, Y., Han, B. and Wei, J., 2016. Efficient upconversion luminescence from Ba₅Gd₈Zn₄O₂₁: Yb³⁺, Er³⁺ based on a demonstrated cross-relaxation process. *Scientific reports*, 6(1), p.22545.
- [58]. Huang, H., Zhou, H., Zhou, J., Wang, T., Huang, D., Wu, Y., Sun, L., Zhou, G., Zhan, J. and Hu, J., 2017. Enhanced anti-stokes luminescence in LaNbO₄: Ln³⁺ (Ln³⁺= Yb³⁺, Er³⁺/Ho³⁺/Tm³⁺) with abundant color. *RSC Advances*, 7(27), pp.16777-16786.
- [59]. Awan, A.B., and Z.A. Khan, 2014. Recent advances in renewable energy—A remedy for Pakistan's energy crisis. *Renewable and Sustainable Energy Reviews*, 33, pp.236-253.
- [60]. Corrado, C., Leow, S.W., Osborn, M., Chan, E., Balaban, B. and Carter, S.A., 2013. Optimization of gain and energy conversion efficiency using front-facing photovoltaic cell luminescent solar concentrator design. *Solar Energy Materials and Solar Cells*, 111, pp.74-81.
- [61] Debije, M.G. and Verbunt, P.P., 2012. Thirty years of luminescent solar concentrator research: solar energy for the built environment. *Advanced Energy Materials*, 2(1), pp.12-35.
- [62]. Rakovich, Y.P., Donegan, J.F., Vasilevskiy, M.I. and Rogach, A.L., 2009. Anti-Stokes cooling in semiconductor nanocrystal quantum dots: A feasibility study. *physica status solidi (a)*, 206(11), pp.2497-2509.
- [63]. Nguyen, T.N., Ebrahim, F.M. and Stylianou, K.C., 2018. Photoluminescent, upconversion luminescent and nonlinear optical metal-organic frameworks: From fundamental photophysics to potential applications. *Coordination Chemistry Reviews*, 377, pp.259-306.

- [64]. Hajagos, T.J., Liu, C., Cherepy, N.J. and Pei, Q., 2018. High-Z sensitized plastic scintillators: a review. *Advanced Materials*, 30(27), p.1706956.
- [65]. Altavilla, C. ed., 2016. *Upconverting nanomaterials: perspectives, synthesis, and applications*. CRC Press.
- [66]. Hong, E., Liu, L., Bai, L., Xia, C., Gao, L., Zhang, L. and Wang, B., 2019. Control synthesis, subtle surface modification of rare-earth-doped upconversion nanoparticles and their applications in cancer diagnosis and treatment. *Materials Science and Engineering: C*, 105, p.110097.
- [67]. Hu, Z., Lin, Z., Su, J., Zhang, J., Chang, J. and Hao, Y., 2019. A review on energy band-gap engineering for perovskite photovoltaics. *Solar Rrl*, 3(12), p.1900304.
- [68]. Soni, A.K. and Singh, B.P., 2019. Luminescent materials in lighting, display, solar cell, sensing, and biomedical applications. In *Luminescence-OLED Technology and Applications* (p. 1). London, UK: IntechOpen.
- [69]. Xin, N., Wei, D., Zhu, Y., Yang, M., Ramakrishna, S., Lee, O., Luo, H. and Fan, H., 2020. Upconversion nanomaterials: A platform for biosensing, theranostic and photoregulation. *Materials Today Chemistry*, 17, p.100329.
- [70]. Lian, H., Hou, Z., Shang, M., Geng, D., Zhang, Y. and Lin, J., 2013. Rare earth ions doped phosphors for improving efficiencies of solar cells. *Energy*, 57, pp.270-283.
- [71]. Vasconcelos, H.C. and Pinto, A.S., 2017. Fluorescence properties of rare-earth-doped sol-gel glasses. *Recent Applications in Sol-Gel Synthesis*, pp.81-107.
- [72]. Soares, M.R.N., 2016. *Development of zirconia based phosphors for application in lighting and as luminescent bioprobes* (Doctoral dissertation, Universidade de Aveiro (Portugal)).
- [73]. Qin, X., Xu, J., Wu, Y. and Liu, X., 2019. Energy-transfer editing in lanthanide-activated upconversion nanocrystals: a toolbox for emerging applications. *ACS Central Science*, 5(1), pp.29-42.
- [74]. Vennerberg, D. and Lin, Z., 2011. Upconversion nanocrystals: synthesis, properties, assembly and applications. *Science of Advanced Materials*, 3(1), pp.26-40.

- [74]. Chen, B. and Wang, F., 2019. Combating concentration quenching in upconversion nanoparticles. *Accounts of Chemical Research*, 53(2), pp.358-367.
- [76]. Han, S., Deng, R., Xie, X. and Liu, X., 2014. Enhancing luminescence in lanthanide-doped upconversion nanoparticles. *Angewandte Chemie International Edition*, 53(44), pp.11702-11715.
- [77]. Tu, L., Liu, X., Wu, F. and Zhang, H., 2015. Excitation energy migration dynamics in upconversion nanomaterials. *Chemical Society Reviews*, 44(6), pp.1331-1345.
- [78]. Park, C.W. and Park, D.J., 2021. Development of Er³⁺, Yb³⁺ Co-Doped Y₂O₃ NPs According to Yb³⁺ Concentration by LP-PLA Method: Potential Further Biosensor. *Biosensors*, 11(5), p.150.
- [79]. Lummen, T.T.A., Handayani, I.P., Donker, M.C., Fausti, D., Dhalenne, G., Berthet, P., Revcolevschi, A. and Van Loosdrecht, P.H.M., 2008. Phonon and crystal field excitations in geometrically frustrated rare earth titanates. *Physical review B*, 77(21), p.214310.
- [80]. Rupp, J.L., Fabbri, E., Marrocchelli, D., Han, J.W., Chen, D., Traversa, E., Tuller, H.L. and Yildiz, B., 2014. Scalable oxygen-ion transport kinetics in metal-oxide films: impact of thermally induced lattice compaction in acceptor doped ceria films. *Advanced Functional Materials*, 24(11), pp.1562-1574.
- [81]. Kar, A., Kundu, S. and Patra, A., 2015. Lanthanide-Doped Nanocrystals: Strategies for Improving the Efficiency of Upconversion Emission and Their Physical Understanding. *ChemPhysChem*, 16(3), pp.505-521.
- [82]. Shalav, A., Richards, B.S. and Green, M.A., 2007. Luminescent layers for enhanced silicon solar cell performance: Up-conversion. *Solar energy materials and solar cells*, 91(9), pp.829-842.
- [83]. Singh, A.K., Singh, S.K. and Rai, S.B., 2014. Role of Li⁺ ion in the luminescence enhancement of lanthanide ions: favorable modifications in host matrices. *RSC advances*, 4(51), pp.27039-27061.

- [84]. Tian, Q., Yao, W., Wu, W. and Jiang, C., 2019. NIR light-activated upconversion semiconductor photocatalysts. *Nanoscale Horizons*, 4(1), pp.10-25.
- [85]. Güdel, H.U. and Pollnau, M., 2000. Near-infrared to visible photon upconversion processes in lanthanide doped chloride, bromide and iodide lattices. *Journal of alloys and compounds*, 303, pp.307-315.
- [86]. Rennero-Lecuna, C., Martín-Rodríguez, R., Valiente, R., González, J., Rodríguez, F., Kramer, K.W. and Güdel, H.U., 2011. Origin of the high upconversion green luminescence efficiency in β -NaYF₄: 2% Er³⁺, 20% Yb³⁺. *Chemistry of Materials*, 23(15), pp.3442-3448.
- [87]. Suyver, J.F., Aebischer, A., Biner, D., Gerner, P., Grimm, J., Heer, S., Krämer, K.W., Reinhard, C. and Güdel, H.U., 2005. Novel materials doped with trivalent lanthanides and transition metal ions showing near-infrared to visible photon upconversion. *Optical materials*, 27(6), pp.1111-1130.
- [88]. Yi, G.S. and Chow, G.M., 2006. Synthesis of hexagonal-phase NaYF₄: Yb, Er and NaYF₄: Yb, Tm nanocrystals with efficient up-conversion fluorescence. *Advanced Functional Materials*, 16(18), pp.2324-2329.
- [89]. Lahtinen, S., Lyytikäinen, A., Pääkilä, H., Hömppi, E., Perälä, N., Lastusaari, M. and Soukka, T., 2017. Disintegration of hexagonal NaYF₄: Yb³⁺, Er³⁺ upconverting nanoparticles in aqueous media: the role of fluoride in solubility equilibrium. *The Journal of Physical Chemistry C*, 121(1), pp.656-665.
- [90]. Tugay, H., Yegingil, Z.E.H.R.A., Dogan, T.A.M.E.R., Nur, N. and Yazici, N., 2009. The thermoluminescent properties of natural calcium fluoride for radiation dosimetry. *Nuclear Instruments and Methods in Physics Research Section B: Beam Interactions with Materials and Atoms*, 267(23-24), pp.3640-3651.
- [91]. De Oliveira, J.P., de Oliveira, M.J., da Silva, I.C., Varca, G.H. and Lugão, A.B., 2017. Influence of different gamma radiation doses on PVA/gelatin based scaffolds. *NUTECH-2017*, p.27.
- [92]. Chen, R., 2006. Dose Dependence of Thermoluminescence (TL) and Optically Stimulated Luminescence with Uniform Excitation. In *Microdosimetric Response of*

Physical and Biological Systems to Low-and High-LET Radiations (pp. 253-330). Elsevier Science.

[93]. McKeever, S.W., 1988. *Thermoluminescence of solids* (Vol. 3). Cambridge University Press.

[94]. Duragkar, A., Muley, A., Pawar, N.R., Chopra, V., Dhoble, N.S., Chimankar, O.P. and Dhoble, S.J., 2019. Versatility of thermoluminescence materials and radiation dosimetry—A review. *Luminescence*, 34(7), pp.656-665.

[95]. Veltri, S., Pantano, P., Bonanno, A. and Antici, P., 2017. *Nano materials and innovative laser-based accelerators for cultural heritage* (Doctoral dissertation).

[96]. Rahman, M.O., Hoque, M.A., Rahman, M.S. and Begum, A., 2015. Responses of LiF Thermoluminescence Dosimeters to Diagnostic ⁶⁰Co Teletherapy Beams. *Bangladesh Journal of Medical Physics*, 8(1), pp.14-21.

[97]. Basun, S., Imbusch, G.F., Jia, D.D. and Yen, W.M., 2003. The analysis of thermoluminescence glow curves. *Journal of Luminescence*, 104(4), pp.283-294.

CHAPTER 3

Theory of Research Techniques and Synthesis methods

3.1 INTRODUCTION

This chapter gives a high-level summary of the research methods that were used to characterize the nanocrystals that were prepared. XRD, field-emission scanning electron microscopy (FE-SEM), TGA, fourier-transform infrared spectroscopy (FTIR), ultraviolet, visible, and near-infrared (UV-VIS-NIR) spectroscopy, TL spectroscopy, and PL spectroscopy are the techniques that have been utilized. The crystalline phases and crystallite sizes of the nanocrystals were determined with the assistance of the XRD. The morphological and elemental features of the nanocrystals were investigated with the help of a FE-SEM that was coupled with an energy dispersive spectroscopy (EDS). TGA analysis was used to investigate the nanocrystals' ability to withstand high temperatures. In order to identify the various functional groups that were present in the samples, FTIR was utilized. Through the use of UV-VIS-NIR spectroscopy, the nanocrystals' absorbance value was estimated. In order to record the UC spectra of the samples, PL was utilized. The vibrational modes of the molecules were observed using Raman spectroscopy. The defects in the nanocrystals were evaluated using TL spectroscopy.

3.2 SYNTHESIS OF POWDER NANOCRYSTALS

The preparation methods of UC nanocrystals have a strong influence on their luminescent characteristics. The size, shape, and matching microstructure of luminous materials will be affected by different preparation procedures, resulting in a wider range of applications. The most widely utilized methods include thermal decomposition, hydrothermal, co-precipitation, the sol-gel process, and the solution combustion method [1]. Among these methods, solution combustion (SC) processing has been found to offer many advantages, including high purity of the products, low energy requirements, relative simplicity, and

rapid processing [2]. Due to the aforementioned advantages, the SC process was employed in this study to synthesize the $\text{NaYF}_4\text{:Yb}^{3+}/\text{Er}^{3+}$ and $\text{NaGdF}_4\text{:Yb}^{3+}/\text{Nd}^{3+}$ nanopowders. The fundamental concepts of the SC process are discussed in the following section.

3.2.1 Solution combustion process

Solution combustion method (SC), also known as "self-propagating high-temperature synthesis (SHS)," is an efficient and cost-effective method for the production of a variety of oxide materials [3]. Compared to other methods of synthesis, exothermic combustion processes are more energy-efficient because they can keep process temperatures high. It also enables the efficient and cost-effective manufacturing of nanoparticles with the phase compositions that are desired. This is made possible by its relatively low heating rates of 350-600 °C, quick heating rates, and short reaction times.

The precursors for SC synthesis are mostly redox mixes. An organic molecule such as urea, citric acid, or the polymer PVA (polyvinyl alcohol) serves as the reducing agent (fuel). A metal salt, such as nitrate, is used as an oxidizing agent [4-5]. Water has traditionally been the most often utilized solvent in the SC synthesis of powder materials [6]. Recently, environmentally friendly solvents, such as ethanol and water, have gained popularity for electronic applications; however, organic solvents, such as 2-methoxyethanol and acetonitrile, are currently the most extensively employed for the manufacture of oxide thin films for electronic applications [7]. The resultant solution is heated to evaporate the solvent, and the exothermic reaction occurs when the ignition temperature is reached. The nitrate ions oxidize the fuel during the combustion reaction. The precursor elements are transformed into metal oxide, and the residual products of the combustion reaction are gaseous H_2O , CO_2 , and N_2 . In theory, this method may be used for any metal ion [8-9]. The presence of a large amount of gas produced by combustion causes large particles to disintegrate into nanoparticles [4]. Figure 3.1 below illustrates a typical SC process.

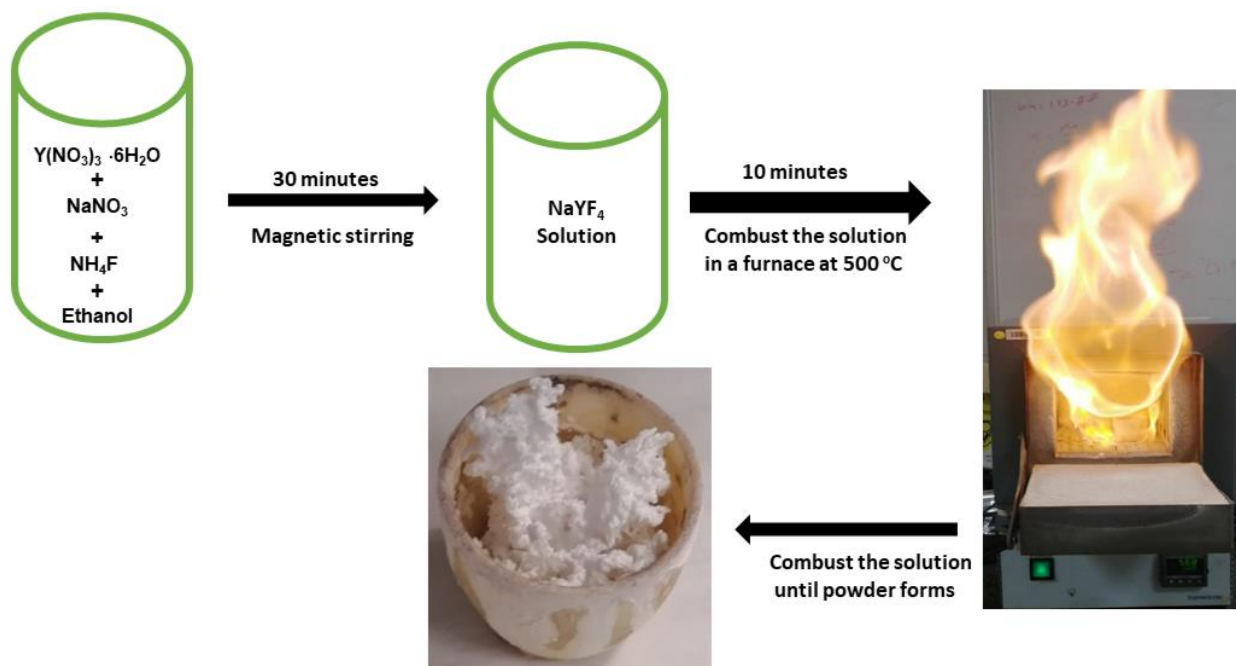
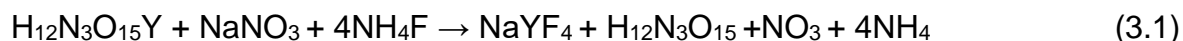


Figure 3.1: Schematic diagram of the solution combustion synthesis of nanocrystals.

3.2.2. Experimental details

3.2.2.1 Solution combustion synthesis of NaYF₄ nanocrystals

The chemical reagents used in this study were graded analytically and applied directly from Sigma-Aldrich without any additional purification steps. NaYF₄ was synthesized by dissolving 4.06 g of Yttrium (III) nitrate hexahydrate [Y(NO₃)₃·6H₂O, 99.8%], 0.90 g sodium nitrate (NaNO₃, 99.0%), 1.57 g ammonium fluoride (NH₄F, 99.99%), and 2.08 g urea (98%) in 20 ml of ethanol (99.8%). The clear solution was poured into a crucible and placed inside the furnace, which was preheated at 500 °C for 20 minutes. Once the temperature of the product had returned to normal, it was crushed into a fine powder with a mortar and pestle and annealed for 2 hours at 600 °C and 700 °C. Urea was used as a fuel because it speeds up the rate of combustion and goes through a process of decomposition that could help lower the temperature of combustion. The chemical reaction involved in the growth of the NaYF₄ nanocrystals is shown in equation 3.1 below.

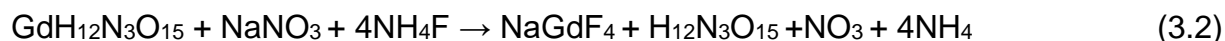


3.2.2.2 Solution combustion synthesis of Yb³⁺-Er³⁺ co-doped NaYF₄ nanocrystals.

For the preparation of Yb³⁺-Er³⁺ co-doped NaYF₄ with various Yb³⁺ and Er³⁺ doping concentrations, stoichiometric amounts of Ytterbium (iii) nitrate pentahydrate [Yb(NO₃)₃ .5H₂O ≥99.9%] erbium (iii) nitrate pentahydrate [Er(NO₃)₃ .5H₂O, 99.9%], corresponding to 10,20,30 and 1,2,3 mol% respectively doping levels were dissolved together with 4.07 g of Y(NO₃)₃ .6H₂O, 0.92 g NaNO₃, 1.52 g NH₄F, and 2.06 g urea in 20 ml of ethanol with Constant agitation with the temperature set at room temperature for 30 minutes. The clear solution was poured into a crucible and placed inside the furnace, which was preheated at 500 °C for 20 minutes. After allowing the product to reach room temperature, it was ground into a fine powder using a mortar and pestle and then annealed at temperatures of 600 and 700 °C.

3.2.2.3 Solution combustion synthesis of NaGdF₄ nanocrystals

The combustion method was used to synthesize NaGdF₄ nanocrystals by dissolving 3.54 g of gadolinium (iii) nitrate hexahydrate [Gd (NO₃)₃.6H₂O, 99 %], 0.68 g of sodium nitrate (NaNO₃ 99.0 %), 1.15 g of ammonium fluoride (NH₄F 99.99 %), and 2.07 g of urea (≥98%) in 20 ml of ethanol (≥99.8%), with constant stirring at room temperature for 30 minutes. The clear solution was poured into a crucible and placed inside the furnace, which was preheated at 500 °C for 20 minutes. After allowing the product to reach room temperature, it was ground into a fine powder using a mortar and pestle and then annealed at temperatures of 600 and 700 °C. The chemical reaction involved in the growth of the NaGdF₄ nanocrystals is shown in equation 3.2 below.



3.2.2.4 Solution combustion synthesis of Yb³⁺-Nd³⁺ co-doped NaGdF₄ nanocrystals

For the preparation of Yb³⁺-Nd³⁺ co-doped NaGdF₄ with various Yb³⁺ and Nd³⁺ doping concentrations, stoichiometric amounts of Ytterbium (iii) nitrate pentahydrate [Yb(NO₃)₃ .5H₂O ≥99.9%], neodymium (iii) nitrate hexahydrate [Nd(NO₃)₃ .6H₂O, 99.9%], corresponding to 10,20,30 and 1,2,3 mol% respectively doping levels were dissolved together with 3.54 g of Gd(NO₃)₃ .6H₂O, 0.68 g NaNO₃, 1.15 g NH₄F, and 2.03 g urea in 20 ml of ethanol with vigorous stirring at room temperature for 30 minutes. The clear solution was poured into a crucible and placed inside the furnace, which was preheated at 500 °C for 20 minutes. After cooling the product to room temperature, it was crushed into a fine powder with a mortar and pestle.

3.2.2.5 Characterization of the nanocrystals

An X-ray diffractometer (Cu K, 45 kV, and 200 mA) from the Rigaku SmartLab was used to determine the crystallite phase of the nanocrystals that were produced. An Oxford Aztec 350 X-Max 80 electron dispersive spectrometer (EDS) was coupled with a JEOL JSM-7800 F field emission scanning electron microscope in order to investigate morphology. Fourier transform infrared spectroscopy (FTIR) spectra were obtained using a SHIMADZU-IRTracer-100 instrument with a resolution of 4.0 cm⁻¹ and 10 scans. In order to investigate the vibrational modes of molecules, an XploRA PLUS Raman microscope was utilized. The quantification of absorbance was carried out with the assistance of a PerkinElmer Lambda 1050 UV/Vis/NIR spectrophotometer. For the purpose of measuring the UC of the samples, a Horiba, Jobin Yvon Fluorolog 3 Photoluminescence Spectrometer, and a continuous LED laser beam with a wavelength of 980 nm were utilized. An investigation into the thermal stability of the NaYF₄:20%Yb³⁺,2%Er³⁺ and NaGdF₄:20%Yb³⁺,2%Nd³⁺ samples was conducted by the SDT (TGA) Q600 TA Instruments from room temperature to 700 °C with a nitrogen flow rate of 60 ml/min and a heating rate of 10 °C/min. Measurements of TL were obtained from a Ris TL/OSL reader of model DA-20 by utilizing the BG-B9 (2 nm) filter.

3.3 CHARACTERIZATION TECHNIQUES

3.3.1 X-ray Diffractometer

X-ray diffraction (XRD) is a method for analyzing the crystal structure of substances [10]. It can also be used to distinguish between amorphous and crystalline substances, ascertain grain size, determine solid composition, measure lattice constants, and measure the degree of crystallinity [11]. An XRD analysis involves shining a collinear X-ray beam of a known wavelength onto the sample and recording the angles at which the beam diffracts. The crystallite size, size distribution, flaws, and strain of nanocrystals all have an effect on the widths of the diffraction lines. Loss of long-range order causes the line width to increase as crystallite size decreases relative to bulk crystals [12]. Crystallite size can be determined using Scherrer's equation (equation 3.3) [13], but it only works for particles on the nanometer scale and has no relevance for grains larger than about 0.1 μm .

$$D = \frac{K\lambda}{\beta \cos\theta} \quad (3.3)$$

where K is an arbitrary dimensionless shape factor that has a value relatively close to one, and D denotes the average dimension of the crystallized domains, which may be less than or comparable to the grain size. The shape factor typically ranges from about 0.89 to 0.91, depending on the specific shape of the crystallite being examined. X-rays have different wavelengths (λ) depending on their origin. After subtracting the instrumental line broadening, the value that is left over for the line broadening at half the maximum intensity (FWHM) is given in radians. Bragg's angle is denoted by θ and is measured in radians [13]. Figure 3.2 shows the general structure of the XRD system in diagram form.

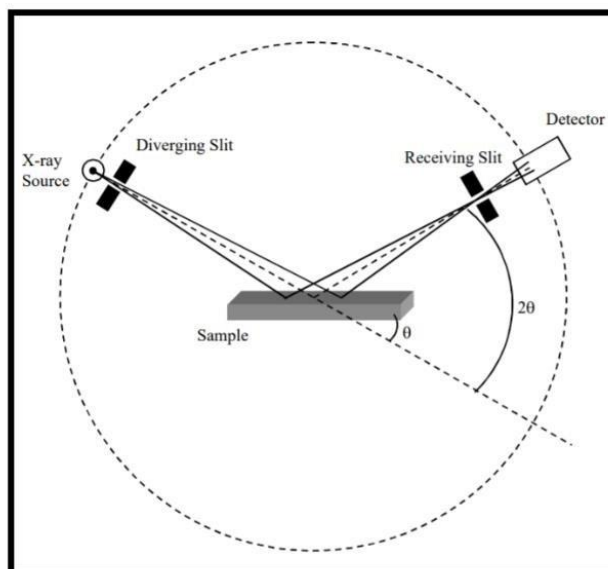


Figure 3.2 Schematic representation of the X-ray diffractometer system [14].

3.3.2 Field-emission scanning electron microscopy

Scanning electron microscopy (SEM) is a way to make pictures of a sample by moving an electron beam back and forth over it [15]. The technique can show information about a material's surface and shape, and when the system is connected to an energy dispersive X-ray spectrometer (EDS), it can also show information about the elements that make up the material. FE-SEM uses a field emission source, which makes an image that is clearer, has fewer electrostatic misalignments, and has a spatial resolution of less than 2 nm. The main idea behind the system is that when an electron beam hits a surface, it creates a splash of secondary electrons with much lower kinetic energies than the main electrons that hit the surface [12].

Before SEM testing in most cases and also in this work, the sample is sputter coated with gold, platinum, or carbon and placed on a stub for analysis. Sputter coating is a method that can be used in conjunction with a high-voltage SEM to achieve superior results by adding a layer of protection to the samples being examined. Coatings reduce the charging in samples, making them easier to analyse. Both the operation of the instrument and the

monitoring of the scanned images are carried out by a computer that is connected to the device being scanned. "Following the formation of a vacuum, the specimen is fastened to an exchange rod, and after that, the electron column is wired up to the scanning electron microscope (SEM). Following the placement of the stub within the sample holder within the electron column, the sample position must be adjusted to be straight, and the electron column must be closed. After all of the necessary adjustments to the working distance and magnification have been made, the controller is then used to take the images" [16]. Figure 3.2 depicts a simple SEM layout, which includes an electron gun, a magnetic lens for forming the beam and limiting the amount of current in the beam, and detectors. A system of ion optics focuses electrons produced by thermionic emission from an electron gun down to a location on the sample (i.e., electromagnetic coils). The spot is moved across the entirety of the surface of the sample using a set of scan coils, and the electrons that are reflected back are then collected, amplified, and converted into a video signal. As a result of this, a micrograph of the specimen is obtained in the form of a 2D plot of the reflected spot [11].

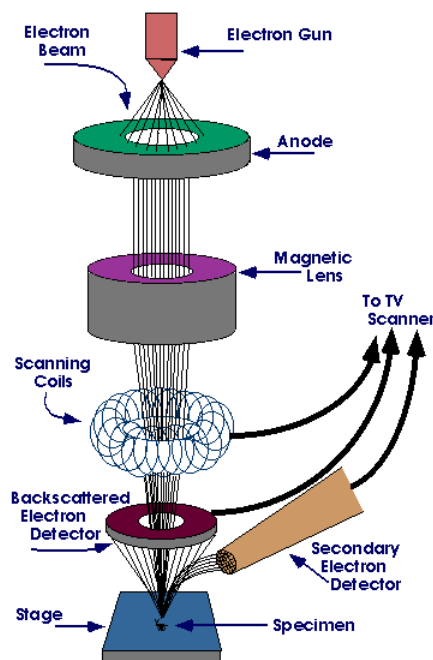


Figure 3.3 A simplified SEM layout [11].

3.3.3 Thermogravimetric analysis

Thermogravimetric analysis (TGA) is a process that monitors the change in weight that a sample undergoes in response to being heated uniformly in order to determine a material's thermal stability and the quantity of volatile components [17]. It analyses the composition, purity, decomposition processes, decomposition temperature, and absorbed moisture content of the products [18]. TGA enables one to comprehend how the mass of material changes with respect to both time and temperature. In this method, the sample is heated from room temperature to a temperature of 1,000 degrees in either nitrogen or air. Following this step, the amount of weight loss that occurs because of semi-volatile chemicals, the breakdown of polymer chains, ash content, carbon black, and moisture is measured. Loss of solvent due to surface absorption can be distinguished from loss of solvent due to degradation and loss of solvent in the crystal lattice. In order to determine interactions with the drug substance, between drug substances, and between active ingredients and excipients or packaging materials, measurements are done in environments where the levels of oxygen and humidity can be precisely controlled [18–19]. Figure 3.4 below shows a picture of the TGA instrument.

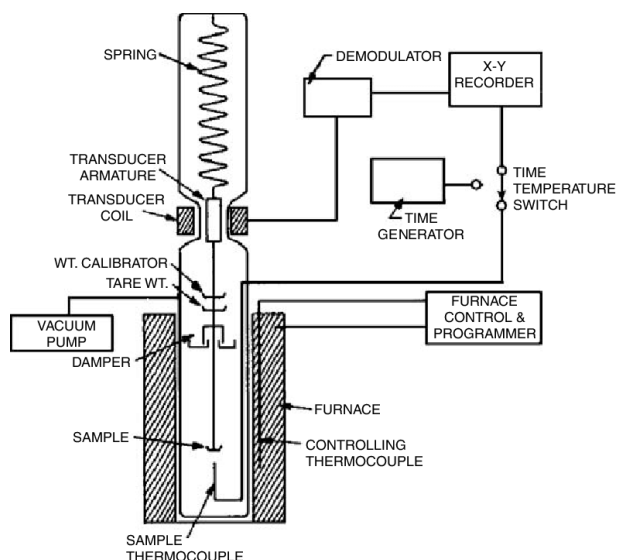


Figure 3.4 Schematic diagram of TGA setup [18].

3.3.4 Fourier-transform infrared spectroscopy

Fourier transform infrared spectroscopy (FTIR) is a way to find out how solid, liquid, and gaseous materials absorb, emit, and conduct light in the infrared spectrum. It is used to figure out which functional groups are in a sample [20]. FTIR can be used to detect and classify unknown substances, find impurities in a material, determine what additives are present, and determine whether a material is degrading or oxidizing [8]. The FTIR spectrum is captured between 4000 and 400 cm^{-1} [20-21]. For FTIR analysis, an FTIR instrument sends infrared light with a wavelength between 10,000 and 100 cm^{-1} through a material. Some of the light is absorbed, and some of it passes through. Radiation is taken in by the sample molecules, which change it into rotational and/or vibrational energy. The signal that comes out of the detector is on a spectrum that goes from 4000 cm^{-1} to 400 cm^{-1} . This spectrum shows the molecular fingerprint of the sample. FTIR analysis is a great way to identify chemicals because every molecule or chemical structure has its own spectral fingerprint [22].

The components of a regular FTIR spectrometer are the "source, sample cell, detector, amplifier, A/D converter, and computer." After passing through the interferometer, the radiation from the sources is picked up by the detector. Together, the A/D converter and amplifier boost the signal and convert it to digital form. The Fourier transform is then performed on the digital signal in the computer [21]. This FTIR spectrometer's operational principles are depicted in Figure 3.5.

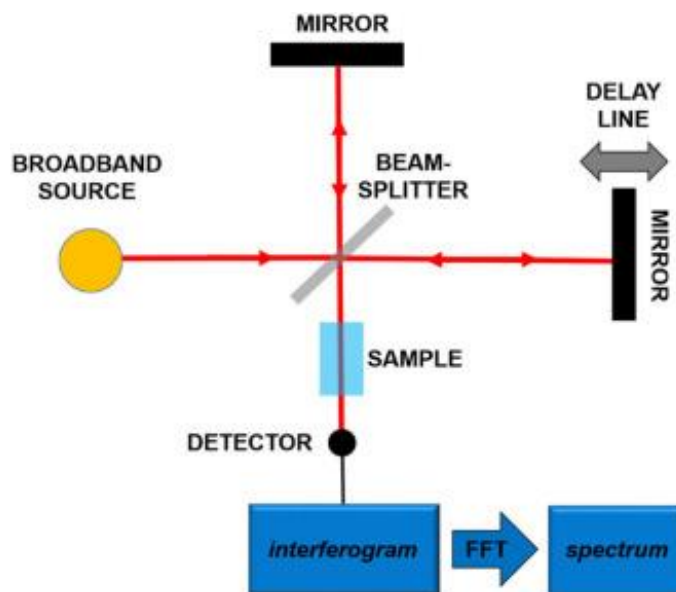


Figure 3.5: An illustration showing the schematic layout of an FTIR spectrometer [21].

3.3.5 Ultraviolet, Visible, and near-infrared system

The optical characterization technique known as ultraviolet-visible-near-infrared (UV-Vis-NIR) spectrophotometry [23] is used to measure the reflectance, transmission, and absorption of light by both liquids and solids without causing any damage to them. Light passing through a sample is measured against its initial intensity, I_0 . The transmittance is denoted as a percentage (%T) and is calculated as the ratio of the input (I) to the output (I_0). The transmittance is used to figure out the absorbance (A) given by equation 3.4 below [24]:

$$A = -\log \left(\frac{\%T}{100} \right) \quad (3.4)$$

There are three kinds of spectrophotometers: single beam, double beam, and split beam. The intensity of light is measured by the single beam UV-Vis-NIR spectrophotometers before and after the sample is placed. Split beam variations send one beam through a control sample and the other through the sample being examined [24]. When determining the amount of light that passes through solid samples, the integrating sphere is positioned

in front of the sample. Light coming from an optical light source is allowed to pass into the integrating sphere after passing through the sample. After that, the light is reflected off the interior surface of the sphere and sent back toward the detector. It is possible to measure both the overall transmittance and the direct transmittance. The diffuse transmittance can be calculated using these two parameters as given by equation 3.5 below [25]:

$$T_{\text{diff}} = T_{\text{overall}} - T_{\text{direct}} \quad (3.5)$$

When determining the transmittance of a solid sample, an integrating sphere is necessary, just as it is when measuring the sample's reflectance. The sample is kept in a location that is posterior to the integrating sphere. The sample is responsible for reflecting light coming from the optical light source; this light is then reflected by the interior surface of the integrating sphere before it is detected by the instrument. In addition to the overall reflectance, diffuse reflectance is also able to be evaluated. The following equation, which can be used to calculate specular reflectance based on overall and diffuse reflectance data, is given below [25]:

$$R_{\text{spec}} = R_{\text{overall}} - R_{\text{diff}} \quad (3.6)$$

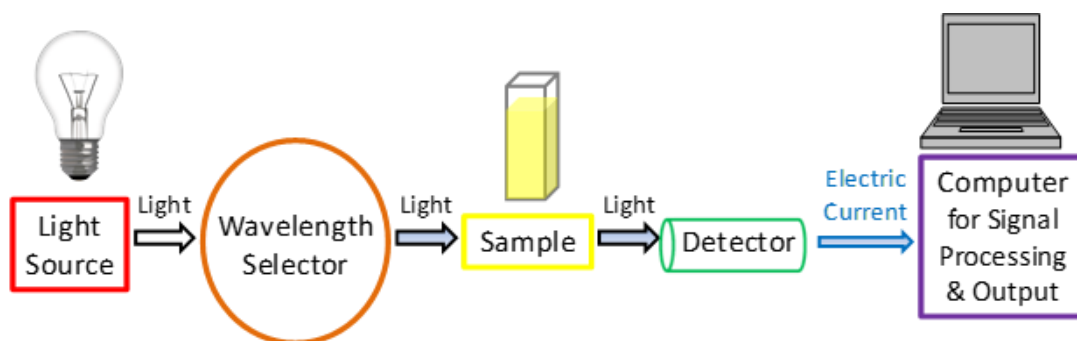


Figure 3.6: Simplified diagram of the basic UV-Vis-NIR spectrophotometer components [26].

3.3.6 Photoluminescence Spectroscopy

Photoluminescence (PL) spectroscopy is a method for investigating the electronic structure of materials without destroying them [27]. It is straightforward, adaptable, and non-destructive [11]. In a typical PL experiment, photons with an energy greater than the band-gap energy are used to stimulate a semiconductor. The semiconductor Bloch equations can be used to describe the polarization created by the incoming light. After the photons are absorbed, electrons and holes are created in the conduction and valence bands, respectively, with finite momenta k . The excitations then go through an energy and momentum relaxation process as they approach the band-gap minimum. Two common mechanisms are coulomb scattering and phonon interaction. Finally, the electrons recombine with holes, and photons are emitted [28-29]. Figure 3.7 depicts a typical PL configuration. Sample preparation is minimal because the measurement does not rely on electrical excitation or detection. This property makes PL particularly appealing for materials with low conductivity or underdeveloped contact or connection technologies [11].

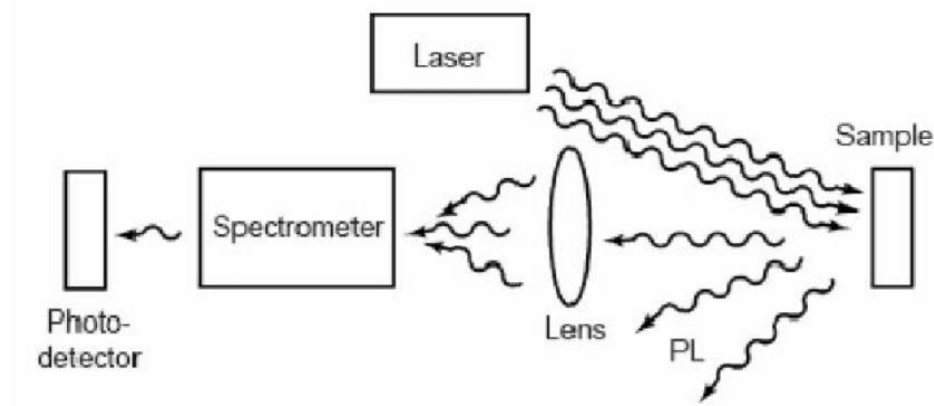


Figure 3.7: A typical PL measurement setup [11].

3.3.7 Raman spectroscopy

The technique of Raman spectroscopy is a method that can be utilized to investigate the chemical structure, phase and polymorphism, crystalline nature, and relations between molecules. This investigation can be carried out in a variety of different ways. It is based on the observation that light has the ability to change the chemical bonds that are already present in a substance. Light from a high-intensity laser source is focused on a molecule, causing the molecule to scatter the light. This is a technique for scattering light, and it works by causing the molecule to scatter the light. Rayleigh, the phenomenon of scatter occurs when the majority of the light that is scattered has the same wavelength (or colour) as the laser source and, as a result, does not provide us with any information that is helpful. This prevents us from drawing any conclusions from the information that is provided by the scattered light. Due to the chemical nature of the analyte, Raman scatter happens when a very little amount of light (usually 0.0000001%), gets scattered at several wavelengths (or colours) [30]. Figure 3.8 below shows a typical Raman principle.

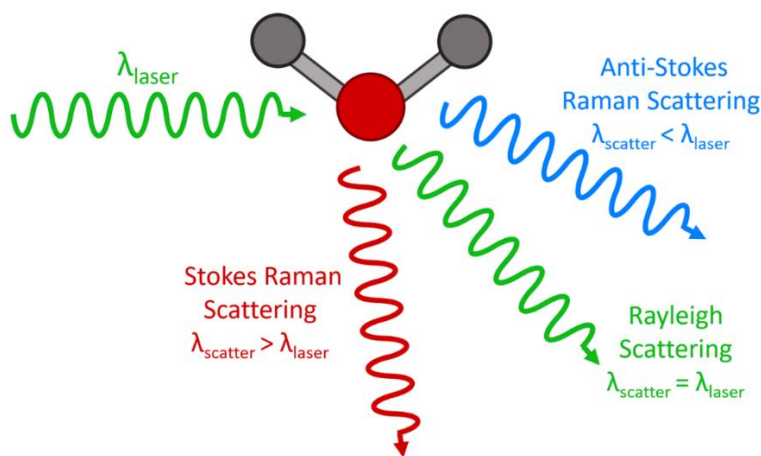


Figure 3.8: A diagrammatic representation of the Raman principle [30].

The position of the peak and the relative peak strength make up the general Raman spectra profile, which possesses a one-of-a-kind chemical imprint that is capable of being utilized to detect and differentiate materials. Because the actual spectrum is often quite complicated, it is possible to look through complete Raman spectral libraries for a match, which helps identify chemicals [30]. A common Raman apparatus involves a laser beam

with a linewidth of less than 1 nm being reflected from a 45° holographic notch filter (HNF), then being focused on the sample by an objective lens after being expanded through a telescope made of two lenses (usually 50 or 100). The same microscope objective is used to gather Raman scatter from the sample, and the same HNF is employed to filter the data. The sample is then moved to the spectrometer, where a liquid nitrogen or thermally cooled CCD camera is used to take a picture of it [31]. The configuration that has been demonstrated brings the illuminating green laser to a point on the sample (slit scanning mode). The cylindrical lens can be taken off to change the line into a spot. A dichroic mirror isolates the red Raman-shifted light from the green laser light and disperses it along a vertical line on the two-dimensional charge-coupled detector (CCD) when a point on the sample is irradiated. This allows the light to be analysed in two dimensions. When using the slit-scanning mode, a large number of spectra are collected all at once. Every single point along the line on the sample generates its own spectrum along the CCD [32]. The operation of a Raman spectrophotometer is depicted in the diagram found in figure 3.9.

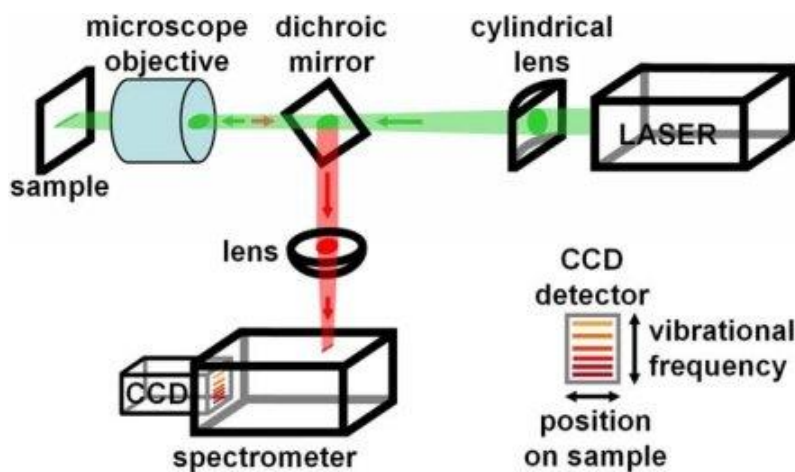


Figure 3.9: Schematic diagram of Raman spectrophotometer [32].

3.3.8 Thermoluminescence spectroscopy

Thermoluminescence (TL) is described as the light that is emitted during the heating of a solid after the substance has first absorbed energy during irradiation. High-energy radiation such as X-rays and gamma rays, as well as ultraviolet, visible, and infrared light, serve as substitute radiation sources. In actuality, the heating just acts as a catalyst to

aid in the release of the absorbed energy, whereas the radiation serves as the energy store. The distribution of electrons in various traps (from shallow traps to deep traps) is affected by the radiation source, the radiation's duration, the time after it ends, and the ambient temperature [33]. TL spectroscopy is a very effective technique used to examine defects in materials, dating, personnel, clinical, environmental, and accidental dose measurements. TL techniques are frequently used to assess the trap depth. It uses TL as a probe to determine which types of radiation are absorbed by crystalline and non-crystalline materials [34]. By carrying out a number of TL experiments with a wide range of excitation temperatures and excitation durations and making use of the initial rise analysis technique, one is able to ascertain both the depth and the shape of the trap distribution. For such a trap depth probe, Smet et al. [33] listed the following steps to be followed:

- (a) Measuring the sample's thermal quenching in order to provide an accurate correction to the TL data.
- (b) Demonstrating the existence of higher-order kinetics by assessing the effect of the dose on the TL glow curves.
- (c) Taking readings of the TL glow curves following excitation at a number of different temperatures (T). Utilizing the first-rise analysis will allow one to determine the overall depth of the trap. The fact that the estimated trap depth fluctuates all the time as a function of T is a strong indication that there is a continuous distribution of the trap depth.
- (d) If the process of trapping is not triggered by heat, the area under the glow curves created in step (c) can be utilized to determine the structure of the continuous trap depth distribution. In the event that the trapping is activated by heat, the areas in question ought to be changed first. Figure 3.10 depicts the experimental setup for measuring TL.

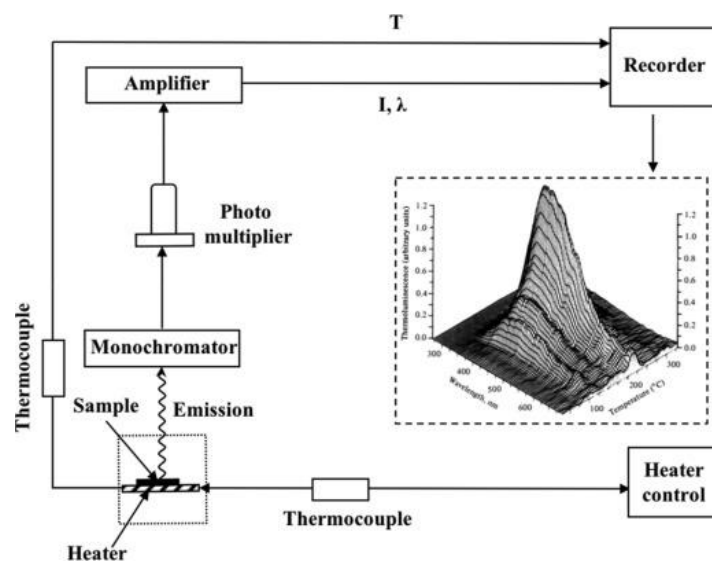


Figure 3.10: Experimental setup for measuring thermoluminescence [33].

References

- [1]. Gao, C., Zheng, P., Liu, Q., Han, S., Li, D., Luo, S., Temple, H., Xing, C., Wang, J., Wei, Y. and Jiang, T., 2021. Recent Advances of Upconversion Nanomaterials in the Biological Field. *Nanomaterials*, 11(10), p.2474.
- [2]. Naplocha, K., 2018. Self-propagating high-temperature synthesis (SHS) of intermetallic matrix composites. In *Intermetallic Matrix Composites* (pp. 203-220). Woodhead Publishing.
- [3]. Stojanovic, B.D., Dzunuzovic, A.S. and Ilic, N.I., 2018. Review of methods for the preparation of magnetic metal oxides. In *Magnetic, Ferroelectric, and Multiferroic Metal Oxides* (pp. 333-359). Elsevier.
- [4]. Bensebaa, F., 2012. *Nanoparticle Technologies: Chapter 5. Clean Energy* (Vol. 19). Elsevier Inc. Chapters.
- [5]. Specchia, S., Galletti, C. and Specchia, V., 2010. Solution combustion synthesis as intriguing technique to quickly produce performing catalysts for specific applications. In *Studies in Surface Science and Catalysis* (Vol. 175, pp. 59-67). Elsevier.
- [6]. Chick, L.A., Pederson, L.R., Maupin, G.D., Bates, J.L., Thomas, L.E. and Exarhos, G.J., 1990. Glycine-nitrate combustion synthesis of oxide ceramic powders. *Materials letters*, 10(1-2), pp.6-12.
- [7]. Tankiewicz, M., Namieśnik, J. and Sawicki, W., 2016. Analytical procedures for quality control of pharmaceuticals in terms of residual solvents content: Challenges and recent developments. *TrAC Trends in Analytical Chemistry*, 80, pp.328-344.
- [8]. Branquinho, R., Santa, A., Carlos, E., Salgueiro, D., Barquinha, P., Martins, R. and Fortunato, E., 2016. Chapter Solution Combustion Synthesis: Applications in Oxide Electronics.
- [9]. Gotoh, T., Jeem, M., Zhang, L., Okinaka, N. and Watanabe, S., 2020. Synthesis of yellow persistent phosphor garnet by mixed fuel solution combustion synthesis and its characteristics. *Journal of Physics and Chemistry of Solids*, 142, p.109436.

- [10]. <https://www.jove.com/science-education/10446/x-ray-diffraction> [Accessed October 2021]
- [11]. Mbule, P.S., 2009. *Sol-gel synthesis of and luminescent properties of Pr^{3+} in different host matrices* (Masters dissertation, University of the Free State).
- [12]. Mbule, P.S., 2013. *The effects of the ZnO nanoparticles buffer layer on organic solar cells* (Doctoral dissertation, University of the Free State).
- [13]. Zhang, F., 2015. *Photon upconversion nanomaterials* (Vol. 416). Berlin, Germany: Springer.
- [14]. Bunaciu, A.A., 2015. Udriștioiu, E. g.; Aboul-Enein, HY. *Critical Reviews in Analytical Chemistry*, 45, pp.289-299.
- [15]. Pinto, A.M., Oliveira, V.S. and Falcao, D.S.C., 2018. *Direct Alcohol Fuel Cells for Portable Applications: Fundamentals, Engineering and Advances*. Academic Press.
- [16]. Sun, D., Siddiqui, M.O.R. and Iqbal, K., 2019. Specialty testing techniques for smart textiles. In *Smart Textile Coatings and Laminates* (pp. 99-116). Woodhead Publishing.
- [17]. Sricharoenchaikul, V. and Atong, D., 2009. Thermal decomposition study on *Jatropha curcas* L. waste using TGA and fixed bed reactor. *Journal of analytical and applied Pyrolysis*, 85(1-2), pp.155-162.
- [18]. Moseson, D.E., Jordan, M.A., Shah, D.D., Corum, I.D., Alvarenga Jr, B.R. and Taylor, L.S., 2020. Application and limitations of thermogravimetric analysis to delineate the hot melt extrusion chemical stability processing window. *International Journal of Pharmaceutics*, 590, p.119916.
- [19]. Buckley, L.L., 1995. Data quality objective to support resolution of the organic fuel rich tank safety issue (No. WHC-SD-WM-DQO-006-Rev. 1). Westinghouse Hanford Co., Richland, WA (United States).
- [20]. Sindhu, R., Binod, P. and Pandey, A., 2015. Microbial Poly-3-Hydroxybutyrate and Related Copolymers. In *Industrial Biorefineries & White Biotechnology* (pp. 575-605). Elsevier.

- [21]. Titus, D., Samuel, E.J.J. and Roopan, S.M., 2019. Nanoparticle characterization techniques. In *Green synthesis, characterization and applications of nanoparticles* (pp. 303-319). Elsevier.
- [22]. Mirabella, F.M. ed., 1998. *Modern techniques in applied molecular spectroscopy* (Vol. 14). John Wiley & Sons.
- [23]. Hunault, M., Lelong, G., Gauthier, M., Gélébart, F., Ismael, S., Galois, L., Bauchau, F., Loisel, C. and Calas, G., 2016. Assessment of transition element speciation in glasses using a portable transmission ultraviolet–visible–near-infrared (UV-Vis-NIR) spectrometer. *Applied spectroscopy*, 70(5), pp.778-784.
- [24]. Passos, M.L. and Saraiva, M.L.M., 2019. Detection in UV-visible spectrophotometry: Detectors, detection systems, and detection strategies. *Measurement*, 135, pp.896-904.
- [25]. Jentoft, F.C., 2009. Ultraviolet–visible–near infrared spectroscopy in catalysis: theory, experiment, analysis, and application under reaction conditions. *Advances in catalysis*, 52, pp.129-211.
- [26]. Hiltunen, A., 2020. Photovoltaic Applications of Porous Atomic Layer Deposited Metal Oxides from Cellulose Templates.
- [27]. Mendelsberg, R.J., 2009. Photoluminescence of ZnO grown by eclipse pulsed laser deposition.
- [28]. Peter, E., Subash, T.D., Subha, T.D. and Nazim, A., 2020. Utilizing Radiant Nanoparticles in Silicon for Balanced White Color Adapters. *Silicon*, pp.1-7.
- [29]. Acharya, S., Padhi, D.K. and Parida, K.M., 2020. Visible light driven LaFeO₃ nanosphere/RGO composite photocatalysts for efficient water decomposition reaction. *Catalysis Today*, 353, pp.220-231.
- [30]. Xu, Z., He, Z., Song, Y., Fu, X., Rommel, M., Luo, X., Hartmaier, A., Zhang, J. and Fang, F., 2018. Topic review: application of Raman spectroscopy characterization in micro/nanomachining. *Micromachines*, 9(7), p.361.

- [31]. Adya, A.K. and Canetta, E., 2020. Nanotechnology and its applications to animal biotechnology. In *Animal Biotechnology* (pp. 309-326). Academic Press.
- [32]. Downes, A. and Elfick, A., 2010. Raman spectroscopy and related techniques in biomedicine. *Sensors*, 10(3), pp.1871-1889.
- [33]. Qiu, J., Li, Y. and Jia, Y., 2020. *Persistent Phosphors: From Fundamentals to Applications*. Woodhead Publishing.
- [34]. Singh, M., Thermoluminescence Spectroscopy: A Powerful Tool.

CHAPTER 4

Effects of doping concentration and annealing temperature on the structure of the solution combustion synthesized NaYF₄ co-doped Yb³⁺-Er³⁺ and NaGdF₄ co-doped Yb³⁺-Nd³⁺ nanocrystals.

This chapter discusses the structure, elemental properties, morphology, and thermal stability of nanocrystals prepared by combusting NaYF₄, NaGdF₄, Yb³⁺-Er³⁺ co-doped NaYF₄, and Yb³⁺-Nd³⁺ co-doped NaGdF₄. The structures of the nanocrystals were studied to see how the amount of dopant and the temperature of annealing affected them.

4.1 INTRODUCTION

UC nanocrystals and their synthesis have, in recent times, garnered a significant amount of attention due to the variety of applications that may be possible with them in biolabeling, solar device sub-band gap energy adjustment, and security printing, with a special emphasis on RE-doped UC nanocrystals. The extremely high UC efficiencies, the capability to change colour purity by adjusting doping concentrations, and the peculiar phenomena brought on by surface effects in nanoscale UC nanocrystals have recently been the subject of a few fundamental studies [1–4]. These studies aim to explain the causes of these characteristics. RE³⁺ ions that have undergone an UC can be incorporated into host materials such as "halides (including iodides, bromides, and chlorides), oxides, oxysulfides, fluorides, vanadates, and phosphates" [5–8]. To achieve the highest possible level of stability in both air and water, the host matrices must not be hygroscopic [9]. In addition to this, they should have "low phonon frequencies" to cut down on losses caused by relaxation paths that do not utilize radiation [10]. Halides such as "iodides, bromides, and chlorides absorb water, and despite the fact that their phonon frequencies are relatively low (300 cm⁻¹), they have very few applications. The host matrix of the oxides possesses phonon frequencies that are greater than 500 cm⁻¹ and is

chemically stable. Additionally, the host matrix has a high number of phonons. Fluorides, in contrast to other host matrices, have good chemical stability, a low phonon frequency (between 300 and 500 cm^{-1}), and are easy to disperse in a colloidal state when combined with water and a number of "nonpolar solvents, such as hexane, ethanol, chloroform, toluene, and dimethyl sulfoxide" [11]. As a consequence of this, fluoride hosts, particularly alkaline RE tetrafluoride (AREF_4), are the hosts that are utilized most frequently for UC emission [6–8]. These materials are suitable for use in integrated optical devices, including solar cells, low-cost NIR diodes, and planar optical amplifiers, because they can combine two or more low-energy photons to produce detectable higher-energy photons. Materials with a low rate of electron-hole recombination are thought to make the greatest hosts for RE^{3+} ions to increase UCL because they can minimize multi-phonon non-radiative relaxation [5].

The majority of lanthanide ions are capable of undergoing UC from NIR to visible light; regrettably, when pump concentrations are low, only a few trivalent lanthanide ions (like Er^{3+} and Tm^{3+}) can undergo extremely effective UC (980 nm excitation) [12]. The most frequently studied UC nanocrystals to date are $\text{Yb}^{3+}\text{-Er}^{3+}$ or $\text{Yb}^{3+}\text{-Tm}^{3+}$ co-doped NaYF_4 nanocrystals [15–16]. These nanocrystals are also widely acknowledged as possessing the highest levels of luminescence of all fluorescent materials [14], making them the best candidates for use in PV cells. $\text{NaYF}_4\text{:Yb}^{3+},\text{Er}^{3+}$ nanocrystals are mostly utilized in solar cells as photon absorption enhancers, and NaYF_4 in the nanoscale size range is well-known as a very effective host matrix for green and blue UC [5, 13]. "Due to its strong photochemical stability, low phonon energy (350 cm^{-1}), high levels of transparency in the UV, visible, and NIR ranges, and ability to control energy transfers between the Ln^{3+} ions, NaGdF_4 makes a great host material for achieving the UC and down-shifting luminescence of Ln^{3+} dopants" [15]. At room temperature, NaYF_4 and NaGdF_4 nanocrystals exist in two polymorphs, namely, hexagonal and cubic, which are excellent luminous host matrices for the UC-process [5, 16]. Kim et al. [16] reported that fluoride compounds, such as $\text{NaYF}_4/\text{NaGdF}_4\text{:Er}^{3+},\text{Yb}^{3+}$, are especially effective materials that emit green radiation after being excited by IR light. In the NaYF_4 and NaGdF_4 hosts, the RE dopant ions (Er^{3+} , Ho^{3+} , or Yb^{3+}) substitute Y^{3+} [6].

NaYF₄:Yb³⁺,Er³⁺ and NaGdF₄:Yb³⁺,Nd³⁺ UC nanocrystals can be synthesized using a variety of techniques, including co-precipitation, hydrothermal, solvothermal processing, thermal decomposition, sol-gel, combustion, and flame synthesis [17-18]. However, the majority of these synthesis techniques demand a number of difficult steps, expensive equipment, and specific experimental conditions. The advantage of combustion synthesis over alternative processes is the affordability with which NaYF₄:Yb³⁺,Er³⁺ nanocrystals may be produced since the process does not need expensive equipments. Additionally, the combustion synthesis method enables the production of homogeneous, crystalline, multi-component, fine powders with shorter processing times and lower temperatures (i.e., a few minutes or even seconds). On the other hand, the high reaction rate typically causes the products' crystallinity to decrease and adds enduring by-products that impair brightness. It is often necessary to perform an appropriate post-treatment to eliminate these occurrences without resulting in excessive crystal growth [19]. In 2016, Roh et al. [20] successfully synthesized the NaYF₄:Yb³⁺,Er³⁺ via a hydrothermal method and then added them as a mesoporous layer capable of upconverting to CH₃NH₃PbI₃ PSCs). The PCE of the PSCs based on the layer of upconverting mesoporous material was 16.0%. This represents an improvement of 13.7% over the efficiency of conventional TiO₂-nanocrystal-based PSCs [19]. The NIR sunlight-collecting ability of the PSCs was 14.1%. This demonstrates how hexagonal NaYF₄:Yb³⁺,Er³⁺ nanoprisms boost photocurrent by extending the PSC's absorption range via UPL. The core-shell NaYF₄:Yb³⁺,Er³⁺/NaYF₄ nanocrystals were prepared in 2018 by Huang et al. [21] using the thermal decomposition technique. The produced nanoparticles demonstrated an improvement in the UCL after being excited at 980 nm due to the superior surface defect reduction and spatial separation of doped ions that the nanoparticles possessed.

The UCNCs include an activator, a sensitizer, and a matrix substance in their construction. The activator serves in this capacity as the light centre. Sensitizers are utilized to absorb energy before transferring that energy onto activator ions. The matrix material, in general, does not contribute to the transmission of energy; rather, it serves as a fixed dopant ion and provides the appropriate crystal field for the luminous centre [22–23]. The UC process is dependent on a number of various processes, some of which are "(i) the absorption of the excitation energy by the sensitizer, (ii) the transfer of energy from

the sensitizer to the activator, (iii) the excited activator's radiative transitions, and (iv) the luminescence quenching" [19, 24–26]. For instance, in β -NaGdF₄:Yb³⁺, Ln³⁺ (where Ln = Er³⁺, Tm³⁺, or Ho³⁺), Ln³⁺ performs the role of the activator, Yb³⁺ fulfils the function of the sensitizer, and β -NaGdF₄ fulfils the function of the matrix material [9]. Yb³⁺ is known to be an outstanding sensitizer (energy donor) with two distinct ground and excited states that are separated by 980 nm and correspond to the states ²F_{7/2} and ²F_{5/2}, respectively. Typically, NIR laser is used to excite Yb³⁺, and energy is then transferred to an activator (energy acceptor), improving visible or NIR emission [17].

In this study, we look at how the UC properties of NaYF₄ and NaGdF₄ nanocrystals change when the concentrations of Yb³⁺-Er³⁺ and Yb³⁺-Nd³⁺ and the annealing temperatures are changed. Different techniques have been used to study the structure, shape, molecular functional groups, and elements.

4.2 RESULTS AND DISCUSSION

4.2.1 XRD studies

Figure 4.1(a-c) displays the XRD patterns of the as-prepared and annealed NaYF₄ and NaYF₄:Yb³⁺,Er³⁺ nanocrystals. Er³⁺ was held constant while varying Yb³⁺ and also Yb³⁺ held constant while varying Er³⁺. For the as-prepared nanocrystals in Figure 4.1(a) and annealed at 600 °C samples Figure 4.1(b), the diffraction peaks were observed at angles (2 θ) of 17.19°, 28.56°, 30.79°, 34.73°, 40.17°, 43.59°, 47.50°, 52.99°, 53.83°, 55.09°, 61.14°, 62.11°, 65.05°, 69.84°, 70.96°, and 77.56° corresponding to the reflection of (100), (110), (101), (200), (111), (201), (210), (002), (300), (211), (102), (112), (220), (202), (311), (212), and (302) crystal planes, respectively. The diffraction peaks mentioned above matched the standard JCPDS data with card number 00-064-0156 quite well. The as-prepared and the samples annealed at 600 °C were confirmed to exhibit the hexagonal β -NaYF₄ phase. On the other hand, NaYF₄:Yb³⁺,Er³⁺ nanocrystals annealed at 700 °C in Figure 4.1(c), shows the diffraction peaks observed at angles (2 θ) of 28.62°, 29.76°, 30.57°, 33.00°, 38.64°, 43.15°, 47.76°, 53.41°, 56.41°, 59.28°, 69.55°, and 76.82° corresponding to the reflection of (111), (110), (101), (200), (111), (201), (220), (300), (311), (222), and (400), and (302) crystal planes, respectively, matching well with the

standard JCPDS data, card number 00-006-0342. These samples confirmed the formation of the α -cubic of the nanocrystals. Diffraction peaks (100), (210), (002), (211), (102), (202), (212), and (112) vanished after the samples were annealed at 700 °C. This may be because material has recrystallized at high annealing temperatures, resulting in a significant grain growth, which could account for the disappearance.

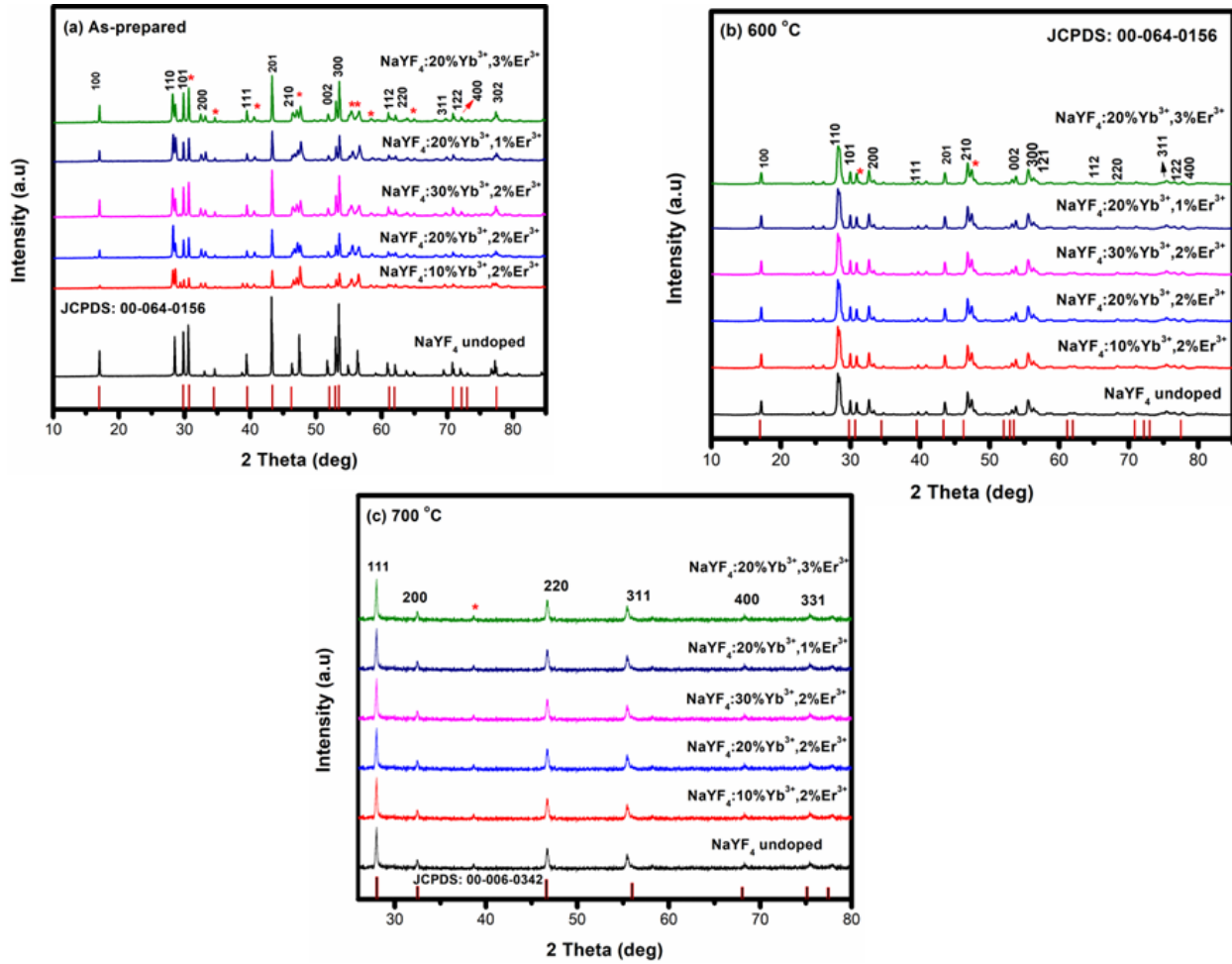


Figure 4.1. XRD patterns of Yb³⁺-Er³⁺ co-doped NaYF₄ nanocrystals (a) as-prepared, (b) annealed at 600 °C, and (c) annealed at 700 °C.

Figure 4.2(a-c) displays the XRD patterns of the as-prepared and annealed NaGdF₄ and NaGdF₄:Yb³⁺,Nd³⁺ nanocrystals. Nd³⁺ was held constant while varying Yb³⁺ and also Yb³⁺ held constant while varying Nd³⁺.

The diffraction peaks for the as-prepared samples were observed at angles (2 θ) of 17.01°, 27.73°, 30.15°, 36.15°, 42.94°, 46.76°, 48.14°, and 52.87° corresponding to the reflection

of (100), (110), (101), (200), (201), (210), (022), and (211) crystal planes, respectively. The diffraction peaks for all the samples annealed at 600 °C and 700 °C were observed at angles (2θ) of 17.01°, 27.73°, 30.15°, 36.15°, 39.36°, 42.94°, 46.76°, 48.14°, 52.87°, 59.55°, and 61.52° corresponding to the reflection of (100), (110), (101), (200), (111), (201), (210), (022), (211), and (220) crystal planes, respectively. All samples verified the formation of the β -hexagonal phases of the nanocrystals. The as-prepared samples data matched with the data of the standard JCPDS card number 01-082-4236, while the annealed samples data matched with the data of the standard JCPDS card number 00-027-0699. The impurity peaks were observed in the as-prepared sample (marked with*). Those peaks are due to the short reaction time [27]. Upon annealing the nanocrystals at 600 °C and 700 °C, an additional diffraction peak was observed in comparison to the as-prepared nanocrystals and the diffraction peak at an angle (2θ) of 52.87° disappeared. The disappearing and adding of the diffraction peaks observed when the nanocrystals were annealed may be because the material have recrystallized at high annealing temperatures, resulting in a significant grain growth, which could account for the disappearance and addition of the diffraction peaks. Some of these grains accumulate in one direction (preferred orientation) as a result of recrystallization due to annealing. This suggests that the substance's crystalline structure has changed. Either the phase dissolves in a multiphase mixture or it has lost its crystal structure and turned amorphous [27].

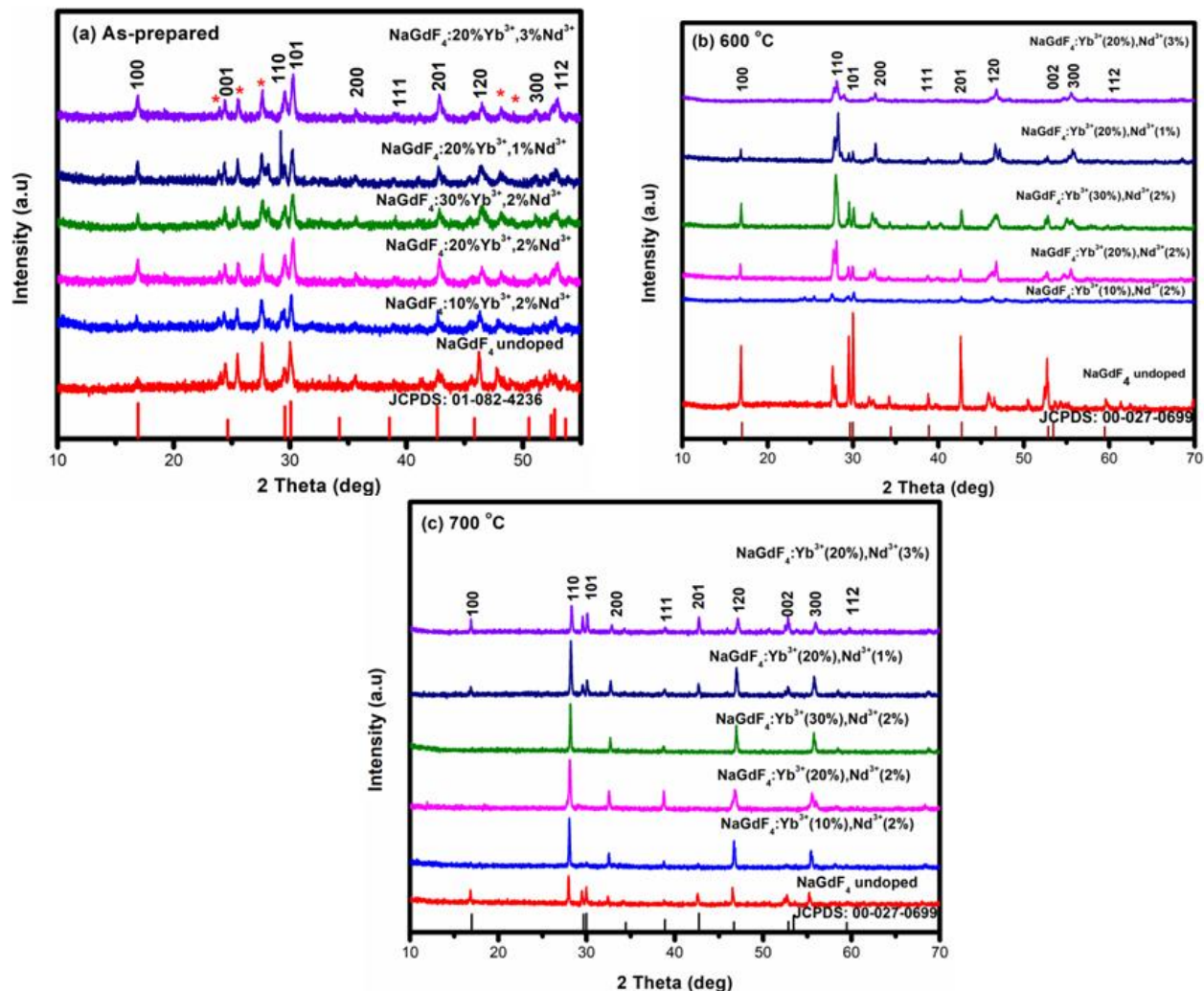


Figure 4.2. XRD patterns of (a) the as-prepared, (b) annealed at 600 °C, and (c) annealed at 700 °C NaGdF₄ and Yb³⁺-Nd³⁺ co-doped NaGdF₄ nanocrystals.

The peaks of the diffraction pattern become more prominent, broaden, and shift as the NaYF₄ and NaGdF₄ hosts are doped. Since dopant atoms swap out a few of the atoms that make up the host when introduced into the host structure, the structure compresses or expands [28]. The size of the dopant influences the peak shift in the XRD diffraction peaks (see figure 4.3 (a), (c) and figure 4.4 (a-c)). If the dopant is smaller than the base metal, it takes up an interstitial position, shifting the lattice structure and decreasing the d-spacing between the atoms [29]. Figures 4.3 and 4.4 demonstrate the diffraction peak

shift to either lower or higher diffraction angles for as-prepared and annealed NaYF₄ and NaGdF₄ nanocrystals upon doping.

When the peak shifts to greater angles, the host structure contracts, and vice versa. Furthermore, the shift in diffraction peaks represents an increase or decrease in lattice parameters, owing mostly to the variations in ionic radii between the principal elements and the dopant ions, showing that the dopant ions have been absorbed into the host lattice in a successful manner [29-30]. If the particles are nanoscale in size, the diffraction peak will be exceedingly diffuse and broad because the structure of the particles will be considerably reflected in their highly disordered surface structure [31].

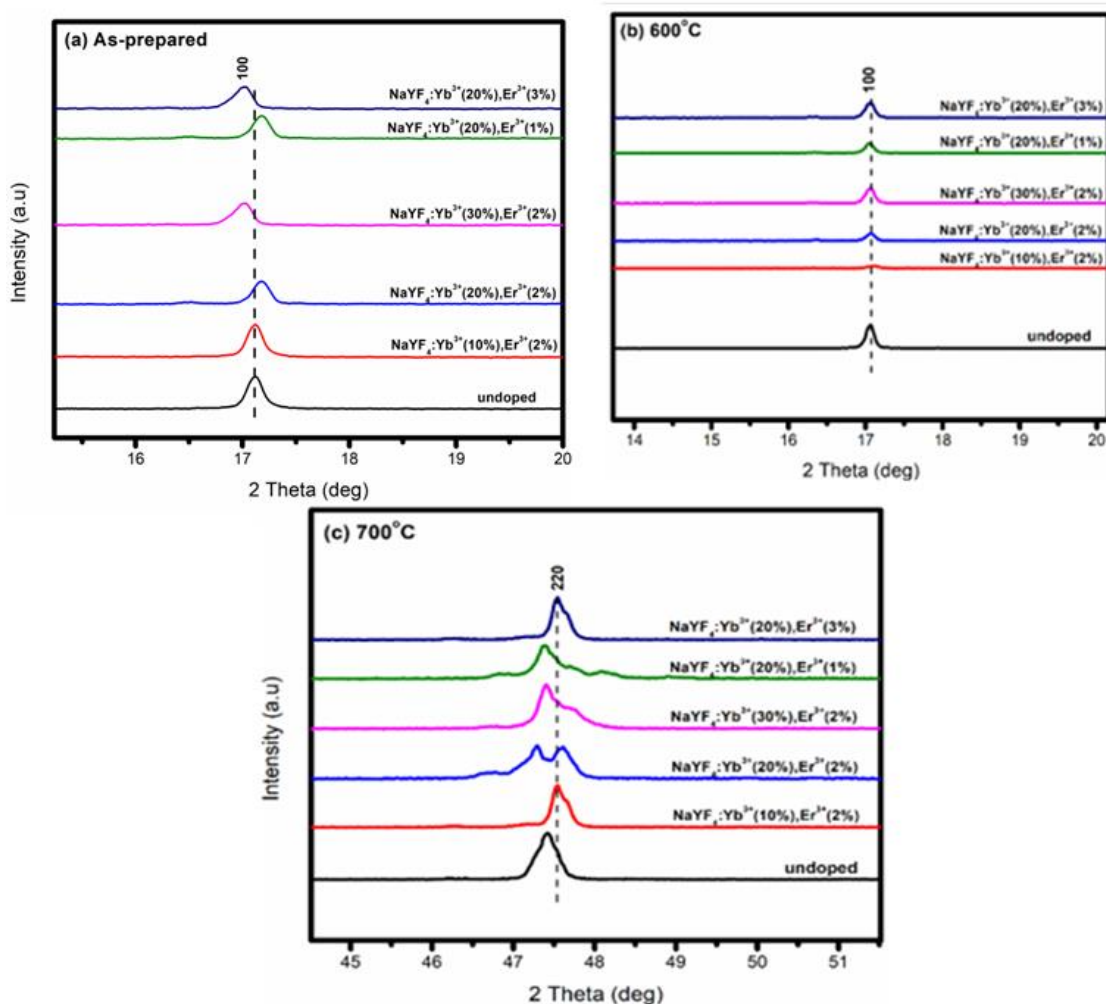


Figure 4.3: Diffraction peak shift analysis of Yb³⁺-Er³⁺ co-doped NaYF₄ nanocrystals.

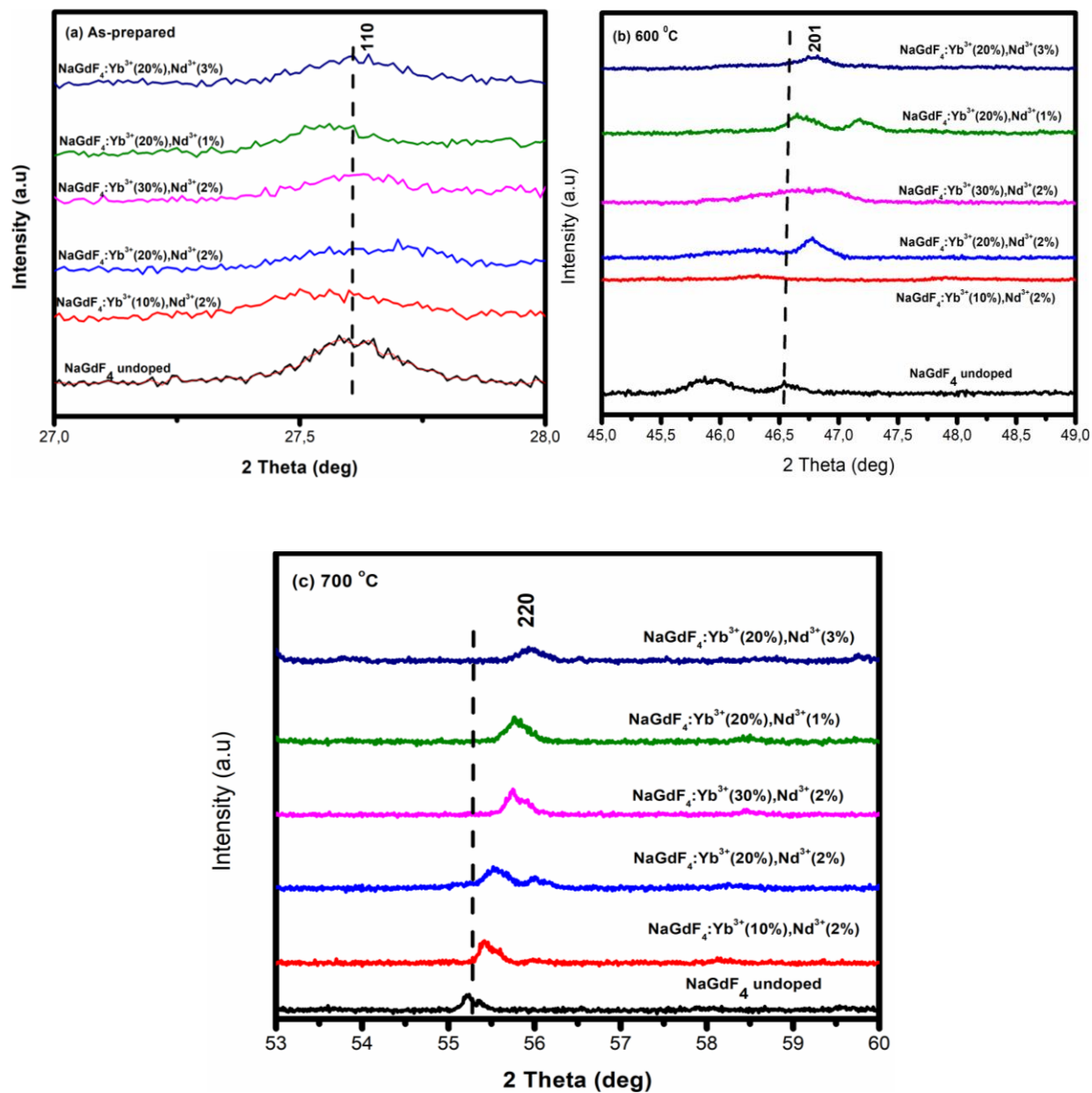


Figure 4.4: Diffraction peak shift analysis of Yb^{3+} - Nd^{3+} co-doped NaGdF_4 nanocrystals.

4.2.2 Crystallite size, lattice parameters and strain analysis.

The Debye-Scherrer equation (1) [31] was employed to compute the crystallite size of the samples, which uses the width of the peak at half of its greatest height (FWHM) of wide-angle X-ray scattering.

$$D = \frac{0.9 \lambda}{\beta \cos \theta} \quad (4.1)$$

where λ is the X-ray source's wavelength, β is the full-width at half maximum in radians, and θ is the angle of Bragg's diffraction.

The crystallite size, FWHM, lattice strain, and lattice parameters of the diffraction peaks for the as-prepared and annealed samples were determined for both NaYF₄ and NaGdF₄ nanocrystals. Varying the dopant concentrations and annealing temperatures, respectively either increased or decreased the crystallite sizes of the nanocrystals. The increase in the crystallite sizes may be due to the enhanced incorporation of Yb³⁺ ions into the Y³⁺ and Gd³⁺ sites of the NaYF₄ and NaGdF₄ host lattices. The decrease in crystallite size indicates a reduction in the crystalline quality of the NaYF₄ with Yb³⁺-Er³⁺ and the NaGdF₄ with Yb³⁺-Nd³⁺ doping (indicated in table 4.1 and 4.2). This indicates that changing dopant concentrations and annealing temperatures, respectively have a huge effect in the crystallite sizes of the nanocrystals [32–33]. The lattice strains of the nanocrystals were estimated using equation (2) [31]:

$$\varepsilon = \frac{\beta}{4 \tan \theta} \quad (4.2)$$

ε - the lattice strain and β - the full width at half maximum. The lattice parameters for the cubic structures were determined using the equation (3) [35]:

$$\frac{1}{d_{hkl}^2} = \frac{h^2}{a^2} + \frac{k^2}{b^2} + \frac{l^2}{c^2} \quad (4.3)$$

and for the hexagonal structures, the lattice parameters were determined using the equation (4) [34]:

$$\frac{1}{d_{hkl}} = \frac{4}{3} \left(\frac{h^2 + hk + k^2}{a^2} \right) + \frac{l^2}{c^2} \quad (4.4)$$

Where the interplanar spacing (d) was determined from the equation (5) [28]:

$$2d_{hkl} \sin\theta = n\lambda_{CuK\alpha} \quad (4.5)$$

The estimated crystallite sizes of the nanocrystals, lattice strains, and lattice parameters are shown in Tables 4.1 and 4.2, and the relationships between the dopant concentrations and crystallite size, as well as lattice strains indicating that high level of doping concentration increases the lattice strain and high annealing temperatures reduces the lattice strain, are shown in Figures 4.5 and 4.6.

Table 4.1: Crystallite size, strain and lattice parameters at for Yb³⁺-Er³⁺ co-doped NaYF₄ nanocrystals.

Sample name	2 θ (°)	Crystallite size (nm)	Lattice strain (x10 ⁻³)	Lattice parameters a=b (Å)	Lattice parameters c (Å)
As-prepared samples					
NaYF ₄ undoped	17.19	5.58	0.21	2.62	5.24
NaYF ₄ :Yb ³⁺ (10%),Er ³⁺ (2%)	17.19	7.25	0.16	2.62	5.24
NaYF ₄ :Yb ³⁺ (20%),Er ³⁺ (2%)	17.19	6.05	0.19	2.62	5.24
NaYF ₄ :Yb ³⁺ (30%),Er ³⁺ (2%)	17.19	5.18	0.23	2.62	5.24
NaYF ₄ :Yb ³⁺ (20%),Er ³⁺ (1%)	17.19	6.30	0.19	2.62	5.24
NaYF ₄ :Yb ³⁺ (20%),Er ³⁺ (3%)	17.19	5.18	0.22	2.62	5.24
Annealed at 600 °C samples					
NaYF ₄ undoped	17.19	4.84	0.24	2.62	5.24
NaYF ₄ :Yb ³⁺ (10%),Er ³⁺ (2%)	17.19	6.59	0.18	2.62	5.24
NaYF ₄ :Yb ³⁺ (20%),Er ³⁺ (2%)	17.19	5.80	0.20	2.62	5.24
NaYF ₄ :Yb ³⁺ (30%),Er ³⁺ (2%)	17.19	4.83	0.24	2.62	5.24
NaYF ₄ :Yb ³⁺ (20%),Er ³⁺ (1%)	17.19	5.37	0.22	2.62	5.24
NaYF ₄ :Yb ³⁺ (20%),Er ³⁺ (3%)	17.19	5.00	0.23	2.62	5.24
Annealed at 700 °C samples					
NaYF ₄ undoped	47.76	3.75	0.12	3.53	3.53
NaYF ₄ :Yb ³⁺ (10%),Er ³⁺ (2%)	47.76	5.15	0.09	3.53	3.53
NaYF ₄ :Yb ³⁺ (20%),Er ³⁺ (2%)	47.76	5.28	0.09	3.53	3.53
NaYF ₄ :Yb ³⁺ (30%),Er ³⁺ (2%)	47.76	5.03	0.09	3.53	3.53
NaYF ₄ :Yb ³⁺ (20%),Er ³⁺ (1%)	47.76	4.79	0.10	3.53	3.53
NaYF ₄ :Yb ³⁺ (20%),Er ³⁺ (3%)	47.76	5.03	0.10	3.53	3.53

Table 4.2: Crystallite size, strain and lattice parameters at for Yb³⁺-Nd³⁺ co-doped NaGdF₄ nanocrystals.

Sample name	2 θ (°)	Crystallite size (nm)	Lattice strain ($\times 10^{-3}$)	Lattice parameters a=b (Å)	Lattice parameters c (Å)
As-prepared samples					
NaGdF ₄ undoped	27.73	1.13	0.94	2.63	0.69
NaGdF ₄ :Yb ³⁺ (10%),Nd ³⁺ (2%)	27.73	1.24	1.29	2.63	0.69
NaGdF ₄ :Yb ³⁺ (20%),Nd ³⁺ (2%)	27.73	0.88	1.41	2.63	0.69
NaGdF ₄ :Yb ³⁺ (30%),Nd ³⁺ (2%)	27.73	0.78	1.40	2.63	0.69
NaGdF ₄ :Yb ³⁺ (20%),Nd ³⁺ (1%)	27.73	0.96	0.95	2.63	0.69
NaGdF ₄ :Yb ³⁺ (20%),Nd ³⁺ (3%)	27.73	1.55	0.70	2.63	0.69
Annealed at 600 °C samples					
NaGdF ₄ undoped	42.71	1.81	0.52	2.28	2.28
NaGdF ₄ :Yb ³⁺ (10%),Nd ³⁺ (2%)	42.71	2.16	0.52	2.28	2.28
NaGdF ₄ :Yb ³⁺ (20%),Nd ³⁺ (2%)	42.71	2.57	0.37	2.28	2.28
NaGdF ₄ :Yb ³⁺ (30%),Nd ³⁺ (2%)	42.71	2.10	0.44	2.28	2.28
NaGdF ₄ :Yb ³⁺ (20%),Nd ³⁺ (1%)	42.71	1.81	0.52	2.28	2.28
NaGdF ₄ :Yb ³⁺ (20%),Nd ³⁺ (3%)	42.71	0	0	2.28	2.28
Annealed at 700 °C samples					
NaGdF ₄ undoped	55.28	1.52	0.39	2.28	2.28
NaGdF ₄ :Yb ³⁺ (10%),Nd ³⁺ (2%)	55.28	1.50	0.49	2.28	2.28
NaGdF ₄ :Yb ³⁺ (20%),Nd ³⁺ (2%)	55.28	1.04	0.83	2.28	2.28
NaGdF ₄ :Yb ³⁺ (30%),Nd ³⁺ (2%)	55.28	1.68	0.39	2.28	2.28
NaGdF ₄ :Yb ³⁺ (20%),Nd ³⁺ (1%)	55.28	1.93	0.44	2.28	2.28
NaGdF ₄ :Yb ³⁺ (20%),Nd ³⁺ (3%)	55.28	2.23	0.49	2.28	2.28

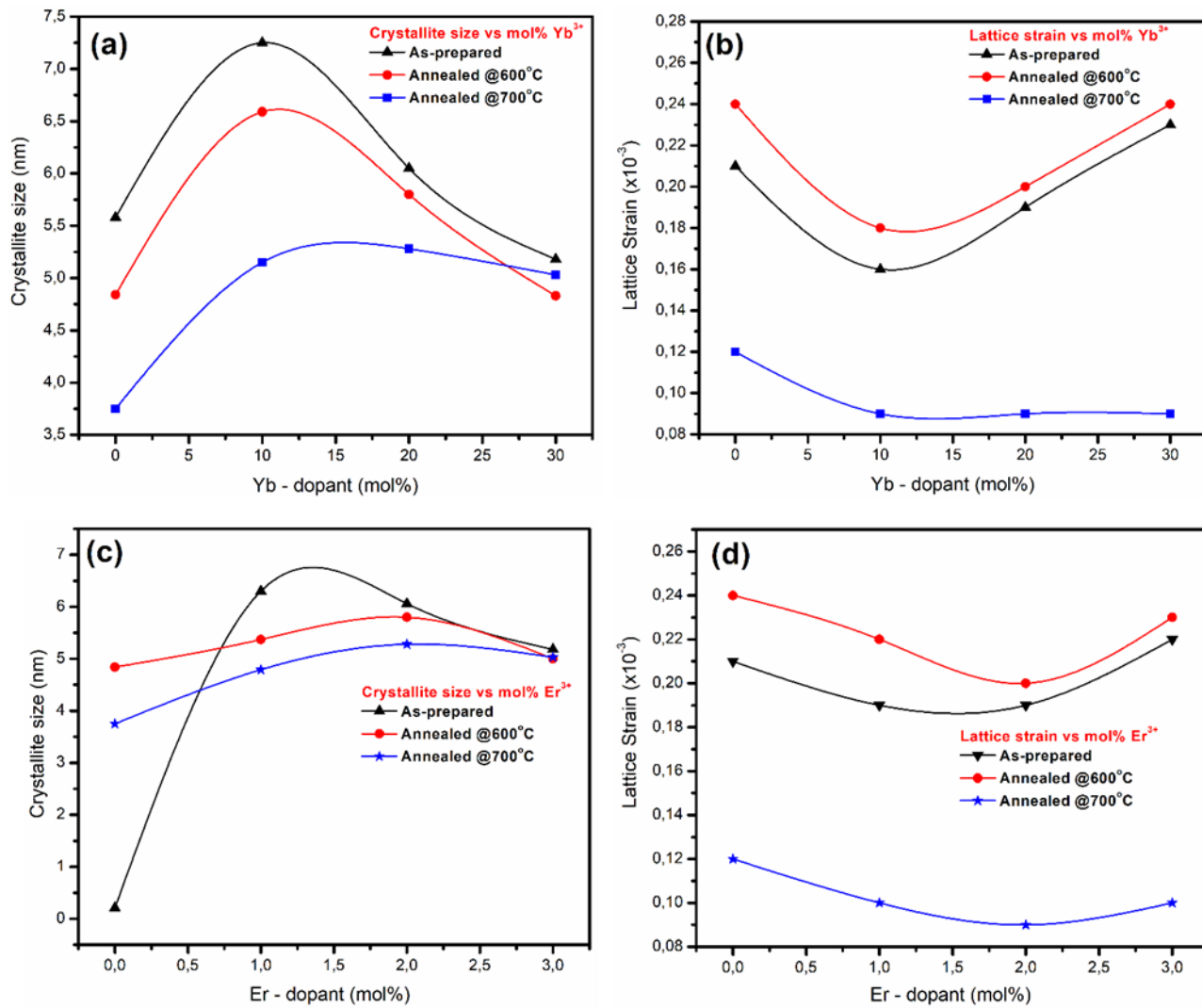


Figure 4.5: Relation between the (a,c) crystallite size and (b,d) lattice strain versus the Yb – Er dopant concentrations.

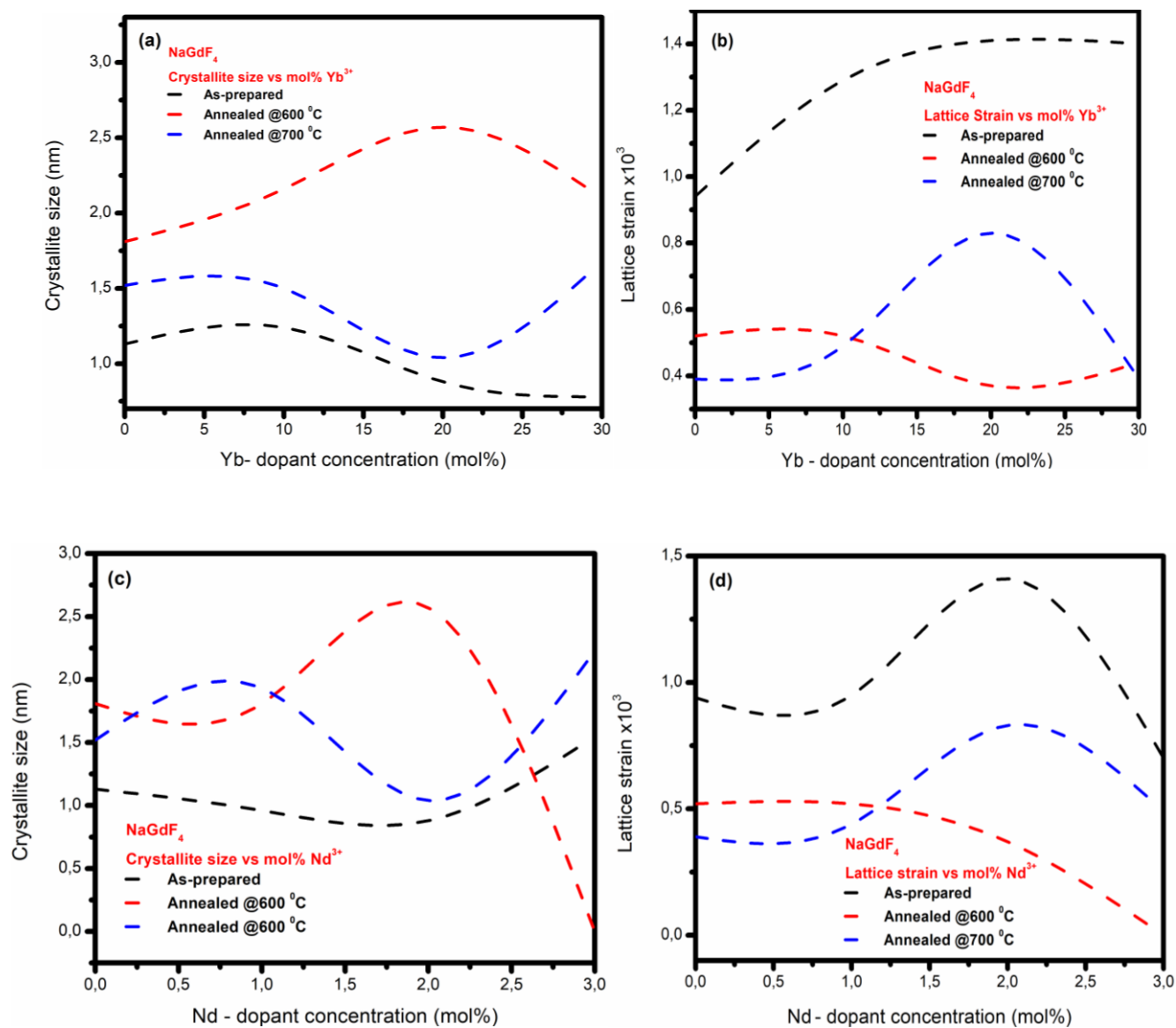


Figure 4.6: Relation between the (a,c) crystallite size and (b,d) lattice strain versus the Yb – Nd dopant concentrations.

4.2.2 FE-SEM and EDS and elemental mapping analysis

Figures 4.7–4.12 show FE-SEM images of the as-prepared and annealed undoped and Yb^{3+} - Er^{3+} and Yb^{3+} - Nd^{3+} doped NaYF_4 and NaGdF_4 , respectively. In Figures 4.7–4.9, the concentration of Er^{3+} ions were held constant at 2 mol% while the concentration of Yb^{3+} ions was changed from 10 to 30 mol%. Again, the concentration of Yb^{3+} ions was kept constant at 20 mol% while that of Er^{3+} ions was changed from 1 to 3 mol% when doping the NaYF_4 host.

In the process of varying the dopants' concentrations, the samples exhibited a dramatic difference in morphologies. Figure 4.7(a) displays the undoped NaYF_4 , showing spherical-like nanocrystals, whereas Figures 4.7(b) and (c) show that increasing the Yb^{3+} ion dopant concentration leads to a combination of spherical-like and growing rod-like morphologies. Figure 4.7(d) shows a mixture of rods and cubic structures at the highest doping concentration of Yb^{3+} (30 mol%). When the Er^{3+} ion concentrations were increased from 1 to 3 mol% (as shown in Figure 4.7(c-f)), the morphology changed to an irregular shape, then to rods, and finally to spherical at the highest Er^{3+} ion concentration (3 mol%).

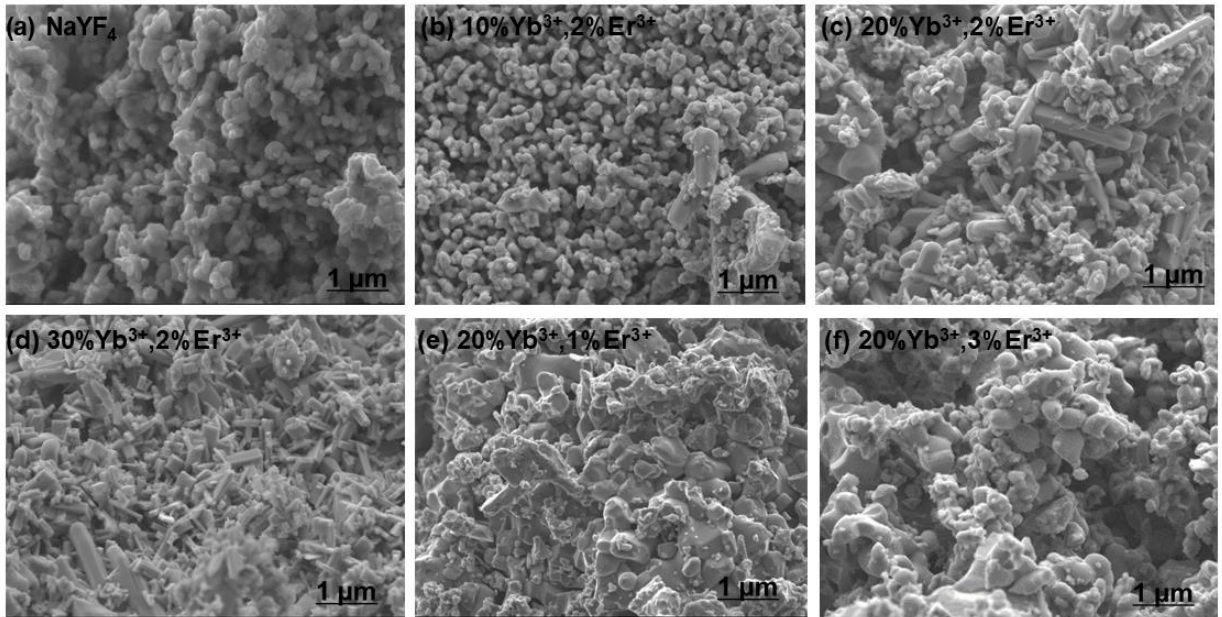


Figure 4.7: FE-SEM images of the undoped and Yb^{3+} – Er^{3+} co-doped NaYF_4 nanocrystals, before annealing.

Upon annealing the samples at 600 °C, as shown in Figure 4.8(a-f), the undoped NaYF₄ nanocrystals displayed a highly agglomerated rod-like morphology (see Figure 4.8(a)). Thereafter, the formation of hexagonally shaped morphology was observed for NaYF₄:10%Yb³⁺,2%Er³⁺ and NaYF₄:20%Yb³⁺,2%Er³⁺ as it appears in Figure 4.8(b-c), with NaYF₄:30%Yb³⁺,2%Er³⁺ showing clearer cubic structured morphology in Figure 4.8(d). Again, when changing the Er³⁺ ion concentration from 1 to 3 mol% (depicted in Figure 4.8(c-f)), the morphology evolved to irregular particle shape with combinations of spherical, and traces of hexagonal shapes at the Er³⁺ concentration of 3 mol%. As the dopant changes and the annealing temperature increases, the structure and morphology changes. High level of doping decreases the particle sizes. This confirms what was observed in XRD.

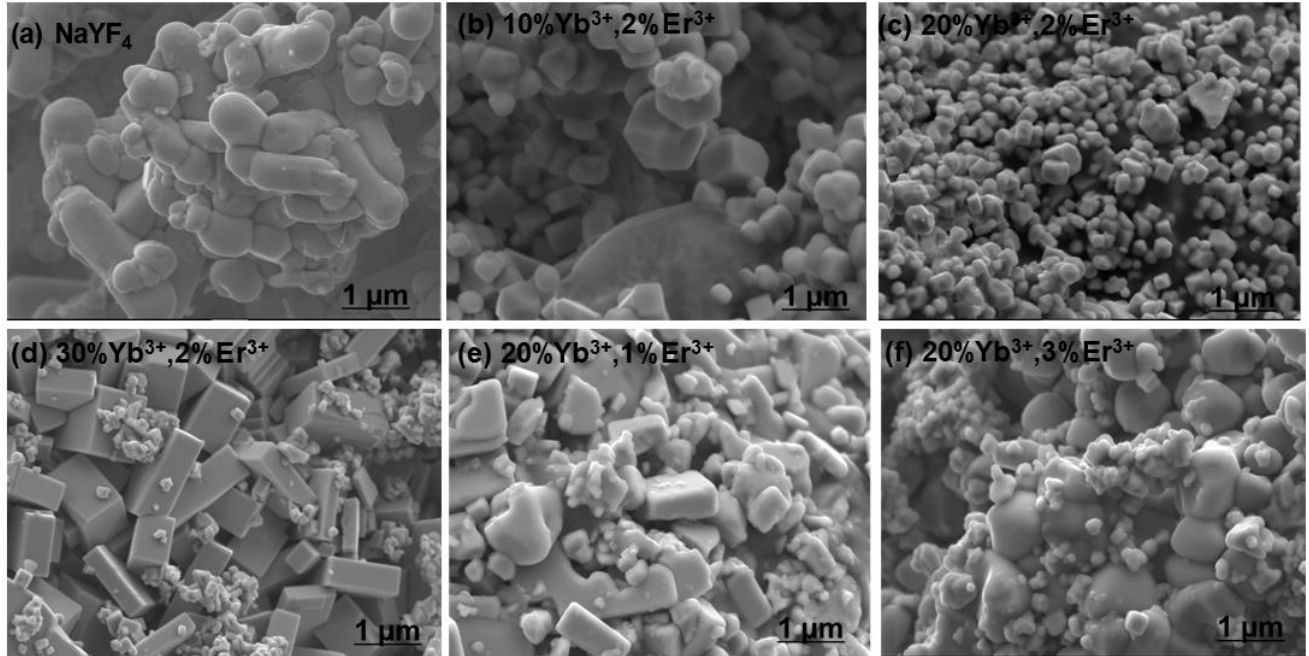


Figure 4.8. FE-SEM images of the undoped and Yb³⁺ – Er³⁺ co-doped NaYF₄ nanocrystals, annealed at 600 °C.

Figure 4.9(a-f) depicts the annealed samples at 700 °C. The undoped NaYF₄ and the samples where Yb³⁺ was varied (10–30 mol%) revealed the formation of a non-uniform morphology with pores. The observed pores are due to the gases that come out of the surface during the combustion process and the high annealing temperatures. When Er³⁺ was varied (1–3 mol%), the NaYF₄:20%Yb³⁺,1%Er³⁺ sample showed a spherical

morphology, whereas the $\text{NaYF}_4\text{:}20\%\text{Yb}^{3+},3\%\text{Er}^{3+}$ sample showed a cubically structured morphology. All samples annealed at 700 °C showed agglomeration of particles, which could be attributed to the high annealing temperature and weak magnetic interactions between the particles [36]. The particle sizes of the nanocrystals decreased with an increase in annealing temperatures.

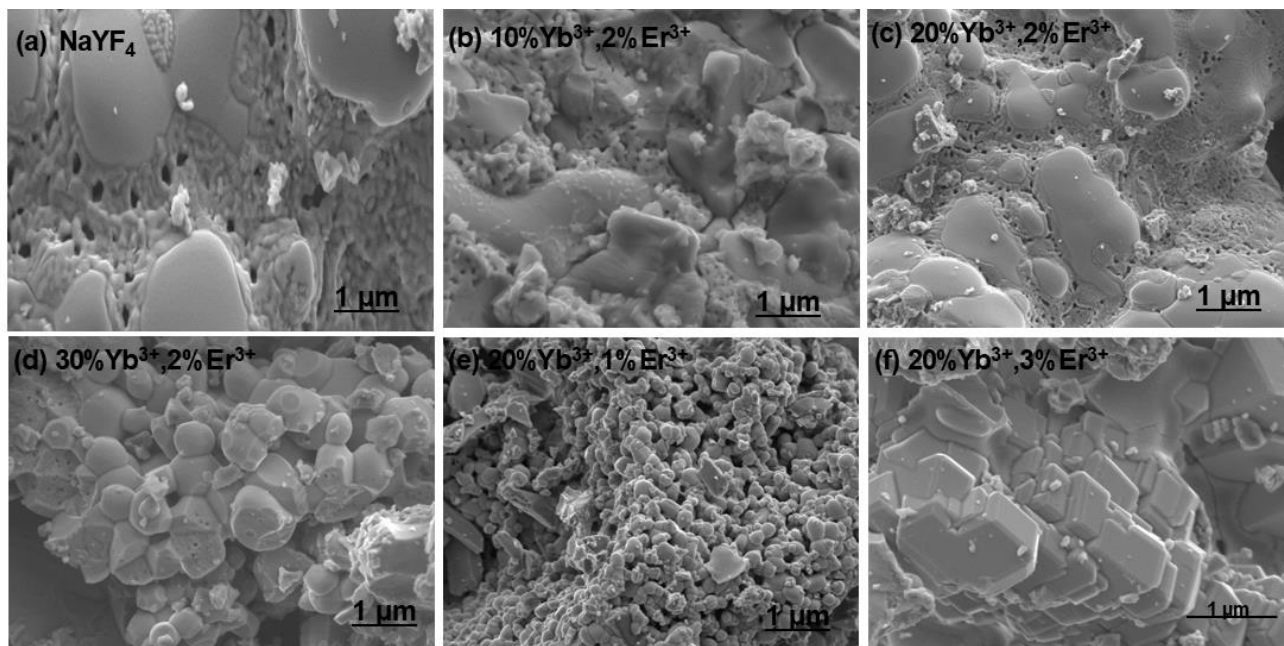


Figure 4.9. FE-SEM images of the undoped and Yb^{3+} – Er^{3+} co-doped NaYF_4 nanocrystals, annealed at 700 °C.

In figures 4.10–4.12, the concentration of Nd^{3+} ions were maintained at a constant level of 2 mol%, while the concentration of Yb^{3+} ions was varied from 10 to 30 mol%. Again, the concentration of Yb^{3+} ions was kept constant at 20 mol%, while that of Nd^{3+} ions was changed from 1 to 3 mol% when doping the NaGdF_4 host. A distinct variation in morphologies is observed in the process of altering dopant concentrations and annealing temperatures. As shown in Figure 4.10, all as-prepared nanocrystals have a non-uniform irregular morphology.

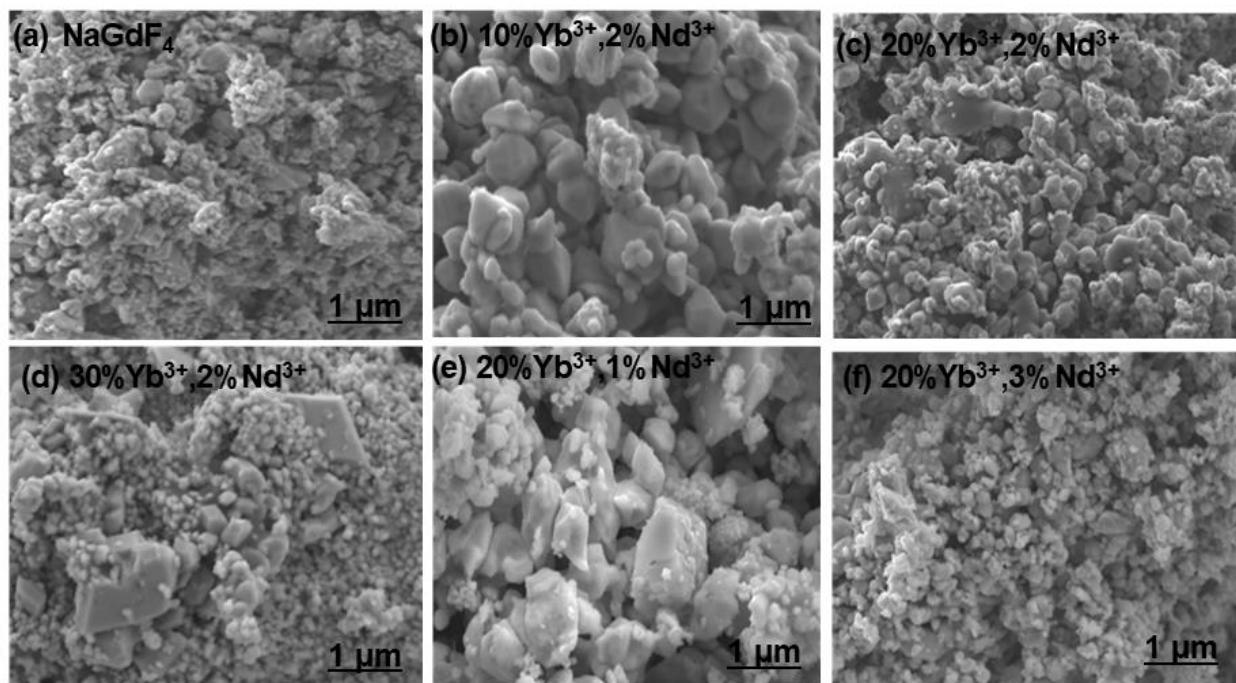


Figure 4.10: FE-SEM images of the undoped and Yb^{3+} – Nd^{3+} co-doped NaGdF_4 nanocrystals, before annealing.

The undoped NaGdF_4 and the $\text{NaGdF}_4\text{:}10\%\text{Yb}^{3+}, 2\%\text{Nd}^{3+}$ samples exhibit a non-uniform irregular morphology after being annealed at $600\text{ }^\circ\text{C}$, whereas the $\text{NaGdF}_4\text{:}20\%\text{Yb}^{3+}, 2\%\text{Nd}^{3+}$, $\text{NaGdF}_4\text{:}30\%\text{Yb}^{3+}, 2\%\text{Nd}^{3+}$, $\text{NaGdF}_4\text{:}20\%\text{Yb}^{3+}, 1\%\text{Nd}^{3+}$, $\text{NaGdF}_4\text{:}20\%\text{Yb}^{3+}, 3\%\text{Nd}^{3+}$ samples exhibit a cubic morphology (see figure 4.11).

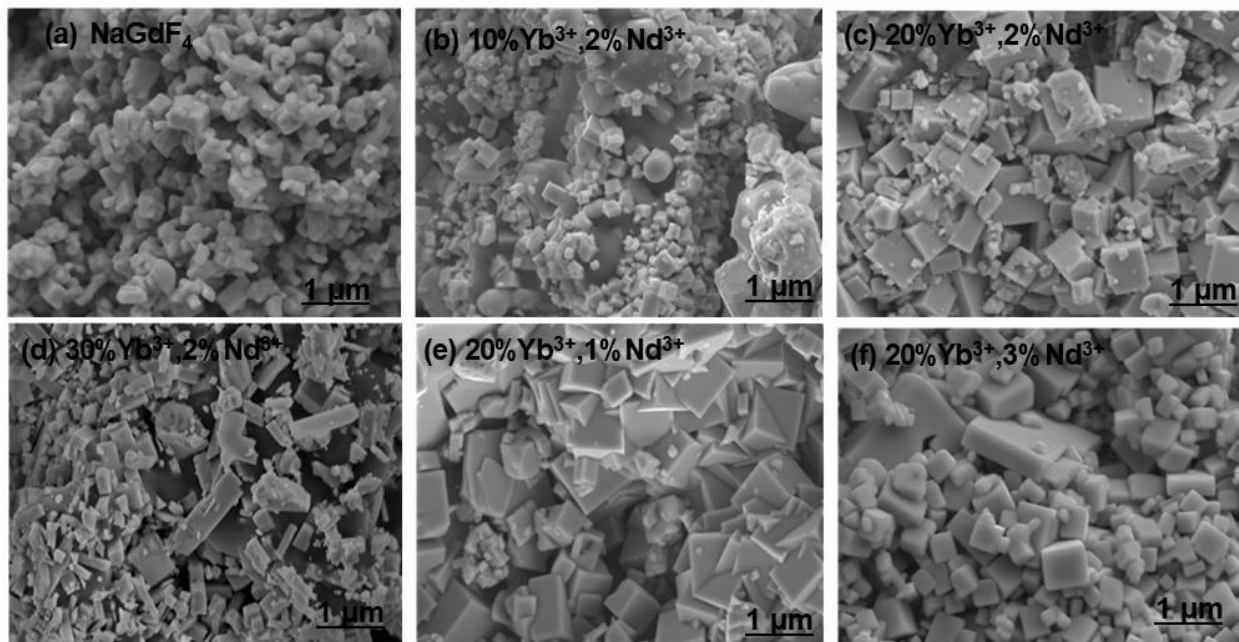


Figure 4.11. FE-SEM images of the undoped and Yb^{3+} – Nd^{3+} co-doped NaGdF_4 nanocrystals, annealed at 600 °C.

When the annealing temperature was increased to 700 °C, an irregular shaped morphology with agglomeration was observed for all the nanocrystals as shown in figure 4.12. These results suggest that altering the concentrations of the dopants Yb^{3+} and Er^{3+} on NaYF_4 and Yb^{3+} and Nd^{3+} on NaGdF_4 , as well as the annealing temperatures, significantly affects the morphology of the NaYF_4 and NaGdF_4 nanocrystals. As confirmed by XRD results, the crystal structure was greatly affected by the annealing temperatures, and this discovery is consistent with the FE-SEM results.

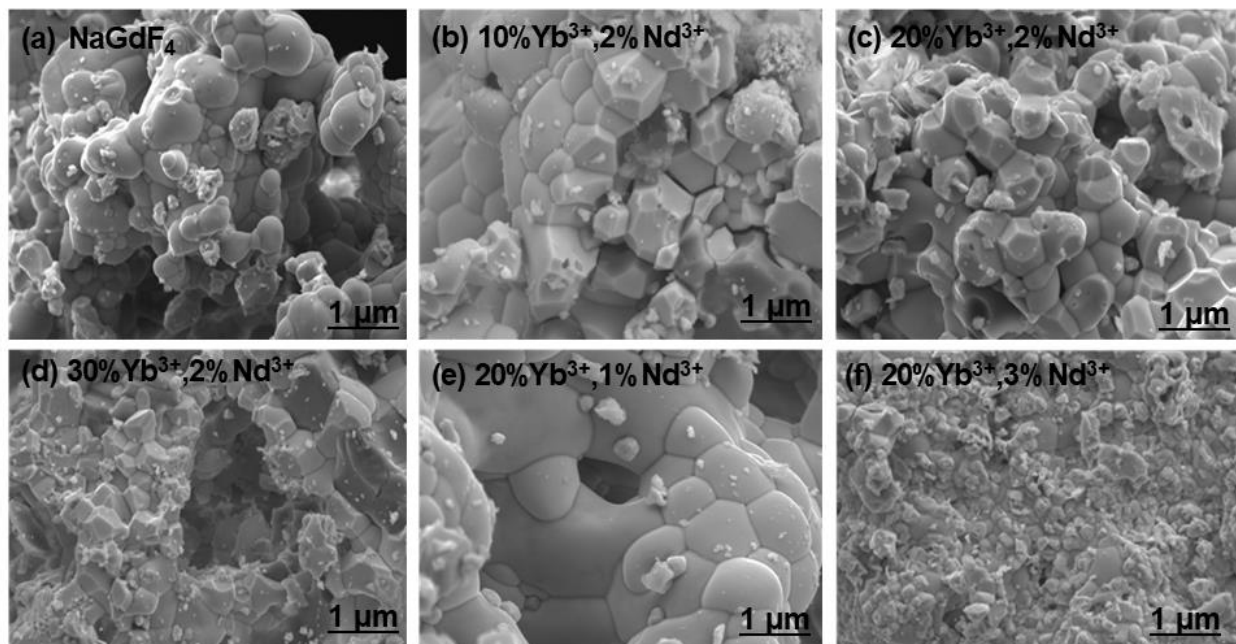


Figure 4.12. FE-SEM images of the undoped and Yb³⁺ – Nd³⁺ co-doped NaGdF₄ nanocrystals, annealed at 700 °C.

EDS studies were further conducted to evaluate the elemental composition of the manufactured nanocrystals. As illustrated in Figure 4.13 (a-b), expected elements like sodium (Na), yttrium (Y), fluorine (F), ytterbium (Yb), and erbium (Er) were confirmed. Figure 4.14(a-b) shows the expected elements like sodium (Na), gadolinium (Gd), fluorine (F), ytterbium (Yb), and neodymium (Nd). For both the undoped NaYF₄ and NaGdF₄ as well as the Yb³⁺-Er³⁺ co-doped NaYF₄ and the Yb³⁺-Nd³⁺ co-doped NaGdF₄, the corresponding elemental mappings of Na, Y, F, Yb, and Er elements in NaYF₄ and Na, Gd, F, Yb, and Nd elements in NaGdF₄ nanocrystals are shown in Figures 4.15 and 4.16. Elemental mapping was done to show the distribution of the elements across the surface of the nanocrystals.

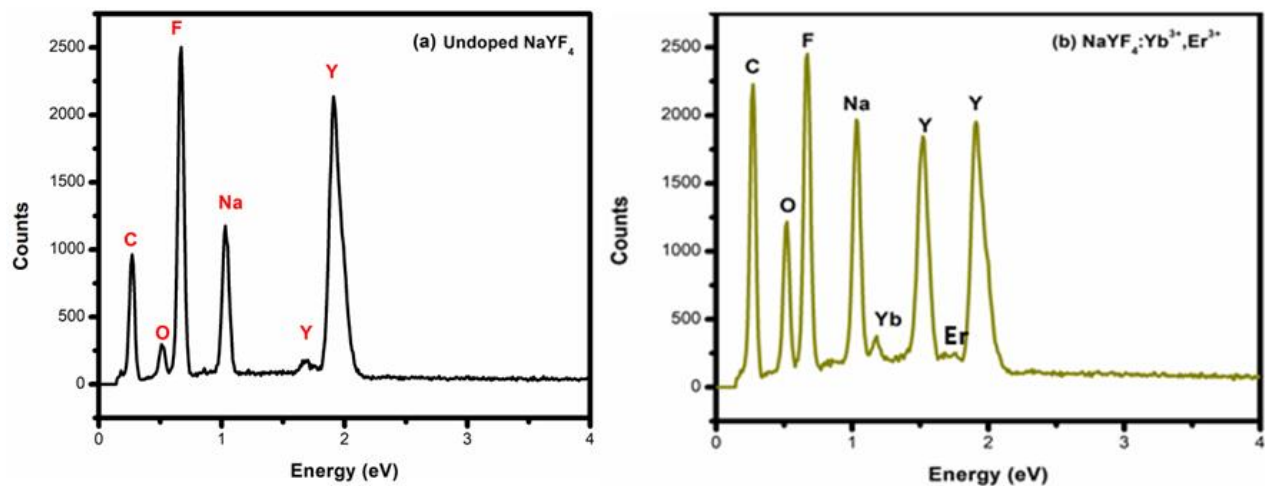


Figure 4.13. EDS spectra of (a) NaYF_4 (b) $\text{NaYF}_4:\text{Yb}^{3+},\text{Er}^{3+}$.

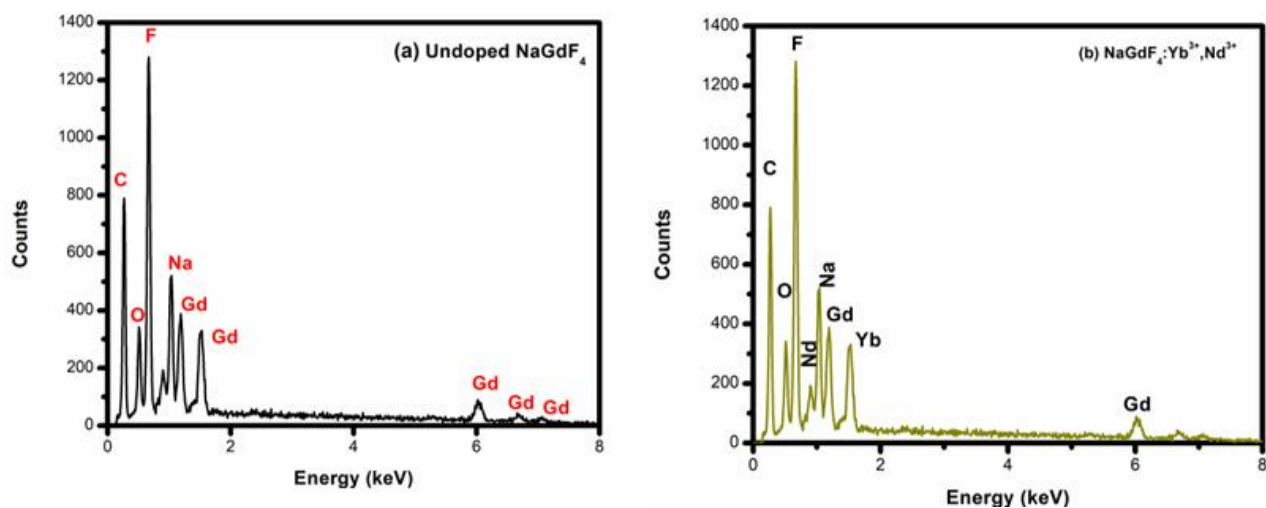


Figure 4.14. EDS spectra of (a) NaGdF_4 (b) $\text{NaGdF}_4:\text{Yb}^{3+},\text{Nd}^{3+}$.

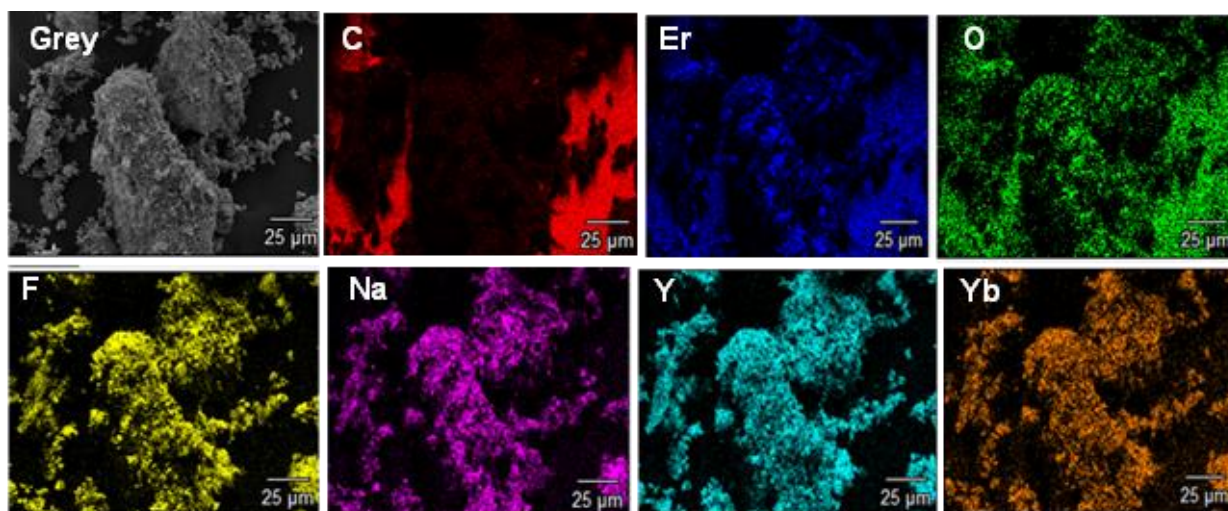


Figure 4.15. Elemental mapping of the $\text{Yb}^{3+} - \text{Er}^{3+}$ co-doped NaYF_4 nanocrystals.

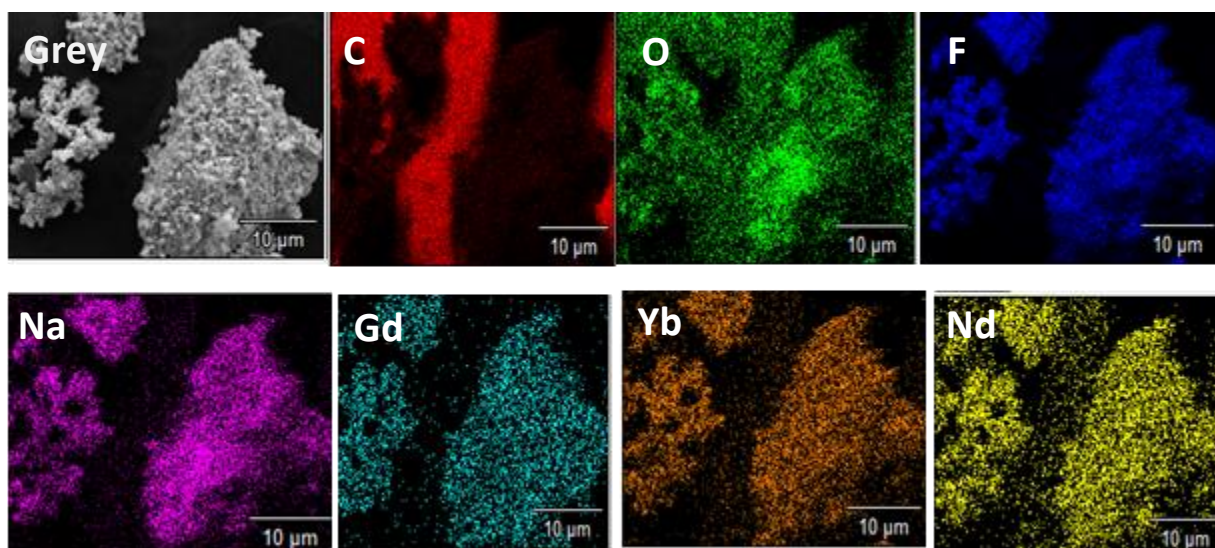


Figure 4.16. Elemental mapping of the $\text{Yb}^{3+} - \text{Nd}^{3+}$ co-doped NaGdF_4 nanocrystals.

4.2.3 Thermogravimetric (TGA) analysis

To investigate the stability of the samples, the as-prepared $\text{NaYF}_4:20\%\text{Yb}^{3+},2\%\text{Er}^{3+}$ and $\text{NaGdF}_4:20\%\text{Yb}^{3+},2\%\text{Nd}^{3+}$ nanocrystals were analysed using TGA. This was done to observe the stability temperatures of the samples. Figure 4.17 shows the TGA curve of the $\text{NaYF}_4:20\%\text{Yb}^{3+},2\%\text{Er}^{3+}$ nanocrystals, indicating a total weight loss of 10.23% in the temperature region from 20 to 690 °C. The initial drop in weight of 3.01% in the range 20–400 °C is ascribed to the water loss [37–38]. The evaporation of the nitrates present on the nanocrystals' surface is responsible for the second, more extreme loss of 7.22% in the range 450–680 °C [37].

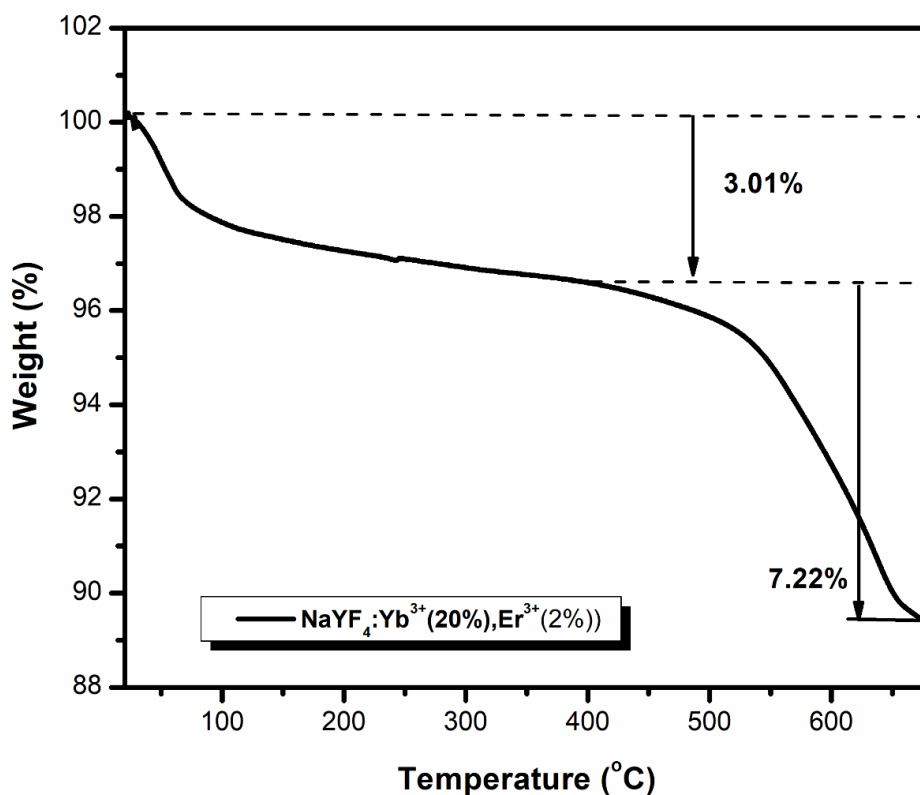


Figure 4.17: Thermogravimetric analysis (TGA) curves of $\text{NaYF}_4:20\%\text{Yb}^{3+},2\%\text{Er}^{3+}$ nanocrystals.

The TGA curve of the as-prepared $\text{NaGdF}_4:20\% \text{Yb}^{3+}, 2\% \text{Nd}^{3+}$ nanocrystals is shown in Figure 4.18, revealing a total weight loss of 5.43 % in the temperature range from 10 to 690 °C. The initial 0.78% loss of weight at temperatures ranging from 10 to 400 °C is attributed to water loss [37–38]. The second, more severe loss of 4.01 % and the third loss of 0.64 % between 450 and 660 °C are both attributed to the evaporation of nitrates that are present on the nanocrystal surface [37]. This showed the stability temperatures of the nanocrystals. The stable nanocrystals are crucial for optical application.

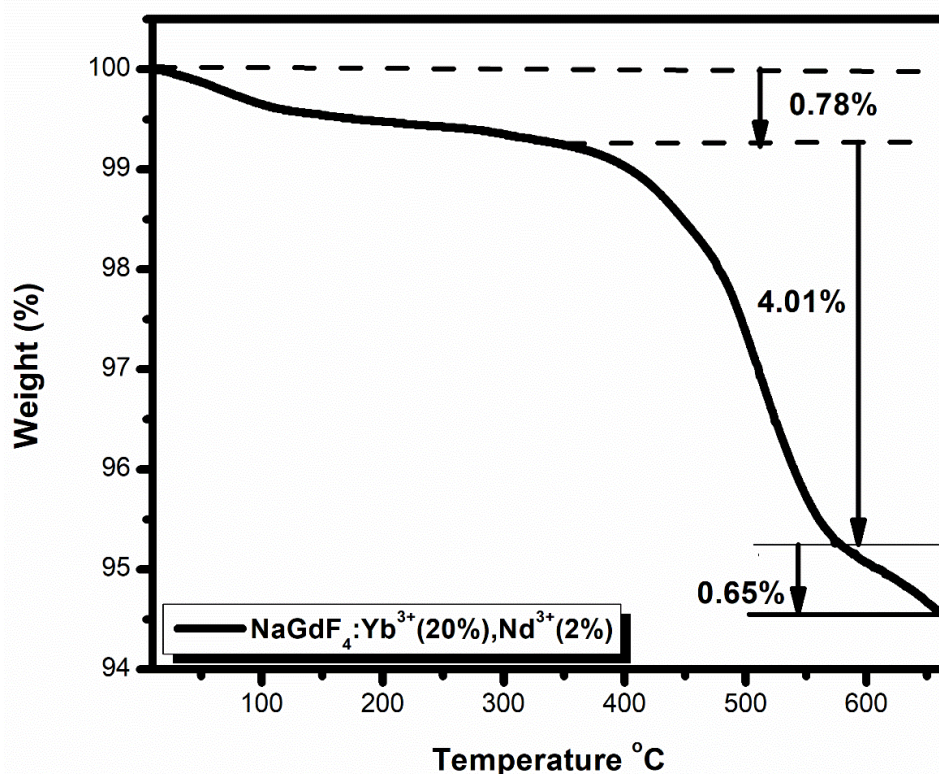


Figure 4.18: Thermogravimetric analysis (TGA) curves of $\text{NaGdF}_4:20\% \text{Yb}^{3+}, 2\% \text{Nd}^{3+}$ nanocrystals.

4.2.4 FTIR and Raman Analysis

The vibration modes of molecules in manufactured nanocrystals were studied using FTIR spectroscopy in the wavenumber range of 500 to 200 cm^{-1} (Figures 4.19 and 4.20). Figure 4.19(a) shows the FTIR spectra of the undoped NaYF_4 , $\text{NaYF}_4:10\% \text{Yb}^{3+}, 2\% \text{Er}^{3+}$, $\text{NaYF}_4:20\% \text{Yb}^{3+}, 2\% \text{Er}^{3+}$, and $\text{NaYF}_4:30\% \text{Yb}^{3+}, 2\% \text{Er}^{3+}$ nanocrystals, Figure 4.19(b)

shows the comparison of the $\text{NaYF}_4:20\%\text{Yb}^{3+},2\%\text{Er}^{3+}$ as-prepared, annealed at 600 °C and annealed at 700 °C. All the samples exhibited the same spectral pattern. The presence of the $\text{RE}^{3+}\text{--F}$ stretching vibrations in the nanocrystals is confirmed by the peak at $\sim 834\text{ cm}^{-1}$ [39]. The peaks at ~ 1120 and ~ 2075 , and $\sim 2339\text{ cm}^{-1}$ are assigned to the C-O stretching vibration of the carboxyl groups. The bands at ~ 1380 and $\sim 1645\text{ cm}^{-1}$ are attributed to the symmetric and asymmetric stretching vibrations of the carboxylate anions, implying the strong --COO--RE^{3+} complex formation on the nanocrystals surface. The broad band exhibited by the nanocrystals at around 3463 cm^{-1} is assigned to the O-H stretching vibration [40]. Figure 4.19(b) indicates that increasing the annealing temperature on $\text{NaYF}_4:20\%\text{Yb}^{3+},2\%\text{Er}^{3+}$ nanocrystals increase the transmittance %. These results confirm that the dopants have been successfully embedded in the NaYF_4 host.

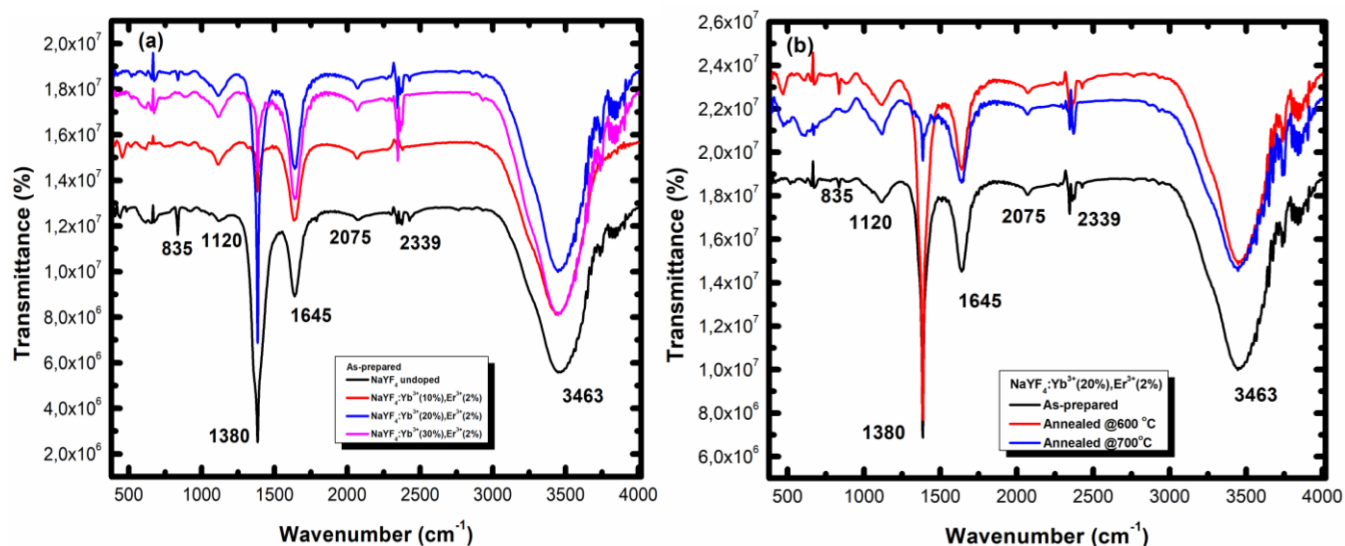


Figure 4.19. FTIR spectra of (a) as-prepared $\text{Yb}^{3+}\text{--Er}^{3+}$ co-doped NaYF_4 nanocrystals and (b) comparison of annealed nanocrystals at 600 °C and 700 °C.

Figure 4.20(a) below shows the FTIR spectra of the undoped NaGdF_4 , $\text{NaGdF}_4:10\%\text{Yb}^{3+},2\%\text{Nd}^{3+}$, $\text{NaGdF}_4:20\%\text{Yb}^{3+},2\%\text{Nd}^{3+}$, and $\text{NaGdF}_4:30\%\text{Yb}^{3+},2\%\text{Nd}^{3+}$ nanocrystals and Figure 4.20(b) shows the comparison of the $\text{NaGdF}_4:20\%\text{Yb}^{3+},2\%\text{Nd}^{3+}$ as-prepared, annealed at 600 °C and annealed at 700 °C. All the samples exhibited the same spectral pattern. The presence of the $\text{RE}^{3+}\text{--F}$ stretching vibrations in the

nanocrystals is confirmed by the peak at $\sim 640\text{ cm}^{-1}$ [39]. The peaks at ~ 1116 and ~ 2077 , and $\sim 2416\text{ cm}^{-1}$ are assigned to the C-O stretching vibration of the carboxyl groups. The bands at ~ 1398 and $\sim 1638\text{ cm}^{-1}$ are attributed to the symmetric and asymmetric stretching vibrations of the carboxylate anions, implying the strong -COO-RE^{3+} complex formation on the nanocrystals surface. The broad band at around 3456 cm^{-1} is assigned to the O-H stretching vibration [40]. When the nanocrystals are annealed at $600\text{ }^{\circ}\text{C}$ and $700\text{ }^{\circ}\text{C}$, the transmittance % increases with an increase in the annealing temperature, as indicated by Figure 4.20(b).

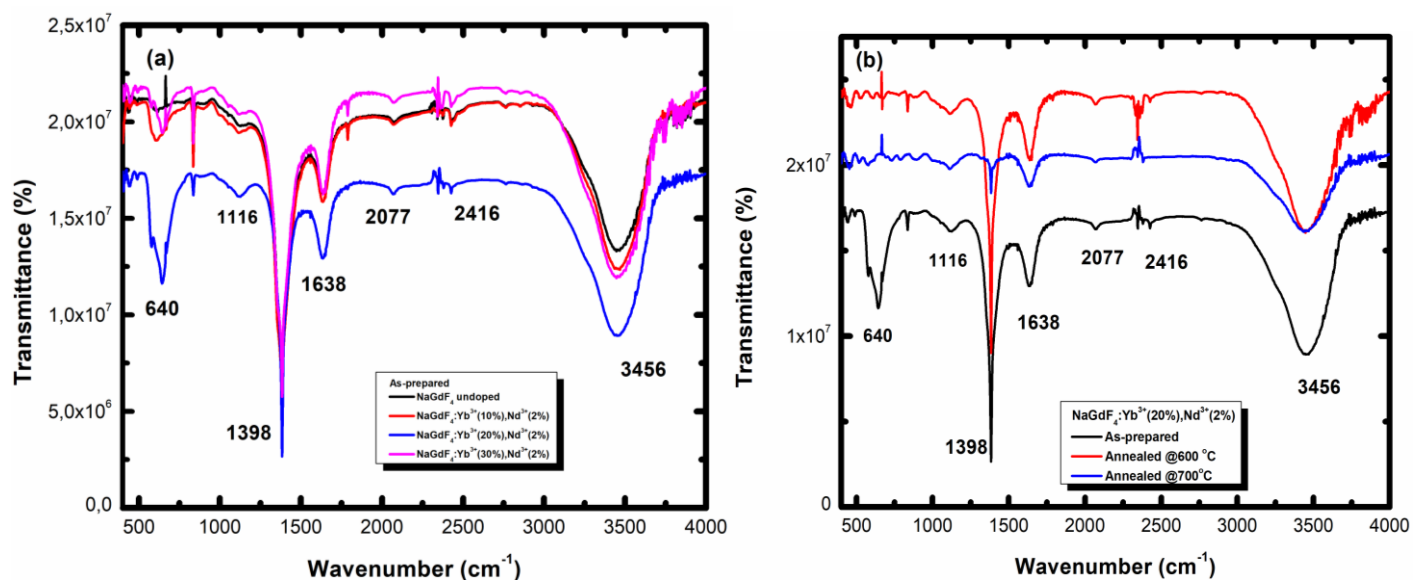


Figure 4.20. FTIR spectra of (a) as-prepared Yb^{3+} - Nd^{3+} co-doped NaGdF_4 nanocrystals and (b) comparison of annealed nanocrystals at $600\text{ }^{\circ}\text{C}$ and $700\text{ }^{\circ}\text{C}$.

To discover the non-radiative relaxations, the vibrational modes of the synthesized nanocrystals were studied. Figure 4.21(a-c) illustrates the Raman spectra of the as-prepared $\text{NaYF}_4:x\%\text{Yb}^{3+},2\%\text{Er}^{3+}$ ($x = 10, 20$, and 30) and $\text{NaYF}_4:20\%\text{Yb}^{3+},2\%\text{Er}^{3+}$ annealed at $600\text{ }^{\circ}\text{C}$ and $700\text{ }^{\circ}\text{C}$ nanocrystals. The clear and distinct peaks between 150 and 750 cm^{-1} , and 1000 cm^{-1} of the hexagonal phase nanocrystals (as-prepared and the $\text{NaYF}_4:20\%\text{Yb}^{3+},2\%\text{Er}^{3+}$ annealed at $600\text{ }^{\circ}\text{C}$) are attributable to the lattice of the NaYF_4 vibrational characteristics. The Na-F pair of atoms' vibrational frequencies are assigned

to peaks between 460 and 770 cm^{-1} . The occurrence of the -OH band between 1300 and 1400 cm^{-1} is clearly visible in the as-prepared sample $\text{NaYF}_4:\text{Yb}^{3+}(10\%),\text{Er}^{3+}(2\%)$, and is assigned to the phonon frequencies of Y-OH. Induced strain could be the cause of the difference in peak intensity [41]. The $\text{NaYF}_4:20\%\text{Yb}^{3+},2\%\text{Er}^{3+}$ nanocrystals annealed at 700 $^{\circ}\text{C}$ shows two dominant broad bands around 366 and 750 cm^{-1} .

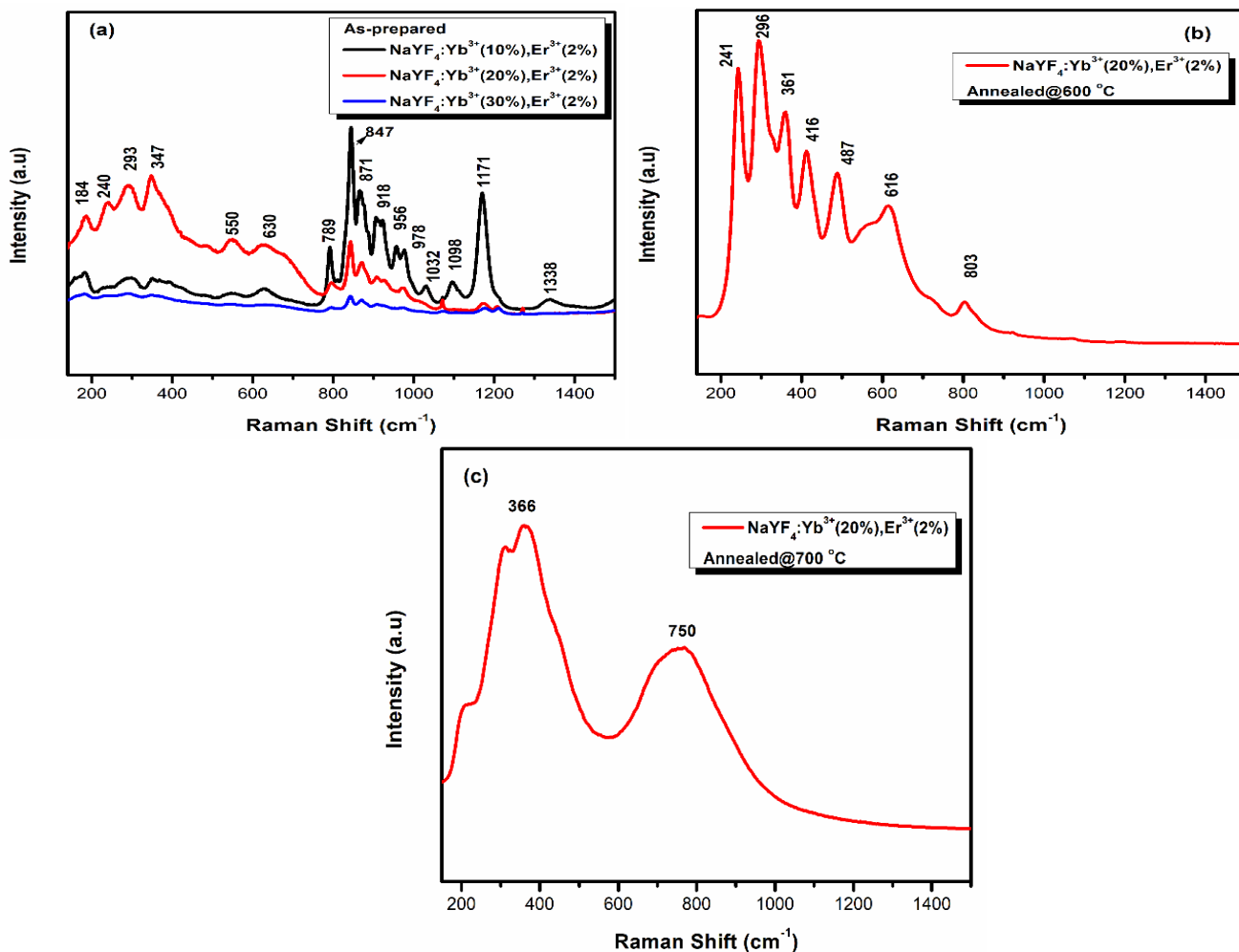


Figure 4.21: Raman spectra of $\text{NaYF}_4:10\%\text{Yb}^{3+},2\%\text{Er}^{3+}$, $\text{NaYF}_4:20\%\text{Yb}^{3+},2\%\text{Er}^{3+}$, and $\text{NaYF}_4:30\%\text{Yb}^{3+},2\%\text{Er}^{3+}$ nanocrystals (a) as-prepared (b) $\text{NaYF}_4:20\%\text{Yb}^{3+},2\%\text{Er}^{3+}$ annealed at 600 $^{\circ}\text{C}$ (c) $\text{NaYF}_4:20\%\text{Yb}^{3+},2\%\text{Er}^{3+}$ annealed at 700 $^{\circ}\text{C}$.

The Raman spectra of undoped and Yb³⁺-Nd³⁺ doped NaGdF₄ nanocrystals in the wave range 200 to 1500 nm are shown in Figure 4.22. The dominant high intensity peaks between 200 and 490 cm⁻¹ are attributed to the β-NaGdF₄:xYb³⁺,xNd³⁺ nanocrystals' lattice phonon modes [42]. The peaks between 461 and 763 cm⁻¹ are assigned to the vibrational frequencies of Na-F [41–42]. The peaks between 905 and 1168 nm that are increasing with an increase in Yb³⁺ concentrations are assigned to the vibrational bands of ytterbium nitrates [43]. The band at 1378 cm⁻¹ is attributed to the phonon frequencies of Y-OH [41]. The peak intensity increased, and the peaks shifted after annealing the samples at 600 and 700 °C. This means that the fraction of substance in the samples contributing to the vibrational mode increased with an increase in annealing temperatures [42]. The chemical bond length of the molecules, which causes electron cloud migration, is linked to the observed shifting of the Raman peaks towards a lower or higher wavenumber [43]. A movement to a higher wavenumber is brought on by a shorter bond length, whereas a shift to a lower wavenumber is brought on by a longer bond length [38]. Raman spectra confirm the structural behaviour of the synthesized samples. These results support the related XRD data indicating the hexagonal and cubic phases for the respective nanocrystals.

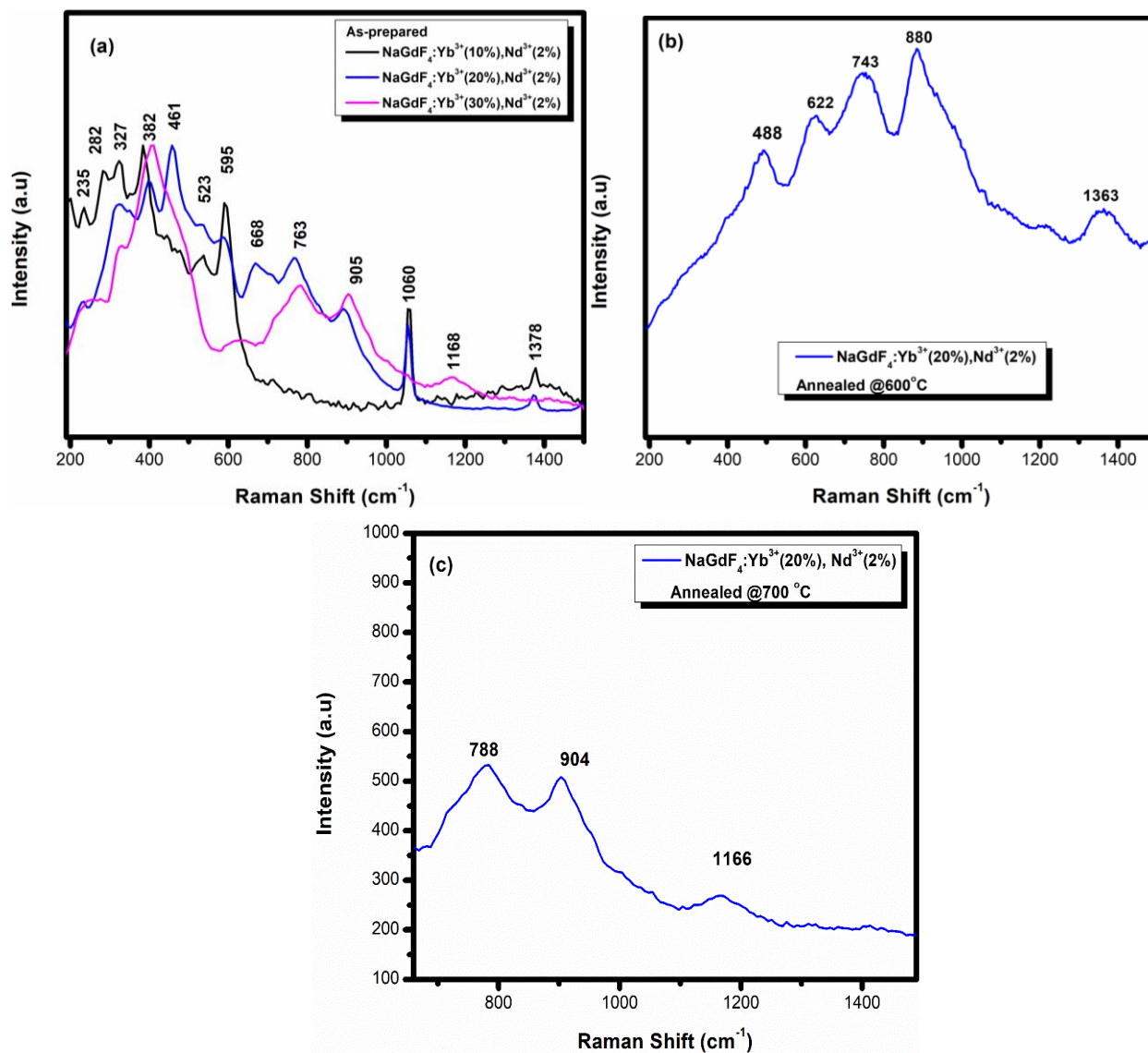


Figure 4.22: Raman spectra of NaGdF₄:10%Yb³⁺,2%Nd³⁺, NaGdF₄:20%Yb³⁺,2%Nd³⁺, and NaGdF₄:30%Yb³⁺,2%Nd³⁺ nanocrystals (a) as-prepared (b) NaGdF₄:20%Yb³⁺,2%Nd³⁺ annealed at 600 °C (c) NaGdF₄:20%Yb³⁺,2%Nd³⁺ annealed at 700 °C.

Conclusion

$\text{NaYF}_4:\text{Yb}^{3+},\text{Er}^{3+}$ and $\text{NaGdF}_4:\text{Yb}^{3+},\text{Nd}^{3+}$ nanocrystals were successfully synthesized by the solution combustion method, and the influence of the concentration of the dopants and the annealing temperature on the structure, morphology, and optical properties were examined. Both $\text{NaYF}_4:\text{Yb}^{3+},\text{Er}^{3+}$ and $\text{NaGdF}_4:\text{Yb}^{3+},\text{Nd}^{3+}$ nanocrystals were annealed at 600 and 700 °C, respectively. For the $\text{NaYF}_4:\text{Yb}^{3+},\text{Er}^{3+}$ nanocrystals, XRD analysis indicated the hexagonal phase for the as-prepared and the nanocrystals annealed at 600 °C and the cubic phases for the 700 °C annealed nanocrystals. While for the $\text{NaGdF}_4:\text{Yb}^{3+},\text{Nd}^{3+}$ nanocrystals, XRD analysis indicated the hexagonal phase for all prepared nanocrystals.

The XRD patterns revealed that doping NaYF_4 and NaGdF_4 leads to a shift in diffraction peaks, a broadening, and a change in peak intensities. The nanocrystals demonstrated different morphologies, including spherical, cubic, hexagonal, non-uniform, irregular, and porous, as dopant concentrations (10–30 mol% of Yb^{3+} , 1–3 mol% of Er^{3+} , and Nd^{3+}) and annealing temperatures were changed. TGA analysis showed the stability temperatures of the $\text{NaYF}_4:20\%\text{Yb}^{3+},2\%\text{Er}^{3+}$ and the $\text{NaGdF}_4:20\%\text{Yb}^{3+},2\%\text{Nd}^{3+}$ samples, with two weight losses of 3.01% and 7.22% in the wave ranges 20-400 °C and 450-680 °C for the $\text{NaYF}_4:20\%\text{Yb}^{3+},2\%\text{Er}^{3+}$ sample, and three weight losses of 0.78 %, 4.01 %, and 0.65 % in the wave ranges of 10-400 °C and 450-660 °C for the $\text{NaGdF}_4:20\%\text{Yb}^{3+},2\%\text{Nd}^{3+}$ sample which are all assigned to the water loss and the evaporation of the nitrate ions.

FTIR spectra showed the expected vibrational modes of the NaYF_4 , $\text{NaYF}_4:\text{Yb}^{3+},\text{Er}^{3+}$, NaGdF_4 , and $\text{NaGdF}_4:\text{Yb}^{3+},\text{Nd}^{3+}$ nanocrystals. An increase in the intensity was noted in the FTIR spectra of the $\text{NaYF}_4:20\%\text{Yb}^{3+},2\%\text{Er}^{3+}$ and $\text{NaGdF}_4:20\%\text{Yb}^{3+},2\%\text{Nd}^{3+}$ nanocrystals. Raman spectra revealed the clear and distinct peaks between 150 and 750 cm^{-1} , and 1000 cm^{-1} of the hexagonal phase nanocrystals (as-prepared and the $\text{NaYF}_4:20\%\text{Yb}^{3+},2\%\text{Er}^{3+}$ annealed at 600 °C), which were attributed to the host lattice NaYF_4 vibrational characteristics. For the $\text{NaGdF}_4:\text{Yb}^{3+},\text{Nd}^{3+}$ nanocrystals, Raman spectra revealed the peaks assigned to the lattice phonon modes of the β - $\text{NaGdF}_4:\text{xYb}^{3+},\text{xNd}^{3+}$ nanocrystals between 200 and 490 cm^{-1} , vibrational frequencies of

Na-F between 461 and 763 cm^{-1} , vibrational bands of ytterbium nitrates between 905 and 1168 cm^{-1} , and phonon frequencies of Y-OH at 1378 cm^{-1} . Upon annealing the samples at 600 °C and 700 °C, the enhancement in the peak intensity and also the shifting of the peaks was observed. The Raman results agreed well with the XRD data.

References

- [1]. He, S., Xia, H., Zhang, J., Zhu, Y. and Chen, B., 2017. Highly efficient up-conversion luminescence in Er³⁺/Yb³⁺ co-doped Na₅Lu₉F₃₂ single crystals by vertical Bridgman method. *Scientific reports*, 7(1), pp.1-9.
- [2]. Anderson, R.B., Smith, S.J., May, P.S. and Berry, M.T., 2014. Revisiting the NIR-to-visible upconversion mechanism in β -NaYF₄: Yb³⁺, Er³⁺. *The journal of physical chemistry letters*, 5(1), pp.36-42.
- [3]. Li, X., Zhang, F. and Zhao, D., 2013. Highly efficient lanthanide upconverting nanomaterials: progresses and challenges. *Nano Today*, 8(6), pp.643-676.
- [4]. Pandey, A., Tiwari, S.P., Dutta, V. and Kumar, V., 2018. Photon Upconversion in Lanthanide-Activated Inorganic Luminescent Materials. In *Emerging Synthesis Techniques for Luminescent Materials* (pp. 86-116). IGI Global.
- [5]. Talane, T.E., 2017. *Study of Structural and Optical Properties of Undoped and Rare Earth Doped TiO₂ Nanostructures* (Doctoral dissertation).
- [6]. Tiwari, S.P., Maurya, S.K., Yadav, R.S., Kumar, A., Kumar, V., Joubert, M.F. and Swart, H.C., 2018. Future prospects of fluoride based upconversion nanoparticles for emerging applications in biomedical and energy harvesting. *Journal of Vacuum Science & Technology B, Nanotechnology and Microelectronics: Materials, Processing, Measurement, and Phenomena*, 36(6), p.060801.
- [7]. Sun, C., Schäferling, M., Resch-Genger, U. and Gradzielski, M., 2021. Solvothermal synthesis of lanthanide-doped NaYF₄ upconversion crystals with size and shape control: particle properties and growth mechanism. *ChemNanoMat*, 7(2), pp.174-183.
- [8]. Palo, E., Salomäki, M. and Lastusaari, M., 2017. Surface modification of upconverting nanoparticles by layer-by-layer assembled polyelectrolytes and metal ions. *Journal of colloid and interface science*, 508, pp.137-144.

- [9]. Hou, Y., Sheng, Z., Fu, C., Kong, J. and Zhang, X., 2022. Hygroscopic holey graphene aerogel fibers enable highly efficient moisture capture, heat allocation and microwave absorption. *Nature Communications*, 13(1), p.1227.
- [10]. Lenth, W. and Macfarlane, R.M., 1992. Upconversion lasers. *Optics and Photonics News*, 3(3), pp.8-15.
- [11]. Allerhand, A. and von Rague Schleyer, P., 1963. Halide anions as proton acceptors in hydrogen bonding. *Journal of the American Chemical Society*, 85(9), pp.1233-1237.
- [12]. Chen, J. and Zhao, J.X., 2012. Upconversion nanomaterials: synthesis, mechanism, and applications in sensing. *Sensors*, 12(3), pp.2414-2435.
- [13]. López-Luke, T., De La Rosa, E., González-Yebra, A.L., González-Yebra, B., Ángeles-Chávez, C., Solís, D., Salas, P., Saldaña, C. and Meza, O., 2010, February. Synthesis and characterization of upconversion emission on lanthanides doped ZrO_2 nanocrystals coated with SiO_2 for biological applications. In *Reporters, Markers, Dyes, Nanoparticles, and Molecular Probes for Biomedical Applications II* (Vol. 7576, pp. 161-170). SPIE.
- [14]. Vidyakina, A.A., Kolesnikov, I.E., Bogachev, N.A., Skripkin, M.Y., Tumkin, I.I., Lähderanta, E. and Mereshchenko, A.S., 2020. Gd^{3+} -Doping Effect on Upconversion Emission of $\text{NaYF}_4\text{:Yb}^{3+}, \text{Er}^{3+}/\text{Tm}^{3+}$ Microparticles. *Materials*, 13(15), p.3397.
- [15]. Huang, X., 2016. Realizing efficient upconversion and down-shifting dual-mode luminescence in lanthanide-doped NaGdF_4 core-shell-shell nanoparticles through gadolinium sublattice-mediated energy migration. *Dyes and Pigments*, 130, pp.99-105.
- [16]. Jonathan, L., Diguna, L.J., Samy, O., Muqoyyanah, M., Abu Bakar, S., Birowosuto, M.D. and El Moutaouakil, A., 2022. Hybrid organic-inorganic perovskite halide materials for photovoltaics towards their commercialization. *Polymers*, 14(5), p.1059.
- [17]. Kavand, A., Serra, C.A., Blanck, C., Lenertz, M., Anton, N., Vandamme, T.F., Mély, Y., Przybilla, F. and Chan-Seng, D., 2021. Controlled Synthesis of $\text{NaYF}_4\text{:Yb, Er}$ Upconversion Nanocrystals as Potential Probe for Bioimaging: A Focus on Heat Treatment. *ACS Applied Nano Materials*.

- [18]. Shan, S.N., Wang, X.Y. and Jia, N.Q., 2011. Synthesis of NaYF₄: Yb³⁺, Er³⁺ upconversion nanoparticles in normal microemulsions. *Nanoscale research letters*, 6(1), pp.1-5.
- [19]. Hakmeh, N., Chlique, C., Merdrignac-Conanec, O., Fan, B., Cheviré, F., Zhang, X., Fan, X. and Qiao, X., 2015. Combustion synthesis and up-conversion luminescence of La₂O₂S: Er³⁺, Yb³⁺ nanophosphors. *Journal of Solid State Chemistry*, 226, pp.255-261.
- [20]. Roh, J., Yu, H. and Jang, J., 2016. Hexagonal β -NaYF₄: Yb³⁺, Er³⁺ nanoprism-incorporated upconverting layer in perovskite solar cells for near-infrared sunlight harvesting. *ACS Applied Materials & Interfaces*, 8(31), pp.19847-19852.
- [21]. Huang, Q., Ye, W., Jiao, X., Yu, L., Liu, Y. and Liu, X., 2018. Efficient upconversion fluorescence in NaYF₄: Yb³⁺, Er³⁺/mNaYF₄ multilayer core-shell nanoparticles. *Journal of Alloys and Compounds*, 763, pp.216-222.
- [22]. Jia, F., Li, G., Yang, B., Yu, B., Shen, Y. and Cong, H., 2019. Investigation of rare earth upconversion fluorescent nanoparticles in biomedical field. *Nanotechnology Reviews*, 8(1), pp.1-17.
- [23]. Ansari, A.A., Parchur, A.K., Nazeeruddin, M.K. and Tavakoli, M.M., 2021. Luminescent lanthanide nanocomposites in thermometry: Chemistry of dopant ions and host matrices. *Coordination Chemistry Reviews*, 444, p.214040.
- [24]. Zheng, W., Sun, B., Li, Y., Wang, R. and Xu, Y., 2019. Multicolor tunable luminescence and laser-sensitization induced upconversion enhancement in Ln-doped Gd₂O₃ crystals for anti-counterfeiting. *Materials Chemistry Frontiers*, 3(11), pp.2403-2413.
- [25]. Dong, H., Sun, L.D. and Yan, C.H., 2015. Energy transfer in lanthanide upconversion studies for extended optical applications. *Chemical Society Reviews*, 44(6), pp.1608-1634.
- [26]. Nadort, A., Zhao, J. and Goldys, E.M., 2016. Lanthanide upconversion luminescence at the nanoscale: fundamentals and optical properties. *Nanoscale*, 8(27), pp.13099-13130.

- [27]. Blake, A.J., Cole, J.M., Evans, J.S., Main, P., Parsons, S. and Watkin, D.J., 2009. *Crystal structure analysis: principles and practice* (Vol. 13). OUP Oxford.
- [28]. Srinet, G., Sharma, S., Guerrero-Sanchez, J., Garcia-Diaz, R., Ponce-Perez, R., Siqueiros, J.M. and Herrera, O.R., 2020. Room-temperature ferromagnetism on ZnO nanoparticles doped with Cr: An experimental and theoretical analysis. *Journal of Alloys and Compounds*, 849, p.156587.
- [29]. Karamat, S., Rawat, R.S., Lee, P., Tan, T.L. and Ramanujan, R.V., 2014. Structural, elemental, optical and magnetic study of Fe doped ZnO and impurity phase formation. *Progress in Natural Science: Materials International*, 24(2), pp.142-149.
- [30]. Cheng, W. and Ma, X., 2009, March. Structural, optical and magnetic properties of Fe-doped ZnO. In *Journal of Physics: Conference Series* (Vol. 152, No. 1, p. 012039). IOP Publishing.
- [31]. Mbule, P.S., 2013. *The effects of the ZnO nanoparticles buffer layer on organic solar cells* (Doctoral dissertation, University of the Free State).
- [32]. Manjula, N., Pugalenth, M., Nagarethinam, V.S., Usharani, K. and Balu, A.R., 2015. Effect of doping concentration on the structural, morphological, optical and electrical properties of Mn-doped CdO thin films. *Mater. Sci. Poland*, 33(4), pp.774-781.
- [33]. Przybylska, D. and Grzyb, T., 2020. Synthesis and up-conversion of core/shell SrF₂: Yb³⁺, Er³⁺@ SrF₂: Yb³⁺, Nd³⁺ nanoparticles under 808, 975, and 1532 nm excitation wavelengths. *Journal of Alloys and Compounds*, 831, p.154797.
- [34]. Lekesi, L.P., Motaung, T.E., Motloung, S.V., Koao, L.F. and Malevu, T.D., 2022. Investigation on structural, morphological, and optical studies of multiphase titanium dioxide nanoparticles. *Journal of Molecular Structure*, 1251, p.132014.
- [35]. Ali, D., Butt, M.Z., Muneer, I., Farrukh, M.A., Aftab, M., Saleem, M., Bashir, F. and Khan, A.U., 2019. Synthesis and characterization of sol-gel derived La and Sm doped ZnO thin films: A solar light photo catalyst for methylene blue. *Thin Solid Films*, 679, pp.86-98.

- [36]. Samsonov, D., Zhdanov, S., Morfill, G. and Steinberg, V., 2003. Levitation and agglomeration of magnetic grains in a complex (dusty) plasma with magnetic field. *New Journal of Physics*, 5(1), p.24.
- [37]. Li, Z., Miao, H., Fu, Y., Liu, Y., Zhang, R. and Tang, B., 2016. Fabrication of NaYF₄: Yb, Er nanoprobe for cell imaging directly by using the method of hydron rivalry aided by ultrasonic. *Nanoscale research letters*, 11(1), pp.1-10.
- [38]. Kawai, K., Fukuda, T., Nakano, Y. and Takeshita, K., 2016. Thermal decomposition analysis of simulated high-level liquid waste in cold-cap. *EPJ Nuclear Sciences & Technologies*, 2, p.44.
- [39]. Giang, L.T.K., Trejgis, K., Marciniak, L., Vu, N. and Minh, L.Q., 2020. Fabrication and characterization of up-converting β -NaYF₄: Er³⁺, Yb³⁺@ NaYF₄ core-shell nanoparticles for temperature sensing applications. *Scientific Reports*, 10(1), pp.1-12.
- [40]. Zhao, P., Wu, Y., Zhu, Y., Yang, X., Jiang, X., Xiao, J., Zhang, Y. and Li, C., 2014. Upconversion fluorescent strip sensor for rapid determination of *Vibrio anguillarum*. *Nanoscale*, 6(7), pp.3804-3809.
- [41]. Wan, F., Shi, H., Chen, W., Gu, Z., Du, L., Wang, P., Wang, J. and Huang, Y., 2017. Charge transfer effect on raman and surface enhanced raman spectroscopy of furfural molecules. *Nanomaterials*, 7(8), p.210.
- [42]. Khan, L.U., Khan, Z.U., Rodrigues, R.V., da Costa, L.S., Gidlund, M. and Brito, H.F., 2019. Synthesis and characterization of tunable color upconversion luminescence β -NaGdF₄: Yb³⁺, Er³⁺ nanoparticles. *Journal of Materials Science: Materials in Electronics*, 30(18), pp.16856-16863.
- [43]. Tcibulnikova, A.V., Borkunov, R.Y., Bryukhanov, V.V., Slezhkin, V.A., Zyubin, A.Y. and Samusev, I.G., 2018, January. Visible and IR spectroscopy of ablative ytterbium nanoparticles. In *Nanophotonics Australasia 2017* (Vol. 10456, pp. 149-152). SPIE.

CHAPTER 5

Optical and thermoluminescence studies of the $\text{NaYF}_4:\text{Yb}^{3+},\text{Er}^{3+}$ and $\text{NaGdF}_4:\text{Yb}^{3+},\text{Nd}^{3+}$ nanocrystals.

5.1 INTRODUCTION

Luminescence is described as the emission of electromagnetic radiation (light) in the range between UV and IR from solid materials known as phosphors when activated by some type of external energy [1]. It involves the emission of light at a longer wavelength (the emission wavelength) after a chemical molecule absorbs light at a particular wavelength [2]. Luminescence can be categorized in different ways, such as "photoluminescence, cathodoluminescence, radioluminescence, thermoluminescence, electroluminescence, triboluminescence, sonoluminescence, chemiluminescence, and bioluminescence," depending on the excitation source [1, 3]. RE-doped nanophosphors are essential optical and luminous materials for solar cell applications. This is due to the fact that they can go through the UC mechanism process. Studies of the optical behaviour of such materials offer information regarding the interactions between the dopant and the surrounding matrix, as well as energy transfer [4]. The PL (UCL), TL, and optical absorption characteristics of the prepared nanocrystals are examined and discussed in this chapter.

5.2.1 Photoluminescence (PL) analysis

Figure 5.1(a-b) depicts the UPL emission spectra of the as-prepared NaYF_4 nanocrystals doped with various concentrations of Yb^{3+} (10 – 30 mol%) and Er^{3+} (1 – 3 mol%) in the wavelength range from 400 to 800 nm under the excitation wavelength of 980 nm. Figure 5.1(b) shows the UPL spectra while varying the sensitizer. All the samples showed the same spectra and the upconversion luminescence phenomenon, which was first seen by Auzel et al. [5]. The UPL emission spectra shows three significant emission bands at ~483 nm (green light), ~542 nm (green light), and ~665 nm (red light), which are assigned to

$^4H_{11/2} \rightarrow ^4I_{15/2}$, $^4S_{3/2} \rightarrow ^4I_{15/2}$, and $^4F_{9/2} \rightarrow ^4I_{15/2}$ transitions of erbium, respectively [5–6]. Red emission was found to have a greater relative increase in intensity than green emission when the concentrations of Er – Yb were varied. This might be because only a small number of Er^{3+} ions emit green light at the $^2H_{11/2}$ and $^4S_{3/2}$ levels, while more Er^{3+} ions remain at the red emission level of $^4F_{9/2}$ [7].

Changing the concentration of the sensitizer (Yb^{3+}) from 10 to 30 mol% while holding the activator (Er^{3+}) at 2 mol% as shown in figure 5.1 (b) allowed for an analysis of the influence of concentration on the UCL and energy transfer mechanism in the Yb^{3+} - Er^{3+} co-doped $NaYF_4$ nanocrystals. Increasing the Yb^{3+} concentration from 10% to 20% in figure 5.1 (b) resulted in a greater luminescence intensity, indicating efficient energy transfer from Yb^{3+} to Er^{3+} ions; however, increasing the concentration to 30% resulted in a lesser luminescence intensity, illustrating the concentration quenching effect. The concentration quenching effect that occurred when Yb^{3+} was increased to 30% might be due to the fact that an increase in the doping concentration of ions in nanocrystals results in a greater number of photon sensitizers and emitters, a shorter distance between the activator and the sensitizer, and an overall brighter emission.

However, as was observed when the concentration of Yb^{3+} was raised to 30%, concentration quenching dominates with great amounts of dopants. As a result, this can diminish the effectiveness of the sequential transfer of energy. As a consequence of this, the proper doping concentration management in the particular host governs their ability to leverage the transfer of energy process and, ultimately, their luminescence effectiveness [8].

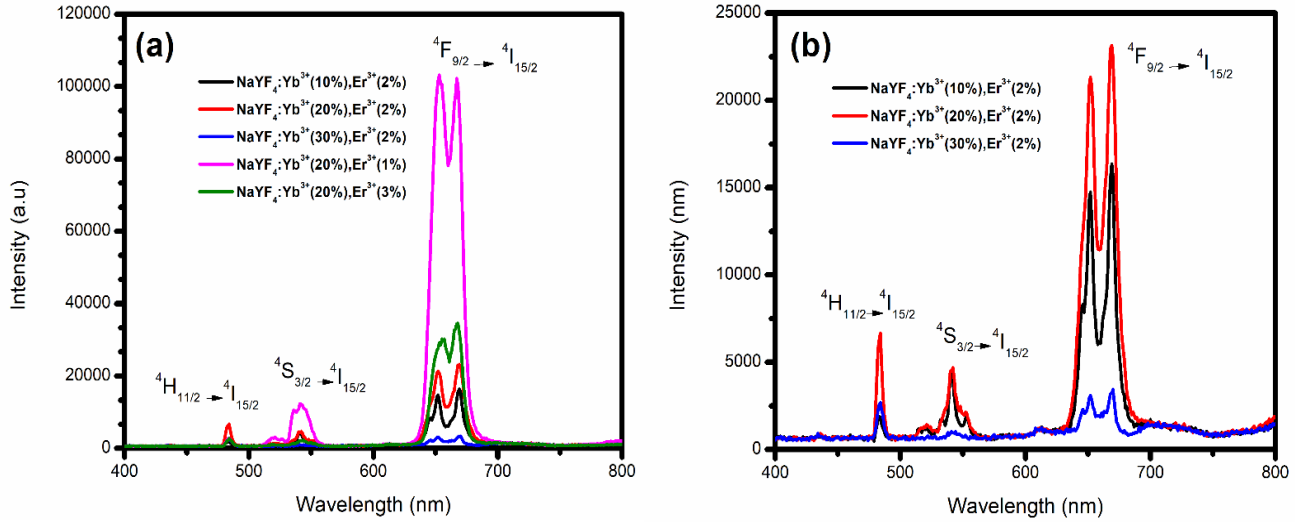


Figure 5.1. (a) Upconversion emission spectra of Yb³⁺-Er³⁺ co-doped NaYF₄ nanocrystals when excited by 980 nm laser beam (b) Upconversion emission spectra while varying concentrations of the sensitizer Yb³⁺.

To investigate how temperature affects the UCL of NaYF₄, the UPL for unannealed, 600 °C annealed, and 700 °C annealed NaYF₄: x% Yb³⁺, 2% Er³⁺ (x = 10, 20, and 30%) samples was plotted together and their intensities were compared (See Figure 5.2(a-c)). The annealing of the nanocrystals enhanced the UCL. From these results, we observe that increasing concentrations of Yb³⁺ increase the luminescent intensity of the nanocrystals, but increasing the concentration above the concentration threshold reduces the UPL intensity of the nanocrystals due to concentration quenching as indicated by figure 5(b), whereas increasing the annealing temperature enhances the PL intensity of the nanocrystals (see figure 5.2 below). Therefore, by carefully adjusting the annealing temperature and doping concentrations, the effectiveness of the photoluminescent materials can be improved.

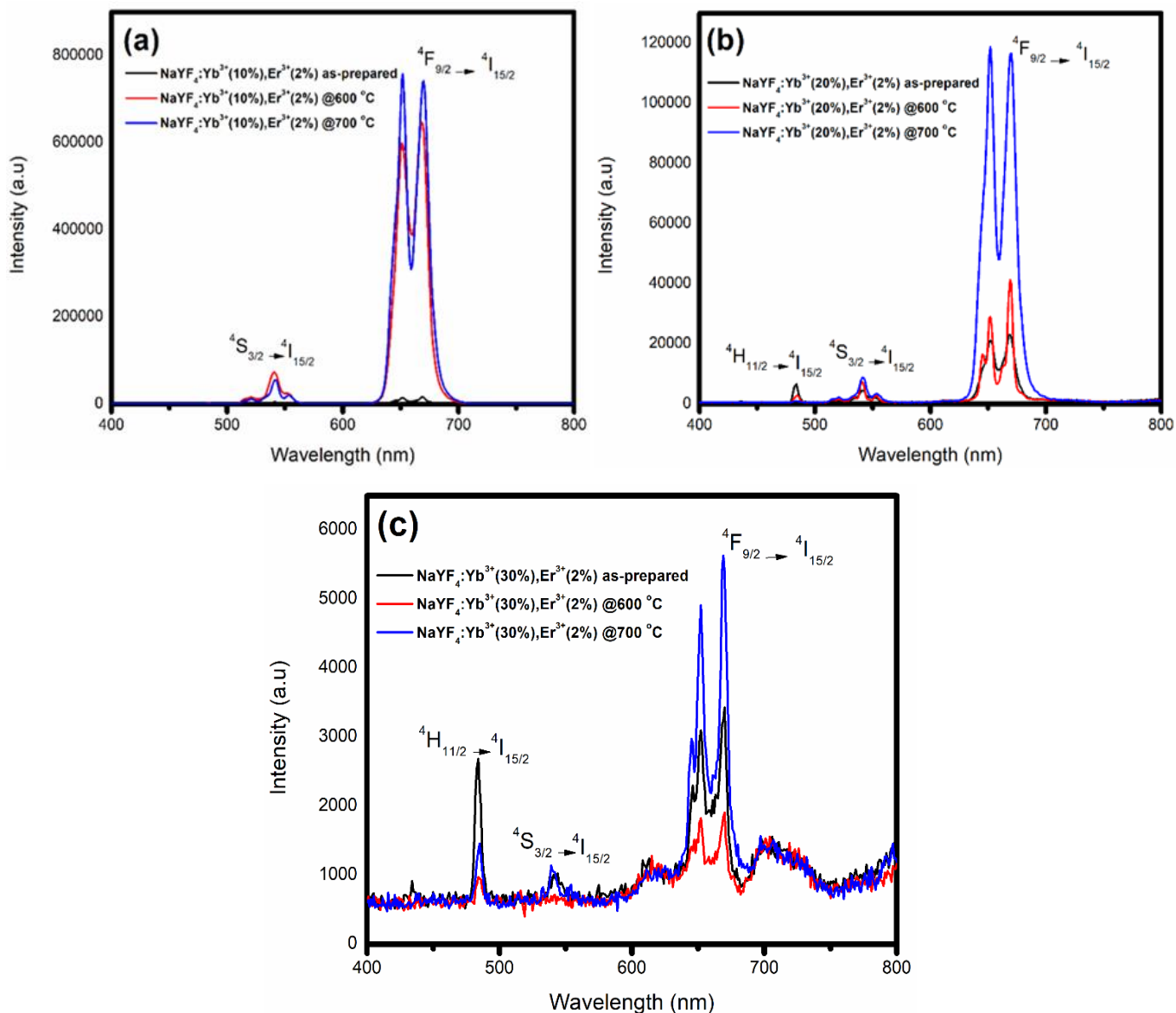


Figure 5.2. Up-conversion PL spectra of (a) $\text{NaYF}_4:10\%\text{Yb}^{3+},2\%\text{Er}^{3+}$, (b) $\text{NaYF}_4:20\%\text{Yb}^{3+},2\%\text{Er}^{3+}$ and (c) $\text{NaYF}_4:30\%\text{Yb}^{3+},2\%\text{Er}^{3+}$, showing how the annealing temperature affects the luminescence intensity.

Figure 5.3 illustrates the UPL emission spectra of the NaGdF_4 nanocrystals in their as-prepared state, doped with varying concentrations of Yb^{3+} (10–30 mol%) and Nd^{3+} (1–3 mol%) in the wavelength range of 400–900 nm under the excitation wavelength of 980 nm. As shown in Figure 5.3(a-b), all samples revealed the same pattern. Excited by light at 980 nm, all $\text{Yb}^{3+}\text{-Nd}^{3+}$ co-doped NaGdF_4 samples showed six significant sensitized upconversion bands centered at 485, 542, 620, 660, 709, and 830 nm, which correspond

to the transitions of Nd^{3+} ions: $^4\text{D}_{3/2} \rightarrow ^4\text{I}_{15/2}$, $^4\text{G}_{7/2} \rightarrow ^4\text{I}_{9/2}$, $^4\text{G}_{7/2} \rightarrow ^4\text{I}_{11/2}$, $^4\text{G}_{7/2} \rightarrow ^4\text{I}_{15/2}$, $^2\text{P}_{3/2} \rightarrow ^4\text{F}_{5/2}$, and $^4\text{F}_{3/2} \rightarrow ^4\text{I}_{9/2}$ respectively [9]. Several investigations have demonstrated that activator and sensitizer dopant concentrations significantly impact UPL [10]. To study the effects of Yb^{3+} on the UPL spectra of the NaGdF_4 , Yb^{3+} was changed from 10% to 30% while Nd^{3+} was held constant at 2%. The luminescence intensity of the nanocrystals decreased when Yb^{3+} was increased from 10% to 20% but increased when the concentration was increased to 30%. The observed luminescent intensity decrease demonstrates the concentration quenching effect [8]. This may be due to the fact that surpassing the concentration threshold makes the sequential transfer of energy process less effective [11].

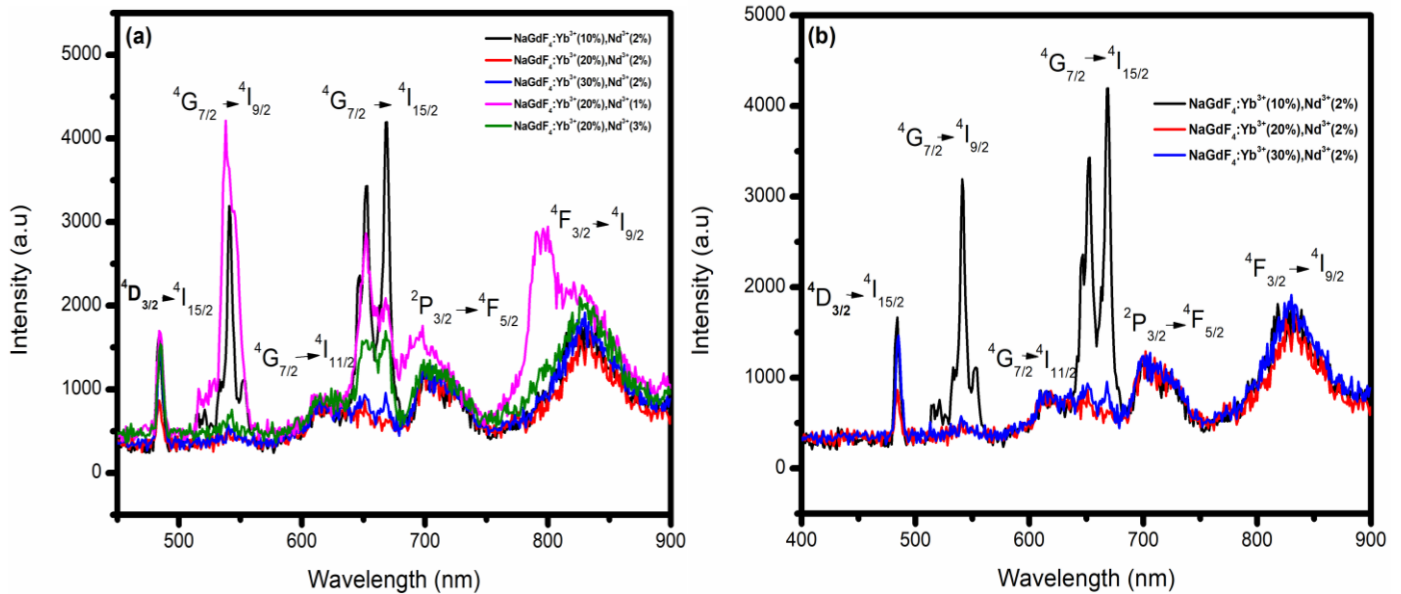


Figure 5.3. (a) The spectra of upconversion emission from $\text{Yb}^{3+}\text{-Nd}^{3+}$ co-doped NaGdF_4 nanocrystals excited by a 980 nm laser beam (b) Changing the amount of Nd^{3+} .

To examine how temperature affects the UCL of NaGdF_4 , the UPL for unannealed, annealed at 600, and 700 °C NaGdF_4 : x% Yb^{3+} , 2% Nd^{3+} (x = 10, 20, and 30%) samples were plotted together and their intensities were compared (See Figure 5.4(a-c)). The UPL intensity increased with an increase in the annealing temperatures for the NaGdF_4 :10% Yb^{3+} ,2% Nd^{3+} and NaGdF_4 :20% Yb^{3+} ,2% Nd^{3+} nanocrystals, and for the NaGdF_4 :30% Yb^{3+} , 2% Nd^{3+} , the UPL intensity decreased when the nanocrystals were

annealed. From these, it was observed that the annealing of the nanocrystals enhanced the UCL of the $\text{NaGdF}_4:10\%\text{Yb}^{3+},2\%\text{Nd}^{3+}$ and the $\text{NaGdF}_4:20\%\text{Yb}^{3+}, 2\%\text{Nd}^{3+}$ but decreased the UPL for the $\text{NaGdF}_4:30\%\text{Yb}^{3+}\text{-Nd}^{3+}$. This might be because increasing the annealing temperatures for samples that are highly doped and showing concentration quenching does not improve the luminescence intensity.

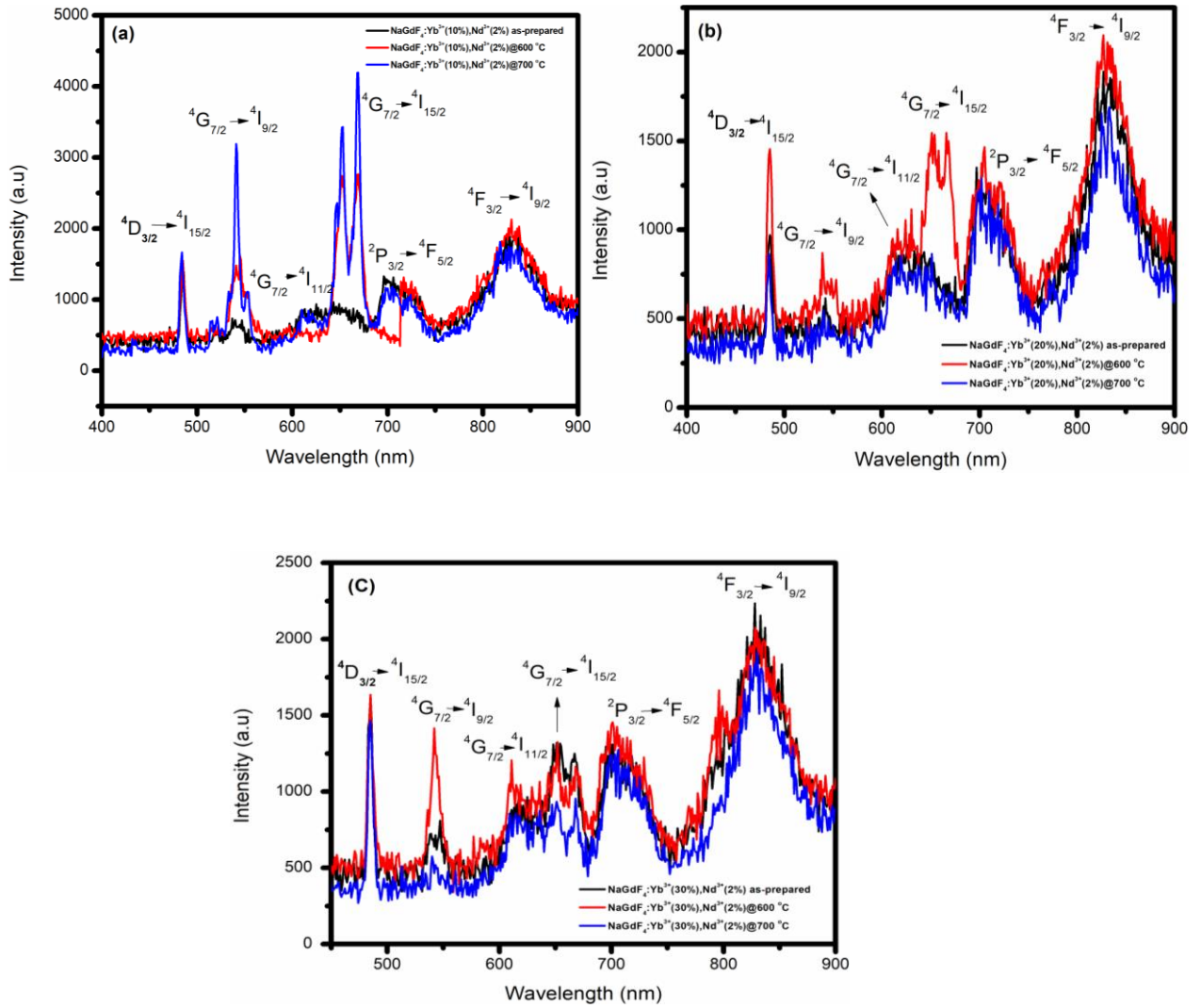


Figure 5.4. Up-conversion PL spectra of (a) $\text{NaGdF}_4:10\%\text{Yb}^{3+},2\%\text{Nd}^{3+}$, (b) $\text{NaGdF}_4:20\%\text{Yb}^{3+},2\%\text{Nd}^{3+}$, (c) $\text{NaGdF}_4:30\%\text{Yb}^{3+},2\%\text{Nd}^{3+}$, showing the effects of temperature in the luminescent intensity of the nanocrystals.

5.2.2 Proposed energy-transfer mechanism

Figure 5.5 displays the energy levels of the Yb^{3+} and Er^{3+} ions as well as the transfer of energy processes during stimulation at 980 nm. The prepared samples are all showing ETU. The ETU is a UPL by Yb^{3+} - Er^{3+} in which a low-phonon-energy host is needed to prevent the first excited state (the $\text{Er}^{3+} {}^4\text{I}_{11/2}$ level) from rapidly relaxing without emitting radiation. The low phonon energy of NaYF_4 accounts for the presence of UPL in these samples [12]. Due to their equal (+3) charge, Yb^{3+} and Er^{3+} ions doped in the NaYF_4 host lattice will replace the Y^{3+} site in the $\text{NaYF}_4\text{:Yb,Er}$ mixture. The absorbing of two photons one after the other in this combination is the foundation of the optical process. As a sensitizer, the Yb^{3+} ion absorbs and transfers NIR photon energy to the Er^{3+} ion in two stages, the excited and intermediate states, respectively. The Er^{3+} ion then experiences multiphonon relaxations that shift its highly excited states into less excited ones, producing radiative emission in the visible spectrum between 500 and 700 nm [5].

Under 980 nm excitation, the Yb^{3+} ion can be raised from its ground state to the ${}^2\text{F}_{5/2}$ level by the absorption of the first photon, which subsequently transfers the energy to the Er^{3+} ion. In the event that the ${}^4\text{I}_{11/2}$ level is already occupied, this transfer of energy can promote the Er^{3+} ion from the ${}^4\text{I}_{15/2}$ level to the ${}^4\text{I}_{11/2}$ level, and from the ${}^4\text{I}_{11/2}$ level to the ${}^4\text{F}_{7/2}$ level via a different ETU process (or a second 980 nm photon). Green emissions are produced when the Er^{3+} ion relaxes nonradiatively to the ${}^2\text{H}_{9/2}$, ${}^2\text{H}_{11/2}$, and ${}^4\text{S}_{3/2}$ levels (${}^2\text{H}_{11/2} \rightarrow {}^4\text{I}_{15/2}$ and ${}^4\text{S}_{3/2} \rightarrow {}^4\text{I}_{15/2}$). If, on the other hand, the ion relaxes even more and occupies the ${}^4\text{F}_{9/2}$ level, red emission (${}^4\text{F}_{9/2} \rightarrow {}^4\text{I}_{15/2}$) results [13].

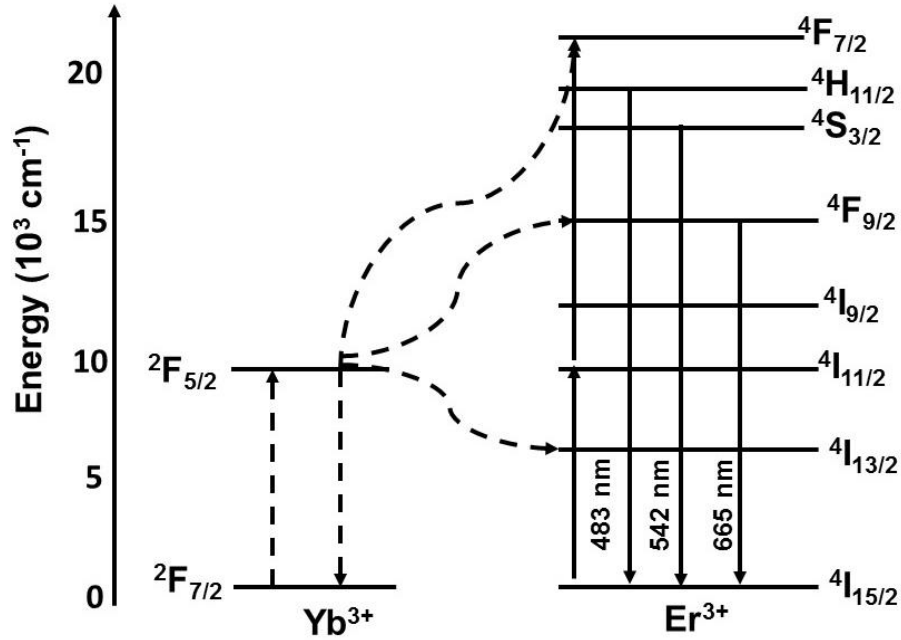


Figure 5.5: Mechanism of Yb³⁺ to Er³⁺ energy transfer under stimulation at 980 nm.

Figure 5.6 displays the Yb³⁺ and Nd³⁺ energies as well as the energy transfer processes under excitation at 980 nm. The ETU is present in all the prepared samples. A low-phonon-energy host is needed for the ETU, a UPL by Yb³⁺-Nd³⁺, to prevent the rapid non-radiative relaxation of the first excited state (the Nd³⁺ → ⁴D_{3/2} level). The occurrence of UPL in these samples is explained by the low phonon energy of NaGdF₄ [10]. Yb³⁺ and Nd³⁺ ions doped in the NaGdF₄ host lattice will replace the Gd³⁺ site in the NaGdF₄:Yb³⁺,Nd³⁺ combination due to their equal (+3) charge. The sequential absorption of two photons in this combination is the foundation of the optical process. As a sensitizer, the Yb³⁺ ion absorbs and transfers NIR photon energy to the Nd³⁺ ion in two stages, called the excited and intermediate states, respectively. After then, multiphonon relaxations convert the Nd³⁺ ion's highly excited states to lower excited states, causing radiative emission in the 500–700 nm visible spectrum [5]. Under 980 nm excitation, the first photon's absorption can raise the Yb³⁺ ion from its ground state to the ²F_{5/2} level and subsequently transfer the energy to the Nd³⁺ ion. This energy transfer can promote Nd³⁺ ions from the ⁴I_{15/2} level to the ⁴I_{11/2} level and from the ⁴I_{11/2} level to the ⁴F_{7/2} level via

another ETU process (or a second 980 nm photon) if the $^4D_{3/2}$ level is already occupied. Green emissions ($^4D_{3/2} \rightarrow ^4I_{15/2}$, $^4G_{7/2} \rightarrow ^4I_{9/2}$, $^4G_{7/2} \rightarrow ^4I_{11/2}$, and $^4G_{7/2} \rightarrow ^4I_{15/2}$) originate from the Nd^{3+} ions relaxing nonradiatively to the $^4G_{7/2}$ levels. If the ion relaxes any further, it can occupy the $^2P_{3/2}$ and $^4F_{3/2}$ levels and emit red light ($^2P_{3/2} \rightarrow ^4F_{5/2}$, and $^4F_{3/2} \rightarrow ^4I_{9/2}$) [13].

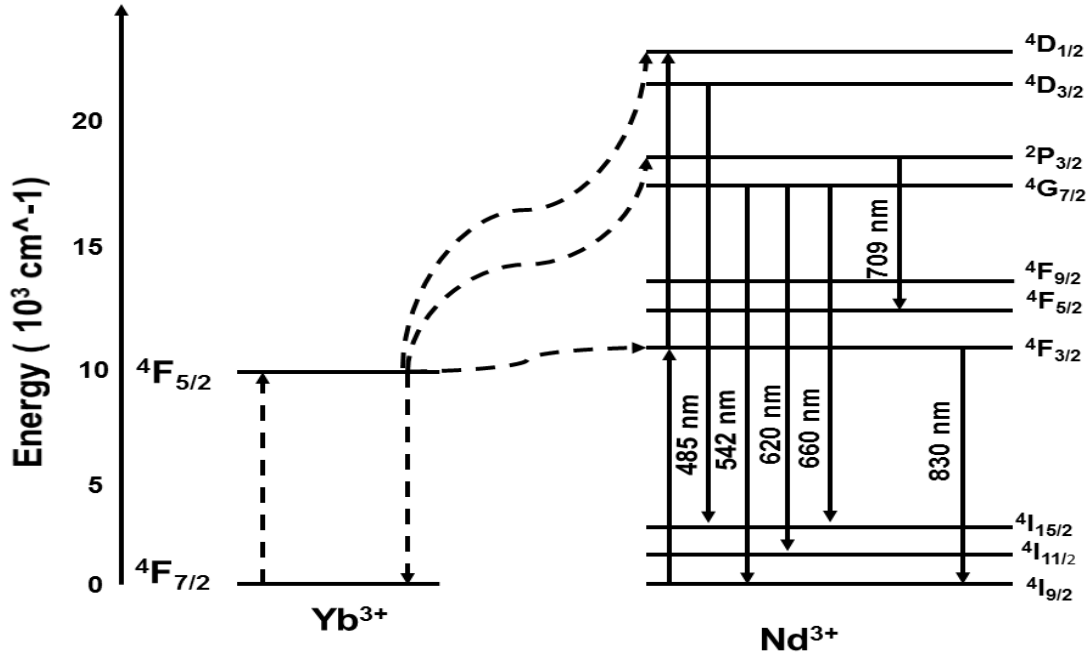


Figure 5.6: Mechanism of Yb^{3+} to Nd^{3+} energy transfer under stimulation at 980 nm.

5.2.4 UV-Vis-NIR analysis

Figure 5.7 depicts the UV-Vis absorption spectra of undoped $NaYF_4$ and Yb^{3+} - Er^{3+} co-doped nanocrystals. The absorption peak occurs in the 250–1800 nm wavelength range. The nanocrystals exhibit six characteristics peaks of Er^{3+} at ~487, 520, 654, 802, 972 and 1526 nm corresponding to electron transitions of $^4I_{15/2} \rightarrow ^4F_{7/2}$ (~ 487 nm), $^4I_{15/2} \rightarrow ^4H_{11/2}$ (~ 520 nm), $^4I_{15/2} \rightarrow ^2F_{9/2}$ (~ 654 nm), $^4I_{15/2} \rightarrow ^4I_{9/2}$ (~ 802 nm), and $^4I_{15/2} \rightarrow ^4I_{13/2}$ (~ 1500 nm), respectively [14]. The absorption peak in the NIR wavelength range (972 nm) corresponds to the intense $^2F_{7/2}$ absorption band of Yb^{3+} , which overlaps with the $^4I_{11/2}$ absorption transition of Er^{3+} [15].

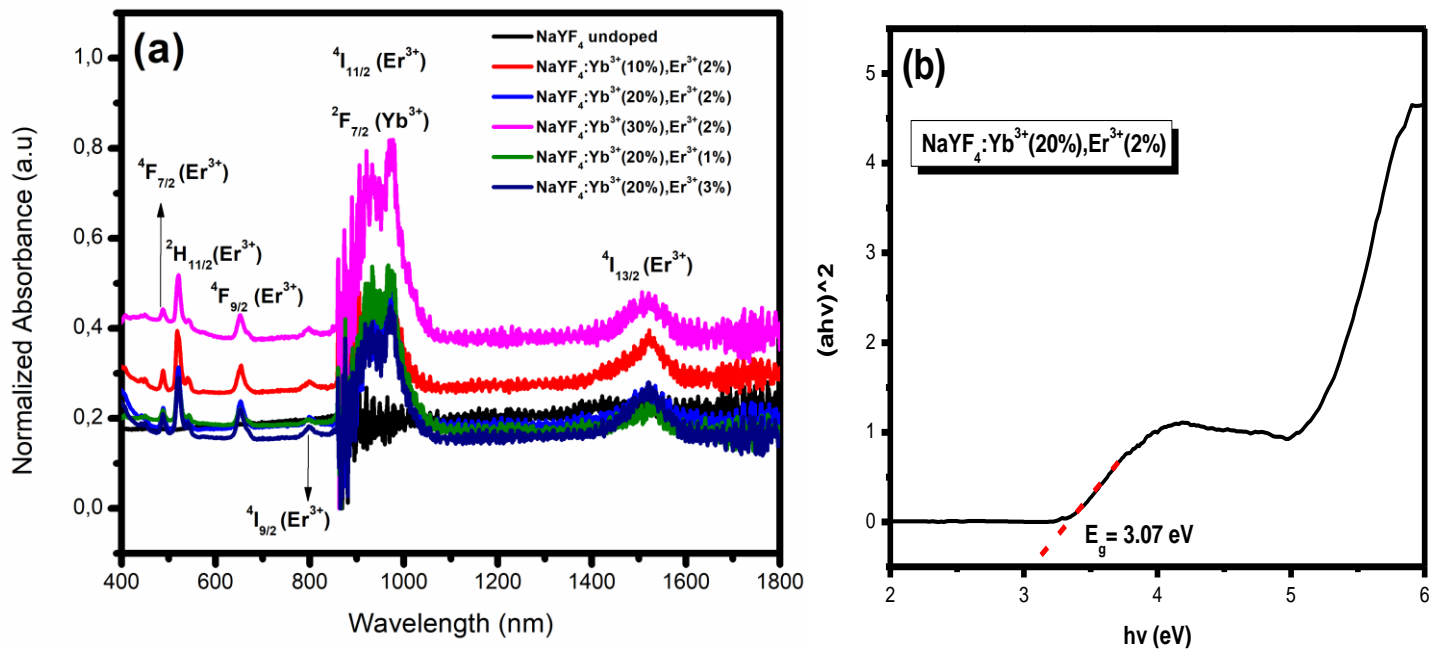


Figure 5.7. Absorption spectra of (a) Yb³⁺-Er³⁺ co-doped NaYF₄ nanocrystals and (b) direct bandgap evaluation using Tauc plot.

The spectra of the UV-Vis absorption of the undoped NaGdF₄ and Yb³⁺-Nd³⁺ co-doped NaGdF₄ nanocrystals in the wavelength range 250 to 850 nm are shown in Figure 5.8 below. The nanocrystals displayed five absorption peaks of Nd³⁺ at ~ 295, 510, 573, 740, and 796 nm assigned to the band-to-band transitions of NaGdF₄, ⁴I_{15/2} → ⁴F_{7/2} (~510 nm), ⁴I_{15/2} → ⁴S_{5/2} (~573 nm), ⁴I_{15/2} → ⁴F_{9/2} (~740 nm), and ⁴I_{15/2} → ⁴I_{9/2} (~796 nm), respectively [16]. Broad absorption in the visible region extending towards the NIR region was observed for all the doped samples. This means that these nanocrystals will make it possible for the PSCs to absorb light in the NIR range.

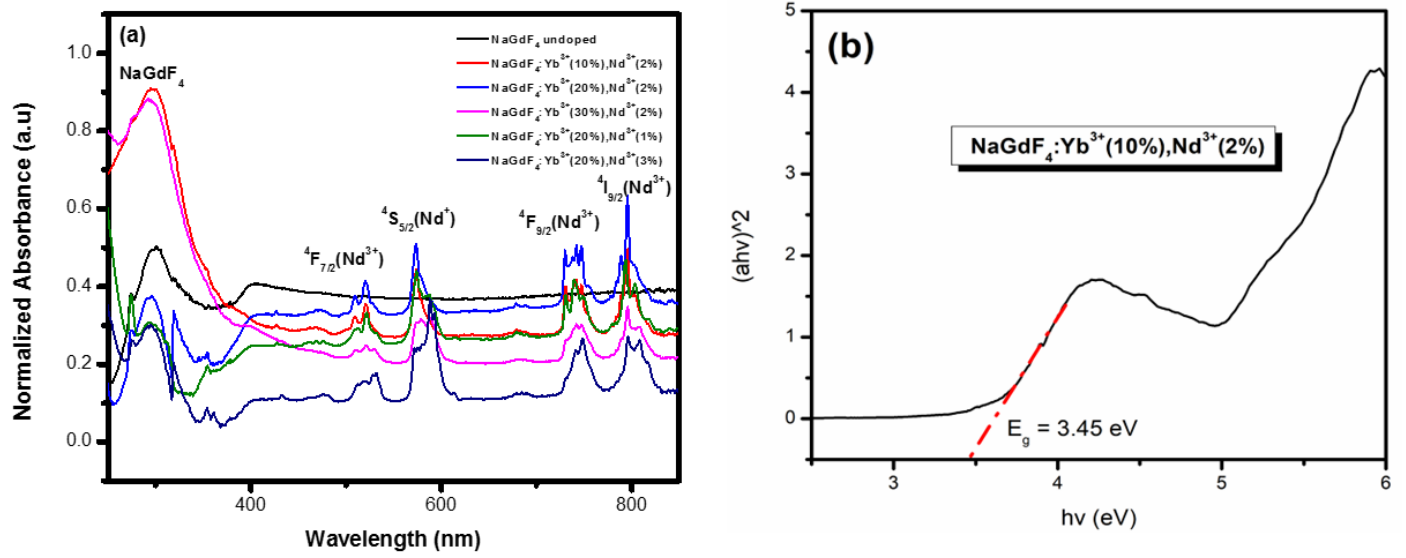


Figure 5.8. Absorption spectra of (a) Yb³⁺-Nd³⁺ co-doped NaGdF₄ nanocrystals and (b) direct bandgap evaluation using Tauc plot.

The absorption spectra illustrate that Er³⁺ and Yb³⁺ are well embedded into the lattice structure of NaYF₄, and Yb³⁺ and Nd³⁺ are also well incorporated into the host lattice of NaGdF₄ [17–19]. When the dopant concentrations were changed, a peak shift towards the higher wavelength was seen to be taking place. This might be because of the growth in the crystallite sizes of the nanocrystals. The absorption peak wavelengths are shifted toward the long wavelength range, and the absorption peaks are often greater in larger conjugated systems [17].

The optical bandgap values were determined for both the undoped, and doped materials based on optical spectrum absorption using the Kubelka-Munk equation provided by equation 5.1 [20]:

$$F(R) = \frac{\alpha}{s} = \frac{(1-R)^2}{2R} \quad (5.1)$$

Where $\alpha = (1-R)$ is the molar absorption coefficient, s is the scattering factor, and R is the reflectance of materials. For the direct allowed transitions using the Tauc plot, the bandgap energy can be obtained by extrapolating the slope of the Tauc plot to $(ahv)^2 = 0$ [21].

$$(\alpha h\nu)^2 = A (h\nu - E_g)$$

5.2

where $F(R)$ is proportional to α since s is only slightly dependent on the wavelength [20], A is the proportionality constant, $h\nu$ is the energy of a photon, and E_g is the direct bandgap. As shown in figures 5.7(b) and 5.8(b), the band gap of the samples was found by plotting $(h\nu)^2$ as a function of photon energy and extrapolating the linear part of the curve to absorption equal to zero [21].

The band gap of the nanocrystals changed as the amount of dopants changed. This could be because the ratio of the number of states to the amount of energy depends on the chemical composition of the material. If the chemical composition changes, at the very least, the ratio of the number of states to the amount of energy should also change. Doping changes the chemical make-up because dopants are impurities. There can't be a rule that says the bandgap will get smaller when impurities are added to the way the energy of the allowed states is spread out. Dopants are commonly referred to as impurities that allow shallow states in the bandgap. When there is a lot of doping, the shallow levels have low ionization energies, which makes the dopant states form a band. If this band is close to the edge of the valence or conduction band, the bandgap will get smaller. [22-23]. Since the Fermi level's shift to the conduction band has taken up some of the lowest states in the conduction band, the band gap has grown. This makes it harder to move from the valence band to the conduction band [24, 25]. The bandgap gets bigger as the size of the nanocrystals' crystallites gets smaller [26, 27]. The results of this study also showed that this is true. Through annealing, the optical band gaps of the nanocrystals were made smaller. This shows that the conductivity goes up directly in line with the temperature of annealing [28]. This gives the nanocrystals a better chance of being used as the electron transport layer in photovoltaic solar cells, where they can absorb low-energy NIR photons and turn them into high-energy visible light that PV materials can absorb to make more photocurrent. Figures 5.7(b) and 5.8(b) show how the optical bandgaps of all nanocrystals were estimated, and Tables 5.1 and 5.2 show approximated band gap and absorption edge wavelengths for both undoped and doped nanocrystals.

Table 5.1. Estimated absorption edge wavelength and band gap for undoped and doped NaYF₄ nanocrystals.

Sample name	Absorbance wavelength (nm)	Estimated bandgap (eV)
As-prepared samples		
NaYF ₄ :10%Yb ³⁺ ,2%Er ³⁺	517	3.84
NaYF ₄ :20%Yb ³⁺ ,2%Er ³⁺	521	3.81
NaYF ₄ :30%Yb ³⁺ ,2%Er ³⁺	524	3.79
NaYF ₄ :20%Yb ³⁺ ,1%Er ³⁺	535	3.71
NaYF ₄ :20%Yb ³⁺ ,3%Er ³⁺	519	3.82
Annealed @ 600°C		
NaYF ₄ :10%Yb ³⁺ ,2%Er ³⁺	541	3.67
NaYF ₄ :20%Yb ³⁺ ,2%Er ³⁺	537	3.69
NaYF ₄ :30%Yb ³⁺ ,2%Er ³⁺	541	3.76
Annealed @ 700°C		
NaYF ₄ :10%Yb ³⁺ ,2%Er ³⁺	538	3.69
NaYF ₄ :20%Yb ³⁺ ,2%Er ³⁺	550	3.61
NaYF ₄ :30%Yb ³⁺ ,2%Er ³⁺	546	3.63

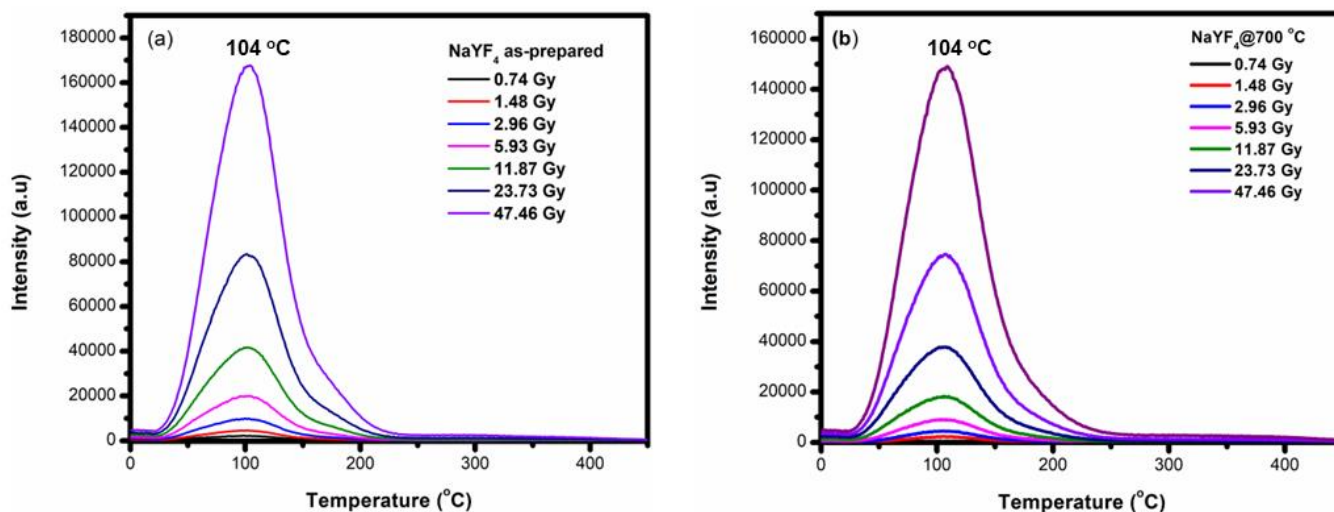
Table 5.2. Estimated absorption edge wavelength and band gap for undoped and doped NaGdF₄ nanocrystals.

Sample name	Absorbance wavelength (nm)	Estimated bandgap (eV)
As-prepared samples		
NaGdF ₄ :10%Yb ³⁺ ,2%Nd ³⁺	574	3.45
NaGdF ₄ :20%Yb ³⁺ ,2%Nd ³⁺	573	3.46
NaGdF ₄ :30%Yb ³⁺ ,2%Nd ³⁺	578	3.43
NaGdF ₄ :20%Yb ³⁺ ,1%Nd ³⁺	576	3.44
NaGdF ₄ :20%Yb ³⁺ ,3%Nd ³⁺	588	3.37
Annealed @ 600°C		
NaGdF ₄ :10%Yb ³⁺ ,2%Nd ³⁺	586	3.38

NaGdF₄:20%Yb³⁺,2%Er³⁺	582	3.41
NaGdF₄:30%Yb³⁺,2%Er³⁺	591	3.36
Annealed @ 700°C		
NaGdF₄:10%Yb³⁺,2%Nd³⁺	594	3.34
NaGdF₄:20%Yb³⁺,2%Nd³⁺	597	3.32
NaGdF₄:30%Yb³⁺,2%Nd³⁺	599	3.31

5.2.5 Thermoluminescence analysis

Figure 5.9(a-d) below shows the TL glow curves of the NaYF₄ and NaYF₄:20%Yb³⁺,2%Er³⁺ as-prepared and annealed at 700 °C, respectively. The glow curves were recorded when the samples were exposed to gamma rays with doses ranging from 0.74 to 47.46 Gy and a heating rate of 1 °C/s. The glow peaks were seen at 104 °C for the undoped samples, 73 °C, 154 °C, 238 °C, 374 °C for the NaYF₄:20%Yb³⁺,2%Er³⁺, 61 °C, 152 °C, and 342 °C for the NaYF₄:20%Yb³⁺,2%Er³⁺ annealed at 700 °C with the intensity increasing as the irradiation source dose increased.



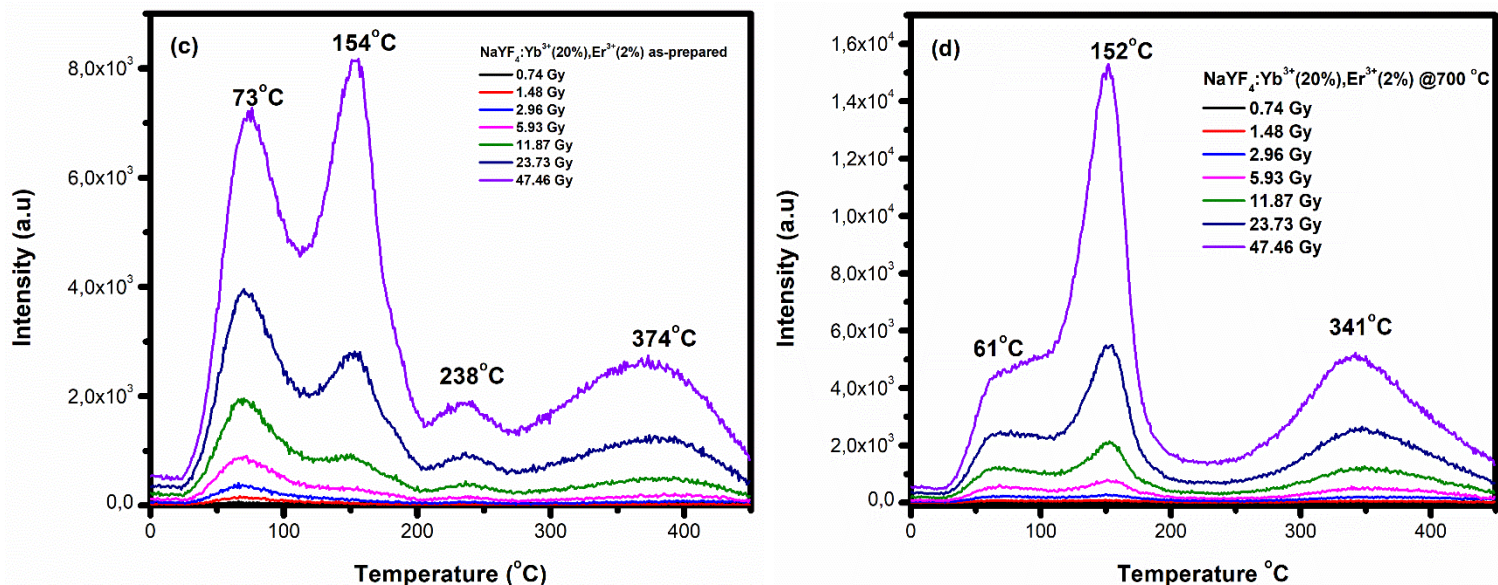


Figure 5.9: TL glow curves of (a) NaYF₄ as-prepared, (b) NaYF₄ annealed @700 °C, (c) NaYF₄:20%Yb³⁺,2%Er³⁺ as-prepared, (d) NaYF₄:20%Yb³⁺,2%Er³⁺ annealed @700 °C.

Figure 5.10(a-d) below shows the TL glow curves of the NaGdF₄ and NaGdF₄:20%Yb³⁺,2%Nd³⁺ as-prepared and annealed at 700 °C, respectively. The glow curves were recorded when the samples were exposed to gamma rays with doses ranging from 0.74 to 47.46 Gy and a heating rate of 1 °C/s. The glow peaks were seen at 106 and 164 °C for the NaGdF₄ as-prepared, 71 °C, 106 °C, and 390 °C for the NaGdF₄ annealed at 700 °C, 68 °C, 129 °C, and 387 °C for the NaGdF₄:20%Yb³⁺,2%Nd³⁺, 69 °C, 179°C, 141 °C, and 380 °C for the NaGdF₄:20%Yb³⁺,2%Nd³⁺ annealed at 700 °C with the intensity increasing as the irradiation source dose increased.

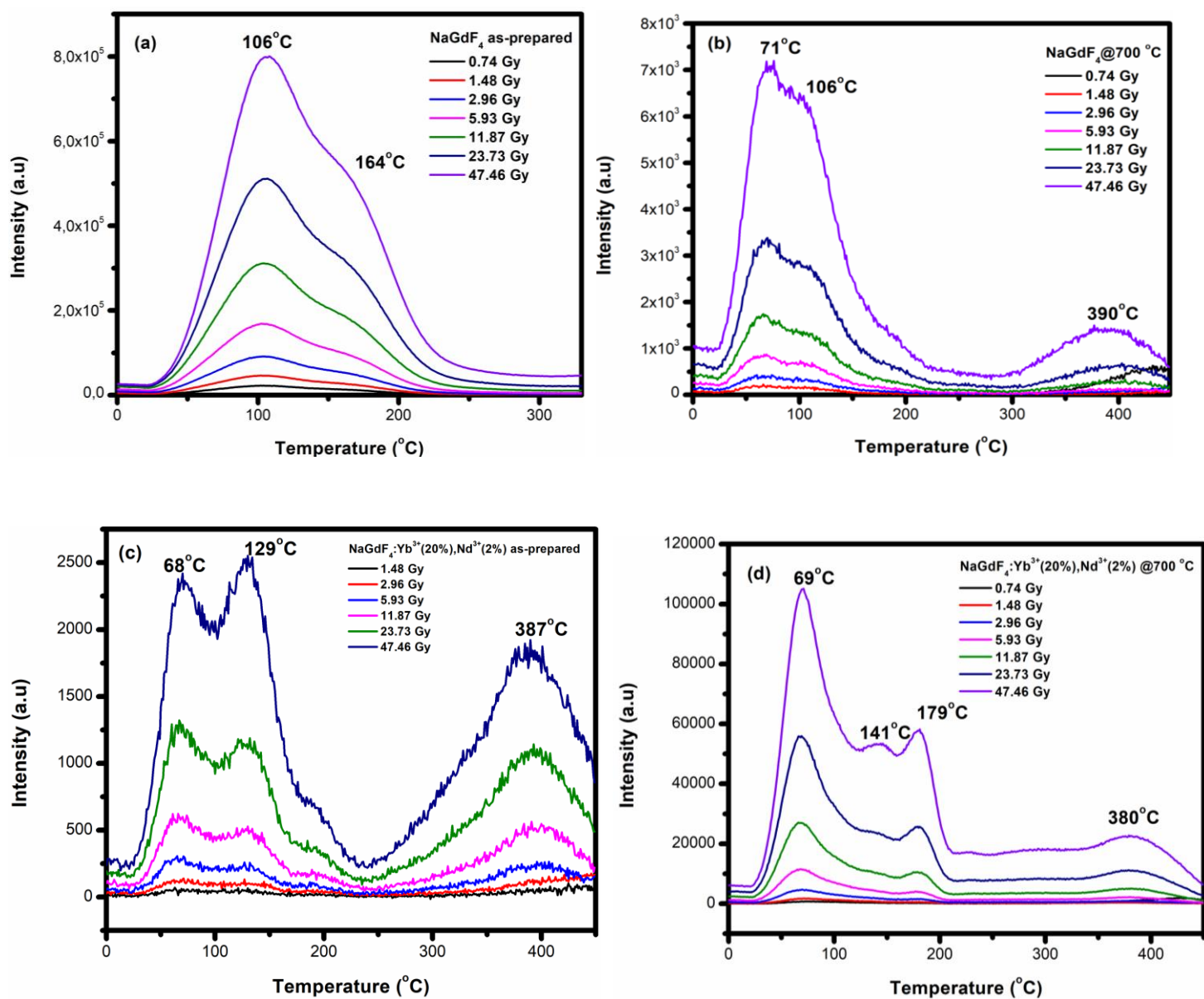


Figure 5.10: TL glow curves of (a) NaGdF₄ as-prepared, (b) NaGdF₄ annealed @700 °C, (c) NaGdF₄:20%Yb³⁺,2%Nd³⁺ as-prepared, (d) NaGdF₄:20%Yb³⁺,2%Nd³⁺ annealed @700 °C.

Figures 5.9 and 5.10 clearly shows that doping and annealing the nanocrystals have huge effects in the TL glow curves. For the undoped NaYF₄ samples, no peak shift was observed when the sample was annealed, indicating that the systems operate on first-order kinetics [29]. For the doped samples, peak shifts towards lower and higher temperatures were observed when the as-prepared samples were annealed. This could be due to cluster formation after annealing the sample. Variations in trapping and recombination kinetics result from the formation of trap clusters as opposed to randomly distributed defects. The elimination and introduction of defects that resulted from annealing may also contribute to the peak shift [30]. The presence of various trapping levels, which can be categorized as shallow trapping, intermediate trapping, or deep trapping, is evidenced by the appearance of new glow peaks in the higher temperature region after host doping [31]. Furthermore, the increase in intensity with dose suggests that more of the traps responsible for the glow peaks were filled, resulting in the release of charge carriers upon heat stimulation [29]. The appearance and disappearance of peaks and increase in the peak intensities when the nanocrystals are annealed may be attributed to the re-arrangement of the available electronic energy levels. This may change due to the phase transformation or the change in the size of the particles [30]. It is worth mentioning that annealed NaYF₄:20%Yb³⁺,2%Er³⁺ and NaGdF₄:20%Yb³⁺,2%Nd³⁺ are proper candidates of TL dosimetry applications.

To calculate the activation energy of trapped electrons, the initial rise (IR) technique was applied to the samples' glow curves after being exposed to 47.4 Gy of beta particle irradiation (see Figure 5.11 for an example). The Garlick-Gibson equation (Equation (5.2)) is used in the IR method. This method does not rely on any sort of kinetic order for the low temperature regions of the glow curve, as shown in Figure 5.11(a-b).

$$I(t) \propto e^{-E/kT} \quad (5.2)$$

where E and k stand for the electrons' activation energy and the Boltzmann constant [5]. Because electron traps are disrupted at low temperatures, this method makes use of those regions' glow peaks. The points were measured between 5 and 15% (*I_c*) of the glow curve's maximum intensity (*I_{MAX}*) [6]. Because above a critical temperature *T_c*, the assumption of a constant number of trapped electrons becomes erroneous, the rule of

thumb states that the initial rise portion chosen should not exceed 10–15% of the peak intensity [8]. The slopes of the fit lines in the initial rise method plots (Fig. 5.11(a) and (b)) [10] give the activation energy of the electrons from the electron trapping centers. Tables 5.3 and 5.4 show the estimated activation energies for the samples from the IR method, and Figure 5.11 shows how the activation energy for all the samples was estimated using this technique.

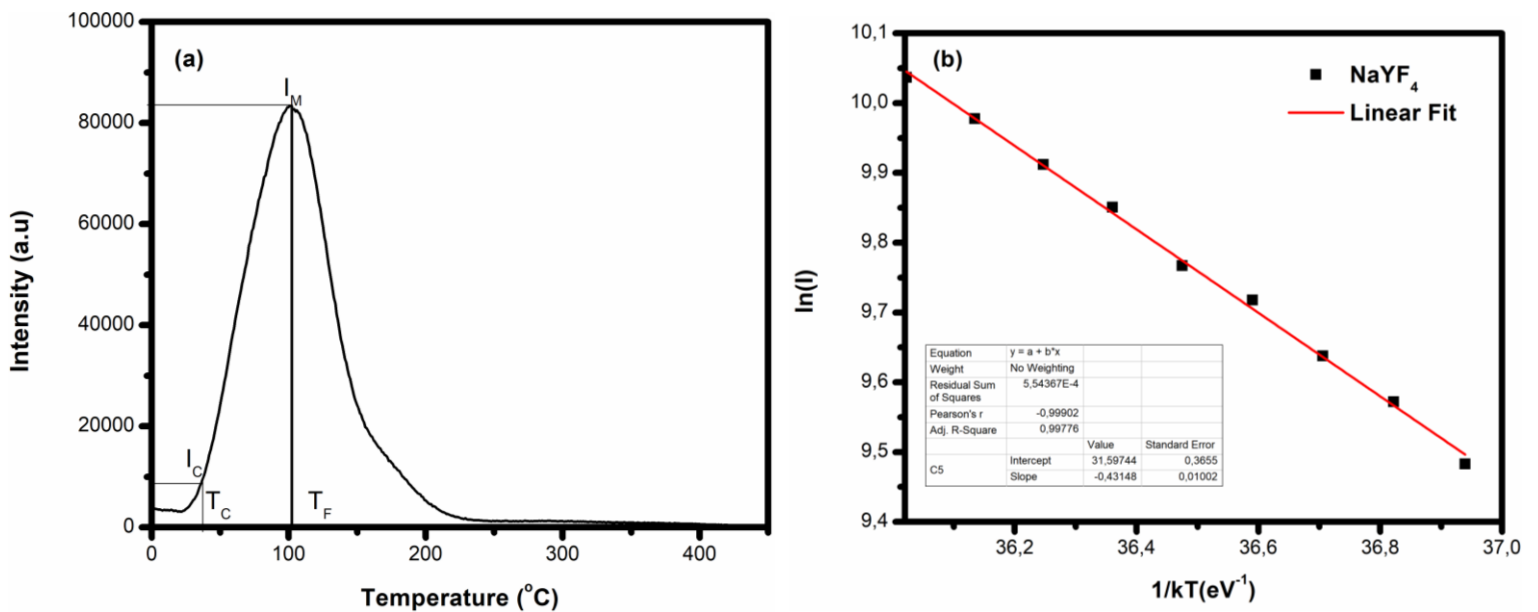


Figure 5.11. (a) a recording of the NaYF₄ glow curve at 23.7 Gy; (b) a linear fit of the NaYF₄ glow curve using the initial rise method

Table 5.3. Estimated activation energies for undoped and doped NaYF₄ nanocrystals.

Name of sample	Estimated activation energy (eV)
NaYF ₄	0.43±0.007
NaYF ₄ @700 °C	0.55±0.073
NaYF ₄ :20%Yb ³⁺ ,2%Er ³⁺	0.47±0.003
NaYF ₄ :20%Yb ³⁺ ,2%Er ³⁺ @700 °C	0.50±0.018

Table 5.4. Estimated activation energies for undoped and doped NaGdF₄ nanocrystals.

Name of sample	Estimated activation energy (eV)
NaGdF₄	0.56±0.011
NaGdF₄@700 °C	0.52±0.002
NaGdF₄:20%Yb³⁺,2%Nd³⁺	0.60±0.008
NaGdF₄:20%Yb³⁺,2%Nd³⁺@700 °C	0.59±0.016

Conclusion

The UPL analysis indicated the effective transfer of energy from Yb^{3+} to Er^{3+} in the NaYF_4 nanocrystals when the Yb^{3+} concentration was increased from 10 to 20% and showed concentration quenching when Yb^{3+} was increased to 30%. Two green and one red UC emissions centred at ~483, 542, and 665 nm attributed to $^2\text{H}_{11/2} \rightarrow ^4\text{I}_{15/2}$, $^4\text{S}_{3/2} \rightarrow ^4\text{I}_{15/2}$, and $^4\text{F}_{9/2} \rightarrow ^4\text{I}_{15/2}$ transitions of Er^{3+} , respectively, were observed under 980 nm laser excitation for all $\text{Yb}^{3+}\text{-Er}^{3+}$ co-doped NaYF_4 samples. Annealing the nanocrystals showed an improvement in the UCL intensities from UPL analysis. Also, energy transfer was observed in NaGdF_4 from Yb^{3+} to Nd^{3+} when Yb^{3+} concentration increased from 10 to 30% and showed concentration quenching when Yb^{3+} was at 20%. Under laser excitation at 980 nm, four green and two red UC emissions centred at 485, 542, 620, 660, 709, and 830 nm, respectively, were seen for all $\text{Yb}^{3+}\text{-Nd}^{3+}$ co-doped NaGdF_4 samples. These emissions were attributed to $^4\text{D}_{3/2} \rightarrow ^4\text{I}_{15/2}$, $^4\text{G}_{7/2} \rightarrow ^4\text{I}_{9/2}$, $^4\text{G}_{7/2} \rightarrow ^4\text{I}_{11/2}$, $^4\text{G}_{7/2} \rightarrow ^4\text{I}_{15/2}$, $^2\text{P}_{3/2} \rightarrow ^4\text{F}_{5/2}$, and $^4\text{F}_{3/2} \rightarrow ^4\text{I}_{9/2}$ transitions of Nd^{3+} , respectively. The synthesized nanocrystals showed upconverted emissions in the visible and NIR spectral ranges through the ETU mechanisms when excited by a 980 nm laser. These bands of emission correspond to the PSCs' absorption range. This means that the PSCs are well-suited to efficiently absorb these emissions and produce the photocurrent when stimulated by a 980-nm laser. The UV-Vis analysis of the NaYF_4 doped samples revealed that the nanocrystals exhibit six characteristics peaks centred at ~487, 520, 654, 802, 972, and 1526 nm ascribed to $^4\text{I}_{15/2} \rightarrow ^4\text{F}_{7/2}$ (~ 487 nm), $^4\text{I}_{15/2} \rightarrow ^4\text{H}_{11/2}$ (~ 520 nm), $^4\text{I}_{15/2} \rightarrow ^2\text{F}_{9/2}$ (~ 654 nm), $^4\text{I}_{15/2} \rightarrow ^4\text{I}_{9/2}$ (~ 802 nm), $^4\text{I}_{15/2} \rightarrow ^4\text{I}_{11/2}$ (~972) and $^4\text{I}_{15/2} \rightarrow ^4\text{I}_{13/2}$ (~ 1500 nm) transitions of Er^{3+} respectively. The absorption peak at ~972 nm attributed to the $^2\text{F}_{7/2}$ transition of Yb^{3+} overlaps with the $^4\text{I}_{11/2}$ absorption transition of Er^{3+} . Five absorption peaks assigned to Nd^{3+} were observed in the NaGdF_4 nanocrystals at ~295, 510, 573, 740, and 796 nm assigned to $^4\text{I}_{15/2} \rightarrow ^4\text{F}_{7/2}$ (~510 nm), $^4\text{I}_{15/2} \rightarrow ^4\text{S}_{5/2}$ (~573 nm), $^4\text{I}_{15/2} \rightarrow ^4\text{F}_{9/2}$ (~740 nm), $^4\text{I}_{15/2} \rightarrow ^4\text{I}_{9/2}$ (~796 nm), and band to band transitions of NaGdF_4 respectively. The band gaps of the nanocrystals decreased when the samples were annealed, indicating a rise in the conductivity of the nanocrystals with an increase in annealing temperature. These nanocrystals showed an absorption in the NIR, which makes them good candidates to

extend the absorption of the PSCs to the NIR region. The proposed energy transfer mechanism suggests an energy transfer from Yb^{3+} to Er^{3+} ions, and UPL confirmed this phenomenon. TL studies revealed that doping the hosts causes the appearance of new peaks, and annealing the samples leads to peak shifts either to lower or higher temperatures. We determined that the dominant electron kinetics from stimulated luminescence were of first order and used the IR method to calculate the depth of the corresponding electron trapping centres. The annealed $\text{NaYF}_4:20\%\text{Yb}^{3+},2\%\text{Er}^{3+}$ and $\text{NaGdF}_4:20\%\text{Yb}^{3+},2\%\text{Nd}^{3+}$ were found to be the proper candidates of TL dosimetry applications, whereas the peak located at 104 °C for the TL glow curve of NaYF_4 annealed at 700 °C and the one located at 106 °C for the TL glow curve of as-prepared NaGdF_4 , could be useful for *afterglow* (AG) or persistent luminescence dosimetry applications.

References

- [1]. Talane, T.E., 2017. *Study of Structural and Optical Properties of Undoped and Rare Earth Doped TiO₂ Nanostructures* (Doctoral dissertation).
- [2]. Kobus, H.J., Kirkbride, K.P. and Raymond, M.A., 2016. Identification: fingerprints a key identification parameter–detection, identification, and interpretation. In *Encyclopedia of Forensic and Legal Medicine: Second Edition* (pp. 65-73). Elsevier.
- [3]. Singh, D., Tanwar, V., Bhagwan, S. and Singh, I., 2016. Recent advancements in luminescent materials and their potential applications. *Adv. Magn. Opt. Mater.*, 317, p.14.
- [4]. Mbule, P.S., 2009. *Sol-gel synthesis of and luminescent properties of Pr³⁺ in different host matrices* (Doctoral dissertation, University of the Free State).
- [5]. Namagal, S., Jaya, N.V., Muralidharan, M. and Sumithra, S., 2020. Optical and magnetic properties of pure and Er, Yb-doped β -NaYF₄ hexagonal plates for biomedical applications. *Journal of Materials Science: Materials in Electronics*, 31(14), pp.11398-11410.
- [6]. Nagli, L., Gaft, M., Flegler, Y. and Rosenbluh, M., 2008. Absolute Raman cross-sections of some explosives: Trend to UV. *Optical Materials*, 30(11), pp.1747-1754.
- [7]. Yang, W., Wang, X., Leng, Z., Lin, H., Zeng, F., Li, C. and Su, Z., 2021. Er, Yb: CeF₃ red emission nanoparticles with controllable size and enhanced luminescence properties. *Journal of Materials Science: Materials in Electronics*, 32, pp.8213-8225.
- [8]. Wen, S., Zhou, J., Zheng, K., Bednarkiewicz, A., Liu, X. and Jin, D., 2018. Advances in highly doped upconversion nanoparticles. *Nature communications*, 9(1), pp.1-12.
- [9]. Tian, L., Xu, Z., Zhao, S., Cui, Y., Liang, Z., Zhang, J. and Xu, X., 2014. The upconversion luminescence of Er³⁺/Yb³⁺/Nd³⁺ triply-doped β -NaYF₄ nanocrystals under 808-nm excitation. *Materials*, 7(11), pp.7289-7303.
- [10]. Sun, C., Schäferling, M., Resch-Genger, U. and Gradzielski, M., 2021. Solvothermal synthesis of lanthanide-doped NaYF₄ upconversion crystals with size and shape control: particle properties and growth mechanism. *ChemNanoMat*, 7(2), pp.174-183.

- [11]. Alkahtani, M., Almuqhim, A.A., Qasem, H., Alsofyani, N., Alfahd, A., Alenzi, S.M., Aljuwayr, A., Alzahrani, Y.A., Al-Badri, A., Alotaibi, M.H. and Bagabas, A., 2021. Lithium-Based Upconversion Nanoparticles for High Performance Perovskite Solar Cells. *Nanomaterials*, 11(11), p.2909.
- [12]. Hakmeh, N., Chlique, C., Merdrignac-Conanec, O., Fan, B., Cheviré, F., Zhang, X., Fan, X. and Qiao, X., 2015. Combustion synthesis and up-conversion luminescence of La₂O₂S: Er³⁺, Yb³⁺ nanophosphors. *Journal of Solid State Chemistry*, 226, pp.255-261.
- [13]. Shan, S.N., Wang, X.Y. and Jia, N.Q., 2011. Synthesis of NaYF₄: Yb³⁺, Er³⁺ upconversion nanoparticles in normal microemulsions. *Nanoscale research letters*, 6(1), pp.1-5.
- [14]. Zhang, Y., Hu, S., Tian, T., Xiao, X., Chen, Y., Zhang, Y. and Xu, J., 2022. Growth and Spectral Properties of Er³⁺ and Yb³⁺ Co-Doped Bismuth Silicate Single Crystal. *Crystals*, 12(11), p.1532.
- [15]. Maaoui, A., Haouari, M., Bulou, A., Boulard, B. and Ouada, H.B., 2018. Effect of BaF₂ on the structural and spectroscopic properties of Er³⁺/Yb³⁺ ions codoped fluoro-tellurite glasses. *Journal of Luminescence*, 196, pp.1-10.
- [16]. Martincik, J., Nikl, M., Ishizu, S., Fukuda, K., Cechak, T., Beitlerova, A., Polak, K. and Yoshikawa, A., 2010, November. VUV-UV-visible luminescence of Nd³⁺, Er³⁺ and Tm³⁺ and energy distribution in LiLuF₄ single crystal host. In *IOP Conference Series. Materials Science and Engineering (Online)* (Vol. 15).
- [17]. Ji, L., Zhang, X., Zhang, T., Wang, Y., Wang, F., Zhong, Z., Chen, Z.D., Xiao, Z., Chen, L. and Li, S., 2019. Band alignment of Pb–Sn mixed triple cation perovskites for inverted solar cells with negligible hysteresis. *Journal of Materials Chemistry A*, 7(15), pp.9154-9162.
- [18]. Wang, Q., Tan, M.C., Zhuo, R., Kumar, G.A. and Riman, R.E., 2010. A Solvothermal Route to Size-and Phase-Controlled Highly Luminescent NaYF₄. *Nanoscience and Nanotechnology*, 10, pp.1-8.

- [19]. Pal, S.K., Mehta, N., Atyia, H.E. and Fouad, S.S., 2021. Investigation of optical band-gap and related optical properties in thin-films of Ge containing Se-Te-Sn alloys. *Journal of Non-Crystalline Solids*, 551, p.120399.
- [20]. Aisida, S.O., Ahmad, I., Zhao, T.K., Maaza, M. and Ezema, F.I., 2020. Calcination effect on the photoluminescence, optical, structural, and magnetic properties of polyvinyl alcohol doped ZnFe₂O₄ nanoparticles. *Journal of Macromolecular Science, Part B*, 59(5), pp.295-308.
- [21]. Mbule, P.S., 2013. *The effects of the ZnO nanoparticles buffer layer on organic solar cells* (Doctoral dissertation, University of the Free State).
- [22]. Zunger, A. and Malyi, O.I., 2021. Understanding doping of quantum materials. *Chemical Reviews*, 121(5), pp.3031-3060.
- [23]. Woods-Robinson, R., Han, Y., Zhang, H., Ablekim, T., Khan, I., Persson, K.A. and Zakutayev, A., 2020. Wide band gap chalcogenide semiconductors. *Chemical reviews*, 120(9), pp.4007-4055.
- [24]. Kar, Samares. (2014). Re: What is the effect on band gap by doping semiconductor bulk crystal?. Retrieved from: https://www.researchgate.net/post/What_is_the_effect_on_band_gap_by_doping_semiconductor_bulk_crystal/54382611cf57d770798b45e0/citation/download.
- [25]. Bianchi, M., Hatch, R.C., Mi, J., Iversen, B.B. and Hofmann, P., 2011. Simultaneous quantization of bulk conduction and valence states through adsorption of nonmagnetic impurities on Bi₂Se₃. *Physical Review Letters*, 107(8), p.086802.
- [26]. Kumar, Rajesh. (2016). Re: What is the effect on band gap by doping semiconductor bulk crystal?. Retrieved from: https://www.researchgate.net/post/What_is_the_effect_on_band_gap_by_doping_semiconductor_bulk_crystal/56d0061264e9b2c5b58b4585/citation/download.
- [27]. Gadkari, Dattatray. (2019). Re: What is the effect on band gap by doping semiconductor bulk crystal?. Retrieved from:

https://www.researchgate.net/post/What_is_the_effect_on_band_gap_by_doping_semiconductor_bulk_crystal/5d1d6815f8ea525fd70041fb/citation/download.

[28]. Li, Z., Miao, H., Fu, Y., Liu, Y., Zhang, R. and Tang, B., 2016. Fabrication of NaYF₄: Yb, Er nanoprobe for cell imaging directly by using the method of hydron rivalry aided by ultrasonic. *Nanoscale research letters*, 11(1), pp.1-10.

[29]. [1]. Piters, T.M., Aceves-Mijares, M., Berman-Mendoza, D., Berriel-Valdos, L.R. and Luna-López, J.A., 2011. Dose dependent shift of the TL glow peak in a silicon rich oxide (SRO) film. *Revista Mexicana de Física*, 57(2), pp.26-29.

[30]. Toktamiş, H. and Yazici, A.N., 2012. Effects of annealing on thermoluminescence peak positions and trap depths of synthetic and natural quartz by means of the various heating rate method. *Chinese Physics Letters*, 29(8), p.087802.

[31]. Mbule, P., Mlotswa, D., Mothudi, B. and Dhlamini, M., 2021. Photoluminescence and thermoluminescence analysis of Zn₂SiO₄: Dy³⁺ nanophosphor. *Journal of Luminescence*, 235, p.118060.

CHAPTER 6

Summary and Future works

6.1 CONCLUSION

This research explains the solution combustion route of synthesizing undoped NaYF₄, Yb³⁺-Er³⁺ co-doped NaYF₄, NaGdF₄, and Yb³⁺-Nd³⁺ co-doped NaGdF₄ nanocrystals synthesized at different doping concentrations and annealed at 600 °C and 700 °C. The properties, such as the crystallite phases, structural, morphological, elemental, thermal stability, optical absorption, and luminescence properties, were characterized using techniques such as XRD, SEM-EDS, Raman, FTIR, TGA, UV/Vis/NIR, PL, and TL spectroscopy.

This study is focused on the effects of varying dopant concentrations and annealing temperatures on the phases, structural, morphological, elemental, and optical properties of the nanocrystals. Findings from this research are outlined below:

The UC products NaYF₄ and NaGdF₄ doped with RE³⁺ ions can be successfully prepared via the combustion method using urea as a fuel. The crystal phases of the nanocrystals were observed from XRD studies and confirmed by Raman analysis. The morphological, chemical, and elemental compositions of the nanocrystals were investigated using SEM-EDS. Phonon vibrations in the prepared samples were studied using FTIR spectroscopy. Stability temperatures and weight losses in the doped samples was observed using TGA analysis. A PL study on the prepared samples revealed the presence of energy transfer between the RE dopants and the NaYF₄ and NaGdF₄ hosts and concentration quenching when the dopant concentration exceeded the threshold concentration. The optical properties of the samples were investigated using UV/Vis/NIR spectroscopy; a change in the absorption band edge due to doping and annealing was observed, indicating that the band gap of the prepared NaYF₄ and NaGdF₄ nanocrystals could be tuned; the band gap was estimated using the Kubelka-Munk relation. The UCL of the nanocrystals was enhanced by increasing the annealing temperatures. Defects in the nanocrystals were studied using TL spectroscopy. We can conclude that with careful variation of sensitizer-

activator doping concentration and thermal treatment, these materials stand a good chance as both light intensity amplifiers and photon absorption efficiency enhancers in PSCs because they can absorb more light overall and increase the efficiency of photon harvesting by emitting visible light after absorbing NIR light.

6.2 FUTURE WORK

In this study, NaYF₄ and NaGdF₄ were co-doped with Yb-Er and Yb-Nd, respectively. In the future, more studies can be done to stabilize the NaGdF₄ materials. The next step will be an investigation into the viability of using these nanocrystals in the active layer of PSCs as NIR photon absorbers to enhance the cells' absorption and performance. Therefore, the fabrication of a solar cell device is necessary for evaluating the potential of these nanocrystals as photon absorption boosters.

6.3 PUBLICATION

- Pebetsi Thokwane and Pontsho Mbule, “Analysis of the NaYF₄:Yb³⁺,Er³⁺ nanocrystals: up-conversion luminescence, crystal structure and morphology influenced by the dopant concentration and annealing temperature” – **Accepted in Bulletin of Materials Science Journal.**
- Pebetsi Thokwane, Luyanda Noto and Pontsho Mbule, “Structural and thermoluminescence properties of NaYF₄ prepared by solution combustion synthesis method.” – **Submitted in the Journal of Luminescence.**

